Paul Tirk, BSc MSc

Recent Developments in Sample Preparation and Measurement for Inductively-Coupled Plasma Optical Emission Spectrometry

DISSERTATION

zur Erlangung des akademischen Grades

Doktor der technischen Wissenschaften

eingereicht an der

Technischen Universität Graz

Betreuer

Em. Univ.-Prof. Dr. techn. Dipl.-Ing. Günter Knapp

Institut für Analytische Chemie und Lebensmittelchemie

Graz, April 2016

EIDESSTATTLICHE ERKLÄRUNG

Ich erkläre an Eides statt, dass ich die vorliegende Arbeit selbstständig verfasst, andere als die angegebenen Quellen/Hilfsmittel nicht benutzt, und die den benutzten Quellen wörtlich und inhaltlich entnommenen Stellen als solche kenntlich gemacht habe. Das in TUGRAZonline hochgeladene Textdokument ist mit der vorliegenden Dissertation identisch.

Datum

Unterschrift

Zusammenfassung

Diese Arbeit befasst sich mit verschiedenen Projekten zum Thema „Optische Emissionsspektrometrie mit induktiv gekoppeltem Plasma“ (engl.: inductively-coupled plasma optical emission spectrometry, ICP-OES). Der erste Teil behandelt die Probenvorbereitung. Es wurde einerseits ein neuer Aufbau des mikrowellenunterstützten Hochdruckdurchflussaufschlusssystems charakterisiert als auch Diesel mit Hilfe von mikrowelleninduzierter Verbrennung zur anschließenden Bestimmung von Schwefel aufgeschlossen. Im zweiten Teil wird ein neues optisches Interface für die ICP-OES beschrieben, welches das Plasma von der Umgebung abschließt. Dadurch kann ein Teil der Plasmagase rezykliert werden, was einer hohen Ersparnis der Betriebsmittel gleichkommt. Zusätzlich werden neue Erkenntnisse zum sogenannten „Carbon Enhancement Effect“ präsentiert.

Abstract

In this work different projects in the field of inductively-coupled plasma optical emission spectrometry (ICP-OES) are presented. The first part deals with sample preparation. A new approach for microwave-assisted high pressure flow digestion was investigated and, in addition, diesel samples were digested using microwave-induced combustion for the subsequent determination of sulfur. In the second part a newly constructed optical interface for ICP-OES was designed which seals the plasma from the surroundings. This makes it possible to recycle part of the plasma gases leading to high savings of running costs. Furthermore, novel insights into the so-called “carbon enhancement effect” are given.

Danksagung

Am Ende eines Dissertationsunterfangens (bzw. am Anfang der Dissertation) ist Platz um Dankbarkeit zu zeigen. Dankbarkeit für die Erfahrungen und die Menschen, die einen im Laufe der Zeit begleitet und bereichert haben.

An erster Stelle gilt mein Dank meinem Betreuer Helmar Wiltsche, welcher mir das Angebot der Doktoratsstelle am Institut für Analytische Chemie und Lebensmittelchemie unterbreitete und mir schon seit Beginn meiner Masterarbeit immer mit Rat und Tat zur Seite stand. Unter seiner fachlichen Kompetenz habe ich viel im Bereich der angewandten Atomspektrometrie erfahren und gelernt. Meinem Doktorvater Günter Knapp sei an gleicher Stelle für den regen Austausch im gemütlichen Beisammensein und seine Großzügigkeit gedankt.

Dankbar bin ich auch über das großartige Arbeitsklima am Institut, trotz verschiedener Arbeitsgruppen und Fachgebiete herrscht ein Zusammenhalt untereinander und großes gegenseitiges Interesse. Im Besonderen hervorzuheben ist in diesem Zusammenhang mein Büro-/Laborkollege und Freund Herbert Motter, der immer und stets – auch außerhalb der Institutsräumlichkeiten – zwei helfende Hände parat hat und – das muss ehrlicherweise auch gesagt werden – meine zeitweise schwindende Motivation an der Forschung immer wieder aufleben hat lassen. Ich werde die gemeinsame Zeit definitiv vermissen.

Gerade die letzte Zeit in meinem Leben zeichnete sich durch große Erkenntnisse und Veränderungen aus, die ich zum größten Teil meinen Freunden verdanke, welche mir auch in jeder Lebenslage und kleineren Krise immer mit Liebe und Verständnis entgegen kommen. Dasselbe gilt für meine Eltern, sie haben mich bestmöglich auf das Leben vorbereitet und stehen mir immer mit Unterstützung und Rat zur Seite.

Graz, im April 2016 Paul Tirk

Dissertation

Recent Developments in Sample Preparation and Measurement for Inductively-Coupled Plasma Optical Emission Spectrometry

Paul Tirk, BSc MSc

Institut für Analytische Chemie und Lebensmittelchemie
Technische Universität Graz

Betreuer: Em. Univ.-Prof. Dr. techn. Dipl.-Ing. Günter Knapp

Graz, im April 2016

Contents

Preface

Over the last years I worked on different projects related to the field of analytical chemistry and especially inductively-coupled plasma optical emission spectrometry (ICP-OES). Achievements were made in both the sample preparation as the essential first step of every analysis as well as the instrumentation and measurement. The thesis is therefore divided into two parts. The first deals with topics in sample preparation while the second one describes advances in ICP-OES. At the beginning of every part, underlying theory and concepts are presented in different chapters. They are followed by the relevant publications.

The first project in sample preparation was part of developing a microwave-assisted high pressure flow digestion system suitable for preparation and digestion of slurries [1] (see chapter 3). In addition, I spent two months at the "Universidade Federal de Santa Maria" (UFSM) in Santa Maria (Rio Grande do Sul, Brazil) working on a project involving the digestion of diesel samples using the microwave-induced combustion (MIC) method in order to enable the determination of the sulfur content [2] (see chapter 4).

Developments in ICP-OES include the design and construction of a sealed plasma which enables the recycling of parts of the argon stream, a feature which saves almost 90 % of argon consumption (see chapter 8). Additionally, new insights into the long discussed "carbon enhancement effect" are given in chapter 9 [3].

CHAPTER 1

Analytical Process

Because the two main divisions of this thesis are part of the solution to an analytical question this first chapter tries to briefly summarize the so-called "Analytical Process". It describes the path from the analytical problem to the solution or result and can be roughly divided into the following steps:

Definition of the problem At the beginning of every analysis we have to ask ourself the question of what exactly do we want to know or achieve. The definition of the analytical problem has to include at least the analyte(s) or species of interest and information about the sample's nature and/or the sample matrix. It then leads us to a selection of the available analytical techniques and the necessary sampling and sample pre-treatment steps.

Choice of the method After the desired information has been defined, a suitable analytical technique has to be chosen. Sometimes only one method is available but often it is necessary to select from a variety of possibilities. When selecting the optimal method we should consider factors like efficiency, time, errors, selectivity and safety. Ideally, the technique of choice is a validated one, which has been tested in various laboratories for its applicability and therefore gives an accurate measurement for the type of analyte and sample. The chosen method also has a big influence on the following sampling and sample preparation steps.

Sampling The next and probably one of the most important steps is "sampling". It crucially determines the quality and outcome of the whole analysis and also poses the most difficulties to overcome. "Sampling" refers to the selection of a small representative portion from the untreated material of interest. Care must be taken to ensure the sample's representative character, *i.e.* its qualities and origins have to correspond well with the desired objectives set in the "definition of the problem". Attention should be payed also to sample storage and transport as to not impair the actual analysis by deteriorating the analytes. This information should be well defined in a sampling plan, containing procedures for selection, collection, transport and preparation of the samples.

Sample preparation After sampling, sample transport and possible storage, the samples have to be transformed into a form suitable for the following analyses. These procedures involve for example homogenizing (grinding, sieving, *etc.*) and belong to "sample preparation". Different analytical techniques require distinct preparation. Most of the time the samples are required to be in liquid form. Solid matter therefore has to be dissolved, gaseous substances absorbed. Chapter 2 will provide some more insights into this matter.

Measurement Having prepared the samples, the measurement can be conducted where a detector converts a physical quantity into a number. Depending on the analytical technique, the obtained values can be emission or absorption intensities (atomic/molecular emission/absorption, fluorescence, phosphorescence), concentrations, time or even dimensionless numbers.

Calibration Calibration data is used to bring the measured values in relation to the desired quantity. Ideally a mathematical model exists, *e.g.* a linear or quadratic, sometimes polynomial dependency. We can distinguish between three main calibration approaches. External calibration is the most commonly used one. A series of reference solutions with known amounts of the analyte(s) is submitted to the measurement and the calibration function is obtained through the relationship of the analyte concentrations and the measured signal. The reference solutions should at least contain the analyte in the same solvent as the sample. If also the concomitant substances are present we speak of "matrix-matched" solutions. The quality of a calibration depends on three main factors: the repeatability of the measurement, the trueness of the standards and the validity of the comparison. These considerations result in statistical confidence bands of the calibration function. As a consequence, the final results of the analysis should also reflect the calibration uncertainties

as confidence limits. When dealing with complex sample matrices (for example petroleum), standard addition is sometimes preferred. The sample – and therefore its matrix – forms the base for the calibration standards. Again, known amounts of the analyte(s) are added directly to the sample solution. The third concept to mention is internal standardization. A substance which should behave chemically similar to the analyte(s) is added to all calibration standards and samples. It therefore runs through all sample preparation steps. The measured values are then divided by the signal of the internal standard resulting in a set of ratios, thus eliminating potential losses and signal alterations due to variations in the analytical instrument. It is obvious that especially in multi-element analysis the choice of a suitable internal standard is difficult or even impossible. In inductively-coupled plasma mass spectrometry (ICP-MS) multiple internal standards are usually added for different ranges of element masses.

Data processing/evaluation By applying the calibration function to the measured data we obtain the desired concentrations. These have to be interpreted and evaluated by taking into account quality control measures such as the use of certified reference materials (CRMs) or the determination of blank values which give rise to limits of detection (LODs) and limits of quantification (LOQs). In the end a number of statistical treatments is usually involved in the summarization and preparation of the final values. Uncertainties are supplied for every result. Chemometric techniques are available to help finding correlations and deal with large amounts of data which readily occur in multi-element determinations. All these considerations are necessary to assess if the results are valid for the given analytical question or if measurements have to be repeated or altered.

Summing up, it should be pointed out that the most critical and time-consuming step of the analytical sequence is the sample preparation. Great care must be taken because there lie most of the potential error sources of the analysis. Many aspects and techniques are presented in the sample preparation chapter (chapter 2).

Part I.

Sample Preparation

CHAPTER 2

Sample Preparation

The transformation of samples into the form suitable for the subsequent measurement is part of the sample preparation step. After the sampling and appropriate storage it is a crucial step in every analysis. Many of the analytical techniques require the samples to be in a liquid form. An advantage of solutions is that the calibration can be easily done using reference solutions and dilutions can be made without great effort. Additionally, the carbon contained in organic samples can significantly impair the measurements in ICP-OES and ICP-MS and should be removed as much as possible (see also chapter 9). These circumstances make sample decomposition through wet digestion an advantageous step. On the other hand, the downside of every sample preparation step is the risk of contamination and – in case of wet digestion – further dilution of the analyte(s).

This chapter tries to summarize briefly the procedures and processes of "sample preparation" in order to better understand the articles about "flow digestion" and microwave-induced combustion (MIC) which are presented in succession as chapters 3 and 4. It is loosely based on chapters 1, 5 and 9 of the book "Microwave-assisted sample preparation for trace element determination" [4].

2.1. Pre-Treatment/Homogenization

Depending on the nature and state of the samples additional pre-treatment may be necessary. Most of the time the samples are of rather inhomogeneous composition. In order to obtain

a representative sample different homogenization techniques have to be applied. These mainly include mechanical procedures for homogenization and preparation for a following digestion step. The next paragraphs give an overview of the most common pre-treatment steps.

Cleaning can be necessary, for example, when dealing with parts of plants to remove soil or dust. Care must be taken to not bring in more contaminants through the use of the washing agents. To avoid the risk of leaching the cleaning process should be as short as possible.

Drying is the controlled removal of water from the samples until a constant weight is achieved. It is a common requirement for solid samples because of their unknown amount of contained water. The temperature has to be chosen such as to not volatilize the analytes but still high enough to evaporate water. It ranges from 60 – 65 °C for biological samples up to more than 1000 °C for some minerals. Both ovens and desiccants are used. A special case of drying is "lyophilization" where the sample is first frozen between −80 and −60 °C and then dried in a vacuum at temperatures of −20 and 40 °C.

Grinding increases the homogeneity of the samples by reducing the particle sizes. Afterwards the representativity of the samples is achieved because the ground particles can be mixed more easily. In addition, grinding increases the surface to volume ratio of the particles which leads to a higher solubility and reactivity towards reagents in the following digestion procedures. The comminution through grinding can be considered one of the most critical steps in the analytical sequence as the parts of the mill pose a high risk of contamination depending on their chemical composition. Therefore the hardness or abrasive resistance of the grinding components must be higher than the one of the sample. The collisions between the sample particles and the grinding components generally cause a warming which has to be considered when dealing with volatile analytes.

For matter that is soft, smooth and elastic at room temperature (*e.g.* most biological samples) cryogenic grinding was developed. It relies on increasing the hardness of the tissues by freezing. As a result very little force is necessary to break the structures.

Sieving separates the particles into classes of different size distributions. It allows the classification and evaluation of the particle sizes which can provide insights into the

effectiveness of the chosen grinding method as well as the achieved homogeneity of the sample. If metal sieves are used there is a risk of contamination similar to grinding. Especially in trace analysis this has to be kept in mind.

Filtering When dealing with solutions which already contain particulate matter, a filtering step may be necessary. It depends on the selected analytical technique as these particles can cause problems by coagulation and clogging in essential parts of the instruments. Especially ICP-based devices use pneumatic nebulizers which are prone to irreversible obstruction. Therefore, filtration through membrane filters is recommended. On the other hand, if we are interested in the particles, filtration provides a way to separate them from the liquid parts of the sample. The residue on the filter can then be decomposed and analyzed separately.

2.2. Conventional Sample Preparation

Before going into the microwave-assisted sample preparation techniques and their recent developments presented in this thesis, a brief overview of conventional open and closed systems is given.

2.2.1. Dry Ashing

The probably simplest method to decompose biological and organic samples is dry ashing. Oxidation occurs by pyrolysis and combustion using the oxygen in the air and releasing the carbon in form of CO_2. Depending on the composition of the sample additional products include water and nitrogen compounds. The remaining ashes contain the inorganic elements mostly in form of metal oxides but also as non-volatile sulfates, phosphates and silicates.

After the sample has been put into a crucible it is placed into a muffle furnace or upon a simple laboratory flame. The temperature range for the pyrolysis of organic matter is usually between $450-600\,^{\circ}\mathrm{C}$. In order to avoid potential losses due to volatilization of the analytes the heating program has to be chosen carefully. Compounds containing chlorine can also lead to the formation of metal chlorides (*e.g.* $PbCl_2$, $CdCl_2$) which are lost easily. Another problem arises when there is a reaction between the analytes and the crucible. Other materials like quartz or platinum are available to counteract these processes.

Despite the mentioned potential risks, dry ashing remains a very effective and simple technique in preparation of solid samples for trace element determination and is still widely used as a standard procedure for petroleum products and foods. The dry ashing process requires little attention of the analyst, sample masses greater than 10 g are possible and the materials and instruments are rather inexpensive. Variations of this technique employ infrared (IR) or microwave radiation. A more recent development uses microwaves to ignite the pyrolysis of the sample under an oxygen atmosphere (see MIC, section 2.5 and chapter 4).

2.2.2. Wet Decomposition

In contrast to simple dry ashing concentrated mineral acids or acid mixtures can be added to the sample as the oxidizing reagents. These procedures are summarized under the term "wet digestion" or "wet decomposition". It only requires slightly elevated temperatures and results in acidic solutions. The analytes are available in simple inorganic forms and the solutions are readily usable in most atomic spectrometry instruments. For organic and biological samples, nitric, sulfuric and perchloric acids produce clear solutions which indicate a complete decomposition although the residual carbon content (RCC) should be checked as it can cause interference in the subsequent measurement. Analytes can also remain retained in undecomposed organic substances. Compared to dry ashing the main advantage of wet digestion is the low reaction temperature. It reduces the risk of volatilization of the analytes although requires more attention of the analyst as concentrated acids or acid mixtures are involved.

Wet digestion systems can be divided into two classes: open and closed systems. In open systems volatile elements such as halogens, antimony, arsenic, boron, selenium and mercury are obviously prone to be lost through evaporation. Furthermore, the boiling temperature of HNO_3 (azeotrope with water, 121 °C) is often not sufficient to achieve a complete decomposition as higher temperatures are needed to destroy the C–C bonds of organic molecules. The highest oxidation power is provided by $HClO_4$ but due to the formation of unstable perchlorates and their explosive nature it cannot be used as the only reagent in concentrated form. In case of silica matrices hydrofluoric acid helps to decompose the insoluble residue which also may contain analyte elements.

As stated before, losses due to volatilization are a big concern in open wet digestion systems. In addition, the highest possible decomposition temperature is limited by the boiling temperature of the solvent or acid at ambient pressure. According to Arrhenius,

the temperature also determines the reaction rate, which directly relates to the required time to achieve a sufficient decomposition. It is obvious that by closing the digestion system, an increased pressure allows higher reaction temperatures, thus remedying the aforementioned limitations. Furthermore, the digestion solution cannot evaporate thus leading to less reagent consumption while the closed nature of the setup minimizes the risk of contamination. On the other hand, it is clear that a closed system inherently bears the risk of explosion and therefore safety measures have to be taken. The vessels can be made of quartz or fluorinated polymers, the latter ones limit the operating temperatures to less than 260 °C. At high pressures and temperatures some elements can also diffuse into polytetrafluorethylene (PTFE). This circumstance is known as "memory effect" because in addition to the analyte losses the elements located in the vessel walls can be released later, potentially leading to cross-contamination. Modern modifications and copolymers have a lower porosity and help to minimize this problem. For most digestions pure HNO_3 is usually sufficient and safe to use. As the oxidation potential increases with temperature, low RCCs are achieved. If hydrofluoric acid has to be added, vessels made of quartz cannot be used and PTFE becomes the material of choice. Due to the aforementioned explosion risk of closed systems, perchloric acid is to be avoided strictly, as it can produce pressure gradients which are too high for the safety devices to respond.

2.3. Flow Digestion

In sample preparation three types of systematic errors are found. Contamination by dust, reagents, vessel material and impurities on the vessel's surface can be prevented by using closed systems. Flow digestion systems allow most of the sample handling procedures to be done in a closed environment while the continuous rinsing of the tubing with the carrier solution effectively avoids both cross-contamination between subsequent samples as well as adsorption of analytes at the tube walls. Secondly, a closed system avoids potential losses of elements due to volatilization while the use of inert materials (*e.g.* PTFE, PFA) minimizes reactions with the tubing. The third source of errors are interferences with remaining carbon resulting from incomplete decomposition of organic samples. The RCC after digestion in flow systems is generally higher because of the shorter residence time of the samples in the heated digestion zone. More detail on the deleterious effects of carbon in ICP-based analytical techniques is given in chapter 9.

Because of the continuous nature of flow systems only liquid samples or slurries (suspension of ground solid samples in water or acid) can be digested. In contrast to batch processes,

automating the sample handling steps is easier to achieve. Furthermore, direct coupling with the following measurement devices is possible. The main stages of a flow digestion system are sample introduction, heating and as the last step, cooling and degassing. In sample introduction the reagent is added to the sample and mixed, if necessary. A defined volume is then pushed by the carrier solution into the heated digestion zone. Here the pressure defines the temperature of the boiling equilibrium. For a good decomposition temperatures of around 200 °C are desired, depending on the reagents the pressure should be around 20 bar (10 % nitric acid in water). After passing through the heated zone the sample solution reaches the cooling and subsequently the degassing stage where the gaseous reaction products are separated from the liquid sample digests. This is done to avoid gas bubbles which on the one hand contain large portions of CO_2 (refer to chapter 9 and on the other hand can cause fragmentation of the sample liquid resulting in fluctuation of the analyte signal during measurement. At the end of the digestion system the pressure has to be lowered to ambient conditions in order to receive the digested sample solution for further processing.

Although in principle flow digestion systems appear rather simple there are a few disadvantages to bear in mind. In general, oxidation efficiencies are low due to the rather short digestion times. Both the oxidation efficiency and the digestion time can be improved by increasing the pressure in the system. Cross-contamination can occur between subsequent samples and is dependent on rinse times, flow velocities and properties of the tubing, such as diameter and material. Especially the inner diameter of the tube is of importance as it determines the maximum allowed particle size in the samples. Particles should not exceed half the inner diameter of the tubing. For larger tube diameters clogging tends to happen more because of swelling or agglomeration of the particles. It has to be kept in mind that a low flow velocity also contributes to segregation of larger particles.

Flow digestion systems can be classified by three characteristics: (1) the operating pressure and temperature, (2) the type of heating (conductive, multimode microwave and focused/-monomode microwave) and (3) the flow program (continuous flow or stopped flow). The most practically and for the design of the system most relevant aspect is the operating pressure. Three pressure ranges are described in literature. In ambient pressure systems a strong formation of bubbles is observed due to the low solubility of gases. The atmospheric pressure limits the boiling point of the digestion solution to around 120 °C, a temperature which provides a rather low oxidation efficiency. These systems are therefore more suitable for the dissolution of insoluble precipitates. The tubing can be made of PTFE or perfluoroalkoxy alkane (PFA) and there are no additional valves needed, allowing the use of highly corrosive acid mixtures without an increased risk of contamination from the valve materials.

The upper pressure limit of medium pressure systems is chosen arbitrarily at 25 bar with the corresponding boiling temperature of 180 °C. Bubble formation is less pronounced while the RCC remains rather high which can cause interference in the subsequent measurement.

In case of nitric acid as the only reagent a temperature of at least 200 °C is necessary if a RCC below 10 % is desired. Complete decomposition of organic substances with nitric acid occurs at temperatures of around 300 °C due to the relatively strong C–C bonds [5, 6]. Under these circumstances (> 200 bar pressure) only a liquid phase is present as the gas is totally absorbed. High pressure flow digestion systems operate at pressures greater than 25 bar. The introduction of the sample requires HPLC-grade 6-port valves and a sample loop while the depressurization is achieved by a restrictor capillary after cooling and degassing of the sample solution. It should be noted, that the temperature limit of PTFE/PFA material is 250 °C which in turn limits the possible pressure. In literature, a system employing a Pt/Ir capillary can be found [7]. It enables a pressure of 300 bar with decomposition temperatures around 360 °C.

The energy in flow digestion systems can be introduced both through conventional and microwave heating. Microwaves are mostly absorbed by the liquid phase and not by steam resulting in an efficient energy transfer and a kind of boiling equilibrium inside the tube. In comparison, with conventional heating there is always a temperature gradient from the heating element to the flowing medium, meaning that the tube is always hotter than the actual digestion solution. On the other hand a major downside of (multimode) microwave systems is the heterogeneous field which induces local hotspots. This eventually causes material failure at certain points of the digestion tube. It should be noted that for medium and high pressure flow digestion systems, the PTFE and PFA tubes have to be surrounded by an additional supporting structure in order to withstand the pressure. Available options include high-tensile strength fibers or stainless steel tubes.

The project I was working on during the last years is described in further detail in chapter 3. More recent developments of the presented flow system including a different reactor geometry with higher volume were done by Thiago Linhares Marques and are already published in [8].

2.4. Combustion

Sample combustion is an attractive alternative to wet digestion. Organic matter is oxidized almost completely leaving only the inorganic remains. As the main reagent is oxygen there is a lower risk of contamination which makes combustion especially interesting for trace element analysis. After the decomposition the nonvolatile analytes (Fe, Si, Al, alkaline elements, *etc.*) are found in the ashes and can be further treated. The volatile elements such as halogens are released into the gas phase and can be absorbed in a suitable solution. Typically, all absorbing solutions are diluted which is an important aspect considering green chemistry recommendations. Furthermore, residues and contamination by the reagents can be minimized. This circumstance also improves blank values and as a result, LODs, while interferences in the following measurement due to high concentrations of reagents are also lowered.

For a sample only containing carbon, hydrogen and oxygen the general formula of the combustion reaction is given by equation 2.1. In a complete combustion the compounds react with the oxygen and decompose into H_2O and CO_2 leading to clean digests. This reaction applies to many organic sample matrices like carbohydrates, lipids and proteins, as well as to hydrocarbons of crude oil or monomers of a polymer. The oxygen as the oxidant can be supplied as pure gas or from the surrounding air.

$$C_xH_yO_z + (x + {}^1\!/_4\, y - {}^1\!/_2\, z)\, O_2 \longrightarrow x\, CO_2 + {}^1\!/_2\, y\, H_2O \tag{2.1}$$

In combustion we can also distinguish between open and closed systems. Open combustion systems were already discussed in section 2.2.1 as dry ashing. Regarding closed systems a series of developments were made: Schöniger flask and the combustion bomb. In the Schöniger method a simple glass flask is used to burn the sample. Contamination by metal is avoided but the sample mass is limited to around 200 mg. In contrast the combustion bomb is a stainless steel container which is able to withstand higher pressures and therefore higher sample masses are possible, but at the cost of increased contamination due to the bomb material. The later introduced microwave-induced combustion (MIC) combines the concepts of closed vessel wet digestion and combustion into one single technique. It is described further in the following section.

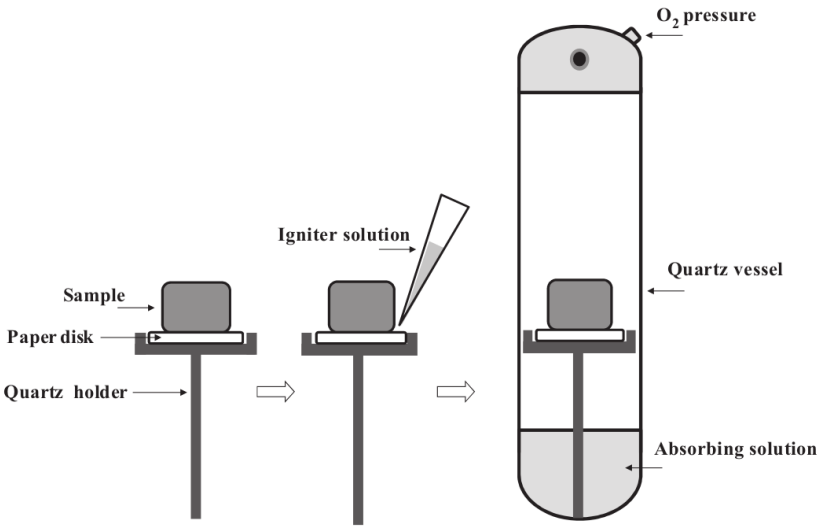

Figure 2.1.: General procedure for MIC in closed vessels [4, p. 154].

2.5. Microwave-Induced Combustion (MIC)

The microwave-induced combustion (MIC) technique was developed in 2004 by Érico Marlon de Moraes Flores at the Universidade Federal de Santa Maria in cooperation with Günter Knapp (Graz University of Technology) [9]. It combines the advantages of classical combustion bomb techniques and microwave-assisted closed vessel digestion into a single system. In MIC, the combustion is initiated by microwaves instead of electric currents. It is carried out in the same quartz vessels used for wet digestion which reduces contamination with metals, only a quartz sample holder is added. The samples are placed in form of pellets onto the sample holder. Liquid samples have to be wrapped in a suitable material such as polycarbonate (PC) capsules or polyethylene (PE) film.

Figure 2.1 depicts the general MIC procedure. After the sample has been placed onto the quartz holder, which has already been prepared with the filter paper, the igniter solution (usually NH_4NO_3) is added. The sample holder is then inserted carefully into the quartz vessel which contains the absorbing solution. After closing of the vessel it is pressurized with oxygen and placed into the microwave system. Ignition occurs within 10 seconds after starting the microwave irradiation. Following the combustion a reflux step can be added in order to improve the absorption of the analytes.

Chapter 4 provides more detail of the project which was done at the "Universidade Federal de Santa Maria" (UFSM) in Brazil.

CHAPTER 3

Flow Digestion

Helmar Wiltsche, Paul Tirk, Herbert Motter, Monika Winkler and Günter Knapp

The following chapter was published in the "Journal of Analytical Atomic Spectrometry", Volume 29 (2014), pages 272 – 279 under the title "A novel approach to high pressure flow digestion" [1].

Abstract

A new high pressure flow digestion system has been developed for sample digestion at a pressure of up to 40 bar and a temperature of about 230 °C. The reaction with acids takes place in a PFA tube and is heated by microwave radiation in a multimode cavity. As the PFA tube cannot withstand the harsh digestion conditions without support, it is placed inside a coiled glass tube pressurized by 40 bar nitrogen thus forming an autoclave. Corrosion of system components by acid fumes and related sample contamination is circumvented by establishing a slow but steady flow of the high pressure nitrogen countercurrent to the sample flow. The presented system does not constrain the selection of the digestion reagent. Acid cocktails of nitric acid with hydrochloric and/or hydrofluoric acid as well as hydrogen peroxide were successfully used for the digestion of various samples. The method accuracy was validated with five certified reference materials (BCR 62, DORM-2, NIST SRM 1515, NIST SRM 1567, NIST SRM 1568) and good agreement between the determined and the certified values was obtained for Al, Ca, Cr, Cu, Fe, Mg, Mn, Ni, Pb, and Zn using inductively-coupled plasma optical emission spectrometry (ICP-OES) for analyte quantification. The flow digestion of the CRMs resulted in clear solutions with residual carbon concentrations (RCCs) between 11 and 40 %. Spike recoveries of Al, As, Ba, Be, Bi, Cd, Co, Cr, Cu, Fe, Mg, Mn, Mo, Ni, Pb, Sb, Se, Sr, Ti, V, and Zn were between 94 and 105 %. For Hg the spike recovery was 89 %. The fully automated high pressure flow digestion system is capable of digesting up to 6 samples per hour.

3.1. Introduction

Flow digestion is an attractive alternative to closed vessel microwave assisted digestion due to the ease of automation, the reduced risk of contamination and the capability of direct coupling to analyte quantification techniques. In general the sample is first mixed with the digestion acid (usually HNO_3 or acid cocktails). Then the sample/acid mixture is heated by passing through a heating zone. In continuous flow systems the sample is pumped through the heating zone continuously by a carrier solution [10–12] while in stopped flow systems the sample is pushed into the heating zone by the carrier solution, then the carrier flow is stopped and the sample is heated [13–15]. At the end of the digestion period, the sample is pushed out of the digestion zone by turning on the carrier solution again. In most flow digestion systems reported in the literature microwave heating was used but in some cases conductive heating was employed. After the heating zone, gases that evolved during the digestion (*e.g.* nitrous oxides, CO_2) can be removed by a gas/liquid separator.

Flow digestion systems can be classified as already noted by their mode of operation (continuous flow or stopped flow), by their means of heating the sample/acid mixture in the digestion zone (conductive heating, microwave heating) or by the pressure inside the digestion system. The pressure inside the heated digestion coil is of great importance as it determines the maximum temperature of the acid mixture and thereby the efficiency of the digestion [16]. Three pressure regimes may be distinguished: ambient, medium (< 25 bar) and high pressure (> 25 bar) flow digestion systems. It is well known that the digestion efficiency of any acid digestion system increases with the temperature of the digestion acid. As the boiling point of the acid limits the maximum attainable digestion temperature it is highly desirable to increase the pressure inside the digestion system.

Ambient pressure systems dominate the literature as they are relatively easy to build. Burguera [17–19] pioneered these systems using microwave assisted sample heating. Ambient pressure flow digestion systems are capable of operating with highly corrosive acids like HCl or mixtures of HCl and HNO_3 as the entire flow path is usually made of either inert polymers or glass [19, 20]. The main disadvantage of ambient pressure flow digestion systems is that gaseous reaction products eject the sample/acid mixture quickly from the heated dissolution zone reducing the effective digestion time and causing undesired peak broadening. The maximum digestion acid concentration [21, 22] and the maximum power level [23–25] in the heated digestion zone are therefore limited by the gas evolution. Moreover, the digestion acid boils at about 120 °C, causing low efficient oxidation of organic substances.

In a medium pressure digestion system the digestion acid is pressurized up to about 25 bar. Thereby the acid's boiling point is considerably increased (*e.g.* 10 % HNO_3: 230 °C) and the solubility of gaseous reaction products in the digestion mixture is enhanced significantly, reducing dispersion effects [11]. The pressure limit of 25 bar is somewhat arbitrarily chosen as the pressure limit of fiber reinforced PTFE tubes [26]. In medium pressure flow digestion systems the oxidation efficiency of HNO_3 is significantly higher than in ambient pressure systems.

High pressure flow digestion systems operate at pressures above 25 bar. This pressure region is comparable with contemporary closed vessel microwave assisted batch digestion systems. The main difference between batch digestion systems and flow systems in this pressure region is the shorter digestion time in flow systems. Typical digestion times in flow systems are between 2 and 5 min. Haiber and Berndt [27] developed a high pressure system operating at up to 360 °C and 300 bar pressure. In this pressure range all reaction products which are gaseous at ambient pressure remain in a liquid phase [28]. The high digestion temperature resulted in extremely low residual carbon concentrations (<< 1 % RCC). A Pt/Ir ($^{80}/_{20}$) tube was used as the heated pressurized digestion tube [7] as this material showed excellent resistance to nitric and hydrofluoric acid [27, 29]. Nevertheless, mixtures of nitric and hydrochloric acid drastically reduced the digestion tube lifetime [29]. The digestion tube was directly heated by clamping a supply voltage to the two ends of the digestion coil making use of its inherent resistance [27]. It is interesting to note, that Bian *et al.* [30] encountered losses of Ag, Ga and Sb during high pressure digestion in the Pt/Ir tube that increased with rising digestion temperature.

Another high pressure flow digestion system using microwave heating is the pressure equilibrium system described by Knapp *et al.* [16, 31]. The underlying principle is that microwave energy is dominantly absorbed by the liquid phase, whereas steam and gaseous reaction products are not significantly heated. Thereby, a boiling equilibrium is formed much in the same way as in reflux boiling. In the pressure equilibrium system the PTFE dissolution coil is placed in a pressurized vessel, which in turn is located in a microwave field resulting in nearly equal pressure inside and outside of the PTFE tubing. This reduces the mechanical stress on the tubing significantly. Nevertheless, the pressure equilibrium system had several shortcomings: the length of the digestion tube – and as a consequence the actively heated volume – is restricted by the size of the waveguide of the used focused microwave oven. Moreover, cross-contamination between successive samples was observed and delicate optimization of the restrictor length, system pressure and carrier flow was necessary.

The aim of this work was to develop a radical new design of a pressure equilibrium system, overcoming the previous shortcomings. A high degree of automation was considered necessary to ensure reproducible experimental conditions.

3.2. Experimental

3.2.1. Flow digestion system

A high pressure, continuous flow, pressure equilibrium [16] flow digestion system was constructed for this work. Briefly, diluted nitric acid (1 % $^{v}/_{v}$) was continuously pumped through the system by an acid resistant all Ti HPLC pump (Knauer, Germany – figure 3.1, A). If not stated otherwise a carrier flow of 2.0 mL min^{-1} was used. A 10 mL sample loop (figure 3.1, C) connected to a 6-port valve (Knauer, Germany – figure 3.1, B; fluorinated polymer sealed, wide bore channel) was used to inject the samples (figure 3.1, L) into the high pressure stream of the flow system. Automated digestion operation was attained by using an autosampler for sample handling (ASX-1400, Cetac, USA – not shown in figure 3.1 for clarity). Two autosampler needles were used: one for sample uptake and one for collecting the digests. Slurries were stirred for 10 seconds by a polyether ether ketone (PEEK) paddle prior to sampling into the flow digestion system in order to overcome problems associated with settling of solids. The PEEK paddle and the needles were rinsed with water in a separate washing position of the autosampler before sample uptake. The sample volume introduced into the sample loop was controlled by a high precision dispenser (1-Channel MultiDispenser, ProLiquid, Germany – figure 3.1, D) connected to the 6-port valve. Many systems reported in literature used a simpler arrangement, in which the sample loop was completely filled with sample by *e.g.* a peristaltic pump. Using a high precision dispenser for sample uptake allowed us to modify the volume introduced into the digestion system from 0.5 to 10 mL (maximum volume of the sample loop). Drawing the sample through the sample loop avoided potential contamination of the dispenser as the sample never entered the dispenser. Moreover, this mode of dispenser operation allowed embedding the sample between two 2 mL segments of 30 % nitric acid ($^{v}/_{v}$) [27]. After injecting the sample into the high pressure stream the autosampler needle was moved to the rinsing position and 10 mL rinsing solution (figure 3.1, M) were pumped by the dispenser through the needle for cleaning purposes. The sample digestion was performed in a perfluoroalkoxy alkane (PFA) tube (1.5 mm inner diameter, 2.5 mm outer diameter, 4.5 m length) placed inside a coiled borosilicate glass tube (4 mm inner diameter, 8 mm outer diameter, 270 mm

coil diameter – figure 3.1, G). By pressurizing the glass tube with nitrogen (40 bar), the pressure inside and outside of the PFA tubing was almost equal during digestion, significantly reducing the mechanical stress on the tubing during the digestion process. The glass coil therefore formed a pressurized autoclave for the PFA digestion tube. Nitrogen was introduced into the system through the gas/liquid separator (figure 3.1, H) and left the glass coil through an exit port (figure 3.1, E). A restrictor capillary (2 m 0.15 mm inner diameter PEEK tube – figure 3.1, F) connected to this exit port maintained the pressure inside the glass coil and limited the flow of N_2 to about $1\,L\,min^{-1}$. This countercurrent flow of N_2 removed traces of water and acid from the glass digestion coil that otherwise would have accumulated there causing corrosion of the stainless steel tubes and sample contamination. It is important to note, that these traces of liquid resulted not from leakage but from diffusion of steam through the PFA tube [32]. Similar behavior was also observed in other pressure equilibrium systems [16]. The digestion coil was installed vertically [27] inside a commercial microwave oven (Multiwave 3000, Anton Paar, Austria) designed for pressurized batch digestion. This microwave oven does not employ pulse width modulation (PWM) for regulating the power level but is of a constant power type. Thereby overheating and violent reactions associated with PWM modulated microwave ovens could be avoided. Moreover, the oven can be operated under conditions of high reflected microwave power as the magnetron cooling is sufficiently strong, eliminating the need for an absorbing water ballast and enabling fully automated system operation over prolonged time. After leaving the microwave irradiated zone the digested samples were cooled (figure 3.1, K) and gaseous reaction products were removed in a gas/liquid separator (figure 3.1, H). This gas/liquid separator was constructed from a 20 mm outer diameter quartz tube installed in a PEEK casing. After depressurization in a restrictor capillary (12 m 0.5 mm inner diameter PTFE tube – figure 3.1, I) the digests were collected in 50 mL sample tubes (figure 3.1, J) using the autosampler's second sampling needle. All system parameters and procedures including the autosampler were computer controlled thus allowing unattended system operation.

To suppress microwave leakage from the oven, the glass coil (figure 3.2, C) was connected to a grounded stainless steel tube (figure 3.2, D). This glass/steel connection was of crucial importance to the entire system. Both, the glass tube and the steel tube had to stay in place at a pressure of 40 bar to avoid leakage. Nonetheless, the connection had to be flexible enough to compensate for thermal expansion of both tubes. A design similar to a packing gland was used to meet both requirements: the glass tube (figure 3.2, C) was fixated by a PEEK ferrule (figure 3.2, F) using a tightening screw (figure 3.2, E). A 1 mm gap between the glass and the steel tube allowed thermal expansion of both tubes. Over both tubes a 20 mm long silicone rubber tube (figure 3.2, G) of 8 mm inner diameter was slipped evenly. A lantern ring (2 mm long, 8 mm inner diameter; not shown in figure 3.2) was then installed

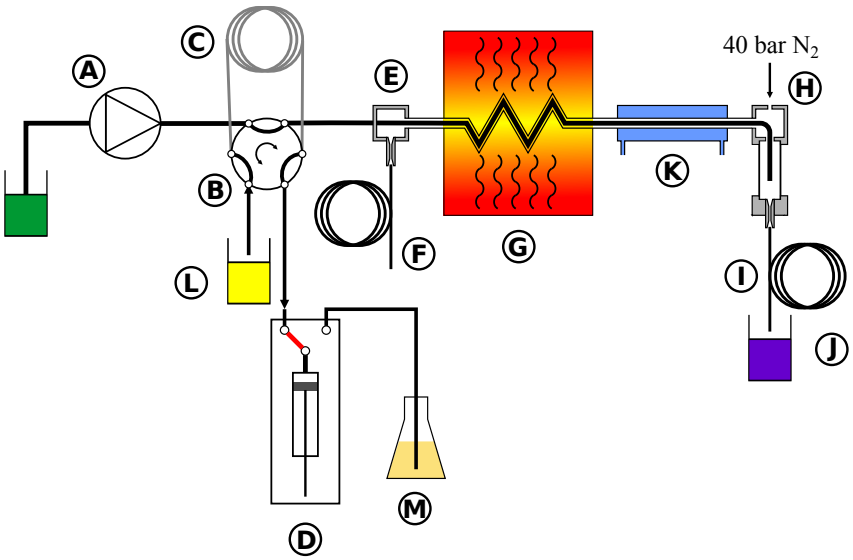

Figure 3.1.: Schematic of the autoflow system. A: high pressure pump for carrier solution, B: 6-port high pressure valve, C: sample loop, D: high precision dispenser for controlled sample uptake, E: exit port of the N_2 pressurizing system, F: N_2 restrictor capillary, G: microwave heated zone, H: gas/liquid separator and N_2 inlet, I: sample restrictor capillary, J: collection of the digested sample, K: cooling unit, L: undigested sample, M: rinsing solution.

on the steel tube and the silicone rubber tube was compressed by tightening the packing screw (figure 3.2, H; formed by an 8 mm inner diameter Swagelok® tube fitting, part number SS-8M0-6). The metal tube (figure 3.2, D) itself was also locked in place by this fitting, a metal ferrule (figure 3.2, I) and the corresponding tightening nut (figure 3.2, J). The PFA digestion tube (figure 3.2, K) could be moved freely inside this glass-to-metal interface leaving plenty of space for the high pressure nitrogen to flow around the PFA tube.

The optimized operating conditions are listed in table 3.1.

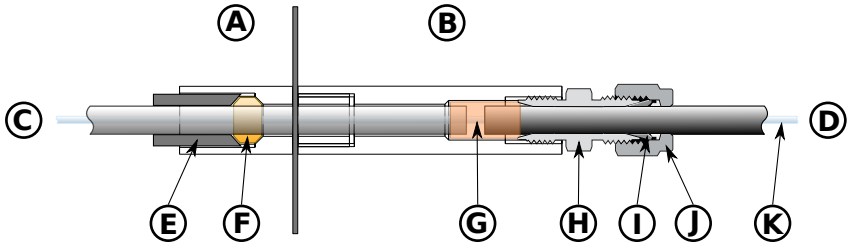

Figure 3.2.: Glas-to-metal interface. A: part inside of microwave oven, B: outside part, C: glass tube, D: metal tubing, E: tightening screw, F: PEEK ferrule, G: silicon rubber tube, H: Swagelok® tube fitting, I: metal ferrule, J: tightening nut, K: PFA digestion tube.

Table 3.1.: Optimized operating conditions of the flow digestion system.

Parameter	Value
Carrier flow rate	2.0 mL min^{-1} of 1 % HNO_3 (v/v)
Sample volume introduced	5 mL
Pressure within the digestion coil	40 bar
Heated volume of the digestion coil	6 mL
Microwave power	400 W
Final volume after digestion	20 mL

3.2.2. Instrumentation

Analytes were quantified with an axially viewed ICP-OES (Ciros Vision EOP, Spectro, Germany) using a cross-flow nebulizer, a Scott type spray chamber and a standard ICP torch with a 2.5 mm inner diameter injector. 1350 W RF power, 12.5 L min^{-1} outer gas flow, 0.6 L min^{-1} intermediate gas flow and 0.83 L min^{-1} nebulizer gas flow were used. The following emission lines were used for analyte quantification: Al 167.078 nm, As 189.042 nm, B 249.773 nm, Ba 455.404 nm, Be 234.861 nm, Bi 190.241 nm, Ca 317.933 nm, Cd 214.438 nm, Co 228.616 nm, Cr 267.716 nm, Cu 219.226 nm, Fe 238.204 nm, Mg 280.270 nm, Mn 257.611 nm, Mo 202.030 nm, Na 588.995 nm, Ni 231.604 nm, Pb 220.353 nm, Sb 206.833 nm, Se 196.090 nm, Sr 407.771 nm, Ti 334.941 nm, V 292.464 nm and Zn 213.856 nm.

Using the conditions reported in table 3.1 and 1 % sample slurries (m/v), the LOQs were 4, 12, 8, 16, 8, 11, 10, 4, 12, 16, 20 and 8 mg kg^{-1} for Al, B, Ca, Cr, Cu, Fe, Mg, Mn, Na, Ni, Pb and Zn respectively. The LOQs were calculated from calibration functions (0 – 1 mg L^{-1}; 5 concentration levels, 5 replications; 95 % confidence level) and corrected for the sample dilution. LOQs are only given for elements analyzed in CRMs or real samples. RSDs were below 3 % in all ICP-OES measurements. Scandium (Sc 361.384 nm) was used as an internal standard at a concentration of 1 mg L^{-1} throughout.

Residual carbon content (RCC) in digests was determined using a total organic carbon analyzer (TOC-5050, Shimadzu, Japan) or ICP-OES (C 193.091 nm emission line).

Closed vessel microwave assisted digestions were performed in standard ceramic supported PFA vessels using a commercial microwave digestion system (Multiwave 3000, Anton Paar GmbH, Austria). About 0.5 g solid sample or 5 g liquid sample were mixed with the digestion acids (HNO_3, or cocktails of HNO_3 and HCl or HF). For 5 minutes the microwave power was ramped to 1400 W and thereafter the sample was digested for additional 15 minutes at the maximum permissible vessel pressure (40 bar).

The acid concentration in the digested samples was determined by manual titration with 0.1 mol L^{-1} NaOH (Roth, Germany) using phenolphthalein as an indicator.

3.2.3. Reagents, certified reference materials and samples

Purified water (18 MΩ cm, Barnstead Nanopure, Thermo Fisher Scientific, USA) and high purity acids (HCl and HF Suprapur, Merck, Germany; HNO_3 purified by subboiling in a quartz still) were used throughout. Calibration standards were prepared from a 100 mg L^{-1} multi element solution (Roth, Germany) in 3 % HNO_3 ($^{v}/_{v}$). Calibration solutions for the determination of the residual carbon content were prepared from potassium hydrogen phthalate (*p.a.* quality, Merck, Germany).

Six certified reference materials (CRMs) were used in this work: BCR 62 (olive leaves), CNRC DORM-2 (dogfish muscle), NIST SRM 1515 (apple leaves), NIST SRM 1547 (peach leaves), NIST SRM 1567 (wheat flour) and NIST SRM 1568 (rice flour).

For initial system characterization commercially available milk powder (Aptamil Folgemilch, Milupa, Austria), apple juice (Spar, Austria) and orange juice (Spar, Austria) were used.

Slurries with 1 % solids were prepared by thoroughly mixing the solid sample with water, adding concentrated acids and making up to volume with water afterwards. Thereby sample clotting was avoided. Liquid samples were diluted with the relevant concentrated acids.

3.3. Results and discussion

3.3.1. Optimization of the microwave field uniformity

A common problem in multimode microwave cavities is the inhomogeneous distribution of microwave radiation. To investigate this effect 12 glass vials (volume: 14 mL) filled with 10 mL 3 % HNO_3 were placed in a circular arrangement (equally spaced, radius: 250 mm, height above cavity floor: 170 mm) inside the microwave cavity. This setup matched the position of the glass digestion coil inside the cavity. After heating for 60 seconds with 400 W the temperature of each vessel was quickly determined with a digital thermometer (300 K, Voltcraft, Taiwan). The error of the temperature measurement was found to be dominated by the cooling of the liquid in the vials during the measurement as the vial temperature

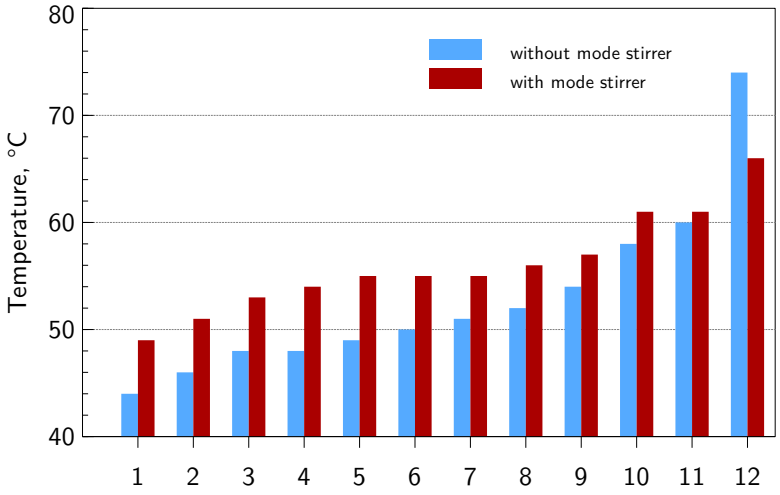

Figure 3.3.: Temperature distribution inside the microwave cavity with and without a spinning mode stirrer. Values arranged with increasing temperature; error bars not shown for clarity.

was measured consecutively rather than simultaneously. Based on repeated measurements of the same vial an error of 3 °C was estimated. The experiment was repeated with a mode stirrer (140 mm diameter aluminum disc with six wings bent 80 mm upwards) installed inside the microwave cavity. This mode stirrer was spun by the digestion vessel rotation mechanism of the Multiwave 3000.

Without the mode stirrer the temperature in the glass vials ranged from 44 to 74 °C with a median of 51 °C. By using the mode stirrer the temperature profile inside the microwave cavity flattened as shown in figure 3.3. The temperature of the diluted nitric acid ranged from 49 to 66 °C with a median of 55 °C. Moreover, the homogeneity of the microwave radiation in the region of the digestion coil could be improved. Consequently the mode stirrer was used throughout the remaining experiments.

3.3.2. Optimization of the digestion parameters

The residual carbon content (RCC) is commonly used to assess the completeness of a digestion. Based on previous experience glucose and glycine were selected as test substances for RCC determination as their behavior during acid digestion is known to be very different [16]. Glucose tends to react violently with nitric acid upon reaching the digestion temperature and serves as a “stress test” for the flow digestion system. Glycine on the other hand is difficult to digest completely.

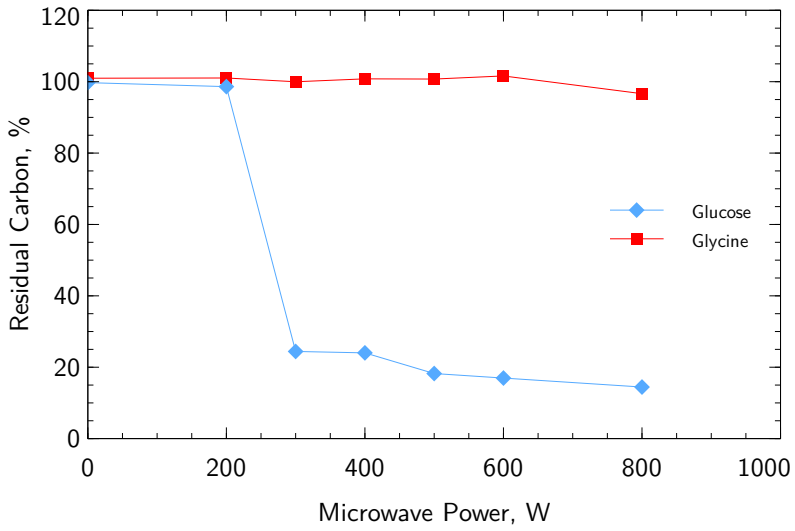

Figure 3.4.: Effect of microwave power on the digestion efficiency of glucose and glycine expressed as RCC, n = 3, error bars smaller than the dots.

The effect of microwave power on the completeness of the digestion was evaluated using solutions of 25 g L^{-1} glucose or 28 g L^{-1} glycine in 30 % nitric acid (v/v) and the instrument conditions reported in table 3.1. As shown in figure 3.4 the decomposition of glucose starts at a power level of 300 W resulting in a RCC of 24 ± 1 % (mean value ± standard uncertainty). With increasing power the RCC decreased almost linear to 14.4 ± 0.8 % at 800 W. For glycine the digestion conditions were not aggressive enough: only at a power level of 800 W some of the glycine was completely decomposed resulting in a RCC of 96 ± 1 %. This behavior can be traced to a digestion temperature significantly below the expected 250 °C within the digestion zone. As shown by Pichler *et al.* [16] glycine is digested only at temperatures above 235 °C for a residence time in the heated digestion zone of 3 minutes. From these results it can be estimated that the digestion temperature in the presented system was between 230 and 235 °C. This temperature is also in good agreement with the data reported by Pichler *et al.* for glucose. A precise measurement of the temperature within the digestion zone was not possible due to potential microwave leakage and geometrical constraints. We believe that the reason for the somewhat low digestion temperature in the presented flow digestion system is the relatively small overall sample volume of 6 mL in the microwave cavity. This results in reduced microwave energy coupling. Depending on the digested sample matrix, all further experiments were conducted with either 400 or 600 W.

It is important to note that even at 800 W the magnetron temperature remained below 60 °C. An experiment with 1000 W was also attempted, but the magnetron temperature increased quickly tripping the microwave digestion ovens over-temperature control circuit. According to the instrument manufacturer, below 1000 W both magnetrons share the power

load, each providing one half. Above 1000 W one magnetron operates at full rated power whereas the second one is used for power regulation. Compared to pressurized flow digestion systems employing mono mode cavities (typically about 100 W) [16], the power level in this setup was far higher.

Due to the relatively large multimode cavity the microwave coupling to the liquid phase inside the digestion coil was low. Consequently, a reduction of the chamber height by a factor of 1.6 was investigated. A tight fitting grounded aluminum sheet was installed inside the microwave cavity reducing its height from 350 mm to 225 mm but leaving length and width unchanged. In a similar experiment to the one above, no significant change in the RCC was encountered for glucose and glycine. The aluminum sheet was therefore not used further on.

The carrier flow rate defines the residence time of the sample in the microwave heated zone. Decreasing the carrier flow rate is not only known to improve the digestion efficiency but also to lengthen the overall time needed to process the sample. The effect of the carrier flow rate on the RCC was investigated using a test solution of $28\,\mathrm{g\,L^{-1}}$ glycine in 30 % nitric acid (v/v) and the instrument conditions reported in table 3.1. Reducing the carrier flow rate from $2\,\mathrm{mL\,min^{-1}}$ to $0.5\,\mathrm{mL\,min^{-1}}$ led to a near linear decrease of the RCC from 99 ± 1 to 89 ± 2 % for glycine as shown in figure 3.5. It is important to note that by reducing the carrier flow rate the digestion time for one sample increased from 10 to 40 minutes. This was deemed impractical and unjustified by the small reduction in RCC despite the high degree of automation in the presented system. Thus the carrier flow rate was set to $2\,\mathrm{mL\,min^{-1}}$ for all further experiments. A stopped flow mode of digestion was not attempted with the presented system.

Increasing the sample volume inside the microwave cavity might be another approach to improve the RCC. Thereby the total volume of liquid inside the cavity would be increased. It was found that regardless of the large radius of the glass coil the introduction of the PFA tube into the coil was not possible for glass coils with more than three turns. During initial tests it was attempted to introduce the PFA tube into a six turn coil. This failed even with the ample use of ethanol as a lubricating agent (PTFE spray or low viscosity oil proved to be inferior to ethanol) after about three and a half turns. The radius of the glass coil was not further altered, as a smaller radius would have worsened the above mentioned problems with the PFA tube and a much larger coil radius was not possible due to the cavity size.

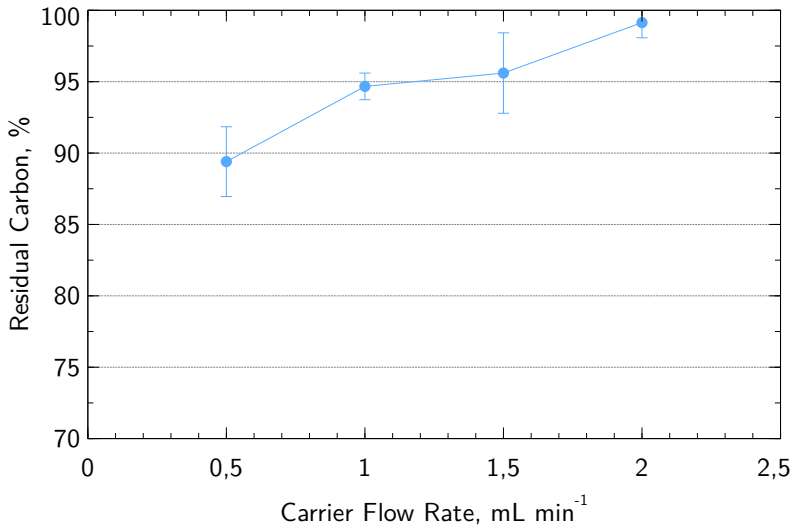

Figure 3.5.: Effect of the carrier flow rate on the digestion efficiency of glycine at 400 W microwave power, n = 5.

3.3.3. Comparison between flow digestion and closed vessel batch digestion

Typical samples processed in flow digestion systems are fruit juices and milk powder. Two juice samples were investigated in this work: clear apple juice and orange juice with pulp. Each sample was acidified with nitric acid to a final concentration of about 30 % HNO_3 ($^{v}/_{v}$) prior to high pressure flow digestion. For the digestion of commercial milk powder a slurry (1 % $^{m}/_{v}$) was prepared. All samples were clear and colorless after digestion. The same samples were also digested in a common closed vessel batch digestion procedure.

The data presented in table 3.2 show that generally there is no significant difference between high pressure flow digestion and closed vessel batch digestion in all three matrices on the 95 % confidence level. For Ca, Mg and Na in orange juice a STUDENT t-test indicated differences between the two digestion principles with lower values attained by flow digestion. We attribute these findings in closed vessel digestion to contamination during sample transfer.

3.3.4. Effect of the digestion acid cocktail

The efficiency of a digestion is often described by the RCC. As already shown, this parameter is heavily affected by the sample matrix. Moreover, no information is provided on the tolerance of the flow digestion system towards the acid cocktail. Using a CRM (NIST SRM

Table 3.2.: Comparison of flow and closed vessel batch digestion of milk powder, apple and orange joice, mean value ± standard uncertainty, n = 5, 95 % confidence level, ND: not determined.

	Apple juice		Orange juice		Commercial milk powder	
	Flow digestion	Closed vessel digestion	Flow digestion	Closed vessel digestion	Flow digestion	Closed vessel digestion
	$mg\,kg^{-1}$	$mg\,kg^{-1}$	$mg\,kg^{-1}$	$mg\,kg^{-1}$	$mg\,kg^{-1}$	$mg\,kg^{-1}$
B	2.2 ± 0.2	2.16 ± 0.06	0.99 ± 0.04	1.06 ± 0.03	ND	ND
Ca	130 ± 2	132 ± 3	154 ± 2	162 ± 3	3.90 ± 0.08	4.1 ± 0.2
Cu	< LOQ (0.2)	< LOQ (0.2)	0.18 ± 0.01	0.19 ± 0.02	ND	ND
Fe	3.9 ± 0.2	4.1 ± 0.3	0.8 ± 0.2	1.0 ± 0.2	0.062 ± 0.002	0.073 ± 0.007
Mg	59 ± 4	62 ± 1	111 ± 2	121 ± 3	0.32 ± 0.01	0.33 ± 0.02
Mn	0.50 ± 0.03	0.52 ± 0.02	0.23 ± 0.01	0.26 ± 0.01	ND	ND
Na	31.6 ± 0.5	32 ± 1	17.6 ± 0.2	20 ± 1	1.17 ± 0.08	1.21 ± 0.04
Zn	0.08 ± 0.01	0.06 ± 0.01	0.15 ± 0.01	0.15 ± 0.01	0.032 ± 0.002	0.034 ± 0.002

1547, peach leaves) the effect of different digestion acid cocktails on both the flow digestion system itself and the analytical characteristics of the digests was investigated. In each run 5 mL of a 1 % slurry ($^{m}/_{v}$) were introduced into the flow digestion system.

The effect of different acid cocktails on the digestion of NIST SRM 1547 (peach leaves) is shown in table 3.3. For Ca and Mg all acid cocktails resulted in good agreement between the determined and the certified values. The obtained values of B and Mn were slightly lower and the results of Na are slightly higher than the certified values irrespectively of the digestion acid mixture indicating other processes than the sample digestion. It is important to note, that for all acid cocktails used, the analyte concentration in the blank digestions (only acid) was below the respective limit of quantification. For Al only about 28 % of the certified value was obtained if just nitric acid was used for digestion. If on the other hand HF was present in the digestion acid cocktail, close agreement between the obtained and the certified concentrations was found. This behavior is well known from closed vessel batch digestion.

In general, the composition of the digestion acid cocktail is of great importance for complete digestion. Only by means of that, low analyte results can be avoided. Consequently, a digestion system should not pose limits on the composition of the acid cocktail. Until now this goal has not been reached for high pressure flow digestion systems. Even dissolution coils made of Pt/Ir (80 % Pt, 20 % Ir) – despite their excellent stability towards HNO_3 and HF [27] – are reported to be attacked by HNO_3/HCl mixtures [29]. One clear advantage of the present flow digestion system is the absence of metals in any part of the system which is in contact with concentrated acids. As a result, a high degree of freedom is given to the selection of the digestion acid cocktail composition.

Table 3.3.: Comparison of different acid cocktails for the digestion of NIST SRM 1547 (peach leaves), mean value ± standard uncertainty, n = 3, 95 % confidence level, ND: not determined, all acid concentrations in $^{v}/_{v}$.

	Determined					
	30 % HNO_3	30 % HNO_3, 3.6 % HCl	30 % HNO_3, 3 % H_2O_2	30 % HNO_3, 3.6 % HCl, 1.3 % HF	Certified	
Al	70 ± 3	132 ± 18	160 ± 20	240 ± 10	249 ± 8	$mg\,kg^{-1}$
B	27.2 ± 0.9	23 ± 1	25.1 ± 0.9	ND	29 ± 2	$mg\,kg^{-1}$
Ca	15 ± 1	14.8 ± 0.1	14.8 ± 0.1	11.4 ± 0.4	15.6 ± 0.2	$g\,kg^{-1}$
Mg	3.94 ± 0.2	3.88 ± 0.06	3.88 ± 0.02	3.18 ± 0.06	4.32 ± 0.08	$g\,kg^{-1}$
Mn	93 ± 3	91.2 ± 0.6	91.9 ± 0.6	91 ± 1	98 ± 3	$mg\,kg^{-1}$
Na	ND	39 ± 2	31 ± 3	ND	24 ± 2	$mg\,kg^{-1}$

3.3.5. Method validation

Five certified reference materials of biological samples were analyzed in order to verify the accuracy of the flow digestion procedure. The acid cocktails were selected based on previous experience in closed vessel batch digestion of these materials. In each run 5 mL of a 1 % slurry ($^{m}/_{v}$) were introduced into the flow digestion system.

The results of the CRM analysis listed in table 3.4 are in good agreement with the certified values. It should be noted that regardless of the large number of stainless steel components in the presented high pressure flow digestion system no significant contamination of the samples with Fe, Cr or Mn was encountered. Moreover, the titanium components in the HPLC pump used for carrier flow generation did not result in significant contamination either. The concentration of Fe, Cr, Mn and Ti in blank solution digests prepared by injecting the diluted acid rather than the sample slurry was below the respective LOQ (11, 16, 4 and 8 $mg\,kg^{-1}$ for Fe, Cr, Mn and Ti; values corrected for the sample dilution caused by the digestion). This clearly demonstrates the effectiveness of the countercurrent flow of nitrogen that is used to pressurize the digestion coil.

The RCC (mean value ± standard uncertainty, n = 3, 95 % confidence level) values after high pressure flow digestion were 35 ± 2, 40 ± 2, 11.6 ± 0.6 and 10.6 ± 0.6 % for BCR 62 (olive leaves), NIST SRM 1515 (apple leaves), NIST SRM 1567 (wheat flour), and NIST SRM 1568 (rice flour), respectively. It is important to note that all digests were clear and without any visual particles.

Spike recoveries were obtained from 1 % slurries of commercial milk powder in 30 % HNO_3 ($^{v}/_{v}$) fortified prior to flow digestion with Al, As, Ba, Be, Bi, Cd, Co, Cr, Cu, Fe, Hg, Mg, Mn, Mo, Ni, Pb, Sb, Se, Sr, Ti, V, and Zn. The final concentration in the digested samples

Table 3.4.: High pressure flow digestion of CRMs, mean value ± standard uncertainty, n = 3, 95 % confidence level, all acid concentrations in %.

		Determined	Certified	
BCR 62 (olive leaves) 30 % HNO_3, 3.6 % HCl, 0.8 % HF	Al	415 ± 9	450 ± 20	$mg\,kg^{-1}$
	Cu	42 ± 1	46.6 ± 1.8	$mg\,kg^{-1}$
	Mn	53.9 ± 0.9	57.0 ± 2.4	$mg\,kg^{-1}$
	Pb	22 ± 1	25.0 ± 1.5	$mg\,kg^{-1}$
	Zn	13.5 ± 0.6	16.0 ± 0.7	$mg\,kg^{-1}$
DORM-2 (dogfish muscle) 20 % HNO_3, 6 % HCl	Al	5 ± 1	10.9 ± 1.7	$mg\,kg^{-1}$
	Cr	37.2 ± 0.6	34.7 ± 5.5	$mg\,kg^{-1}$
	Fe	153.2 ± 0.6	142 ± 10	$mg\,kg^{-1}$
	Mn	3.99 ± 0.02	3.66 ± 0.34	$mg\,kg^{-1}$
	Ni	23 ± 2	19.4 ± 3.1	$mg\,kg^{-1}$
	Zn	19.7 ± 0.7	25.6 ± 2.3	$mg\,kg^{-1}$
NIST SRM 1515 (apple leaves) 30 % HNO_3, 3 % HF	Al	290 ± 10	286 ± 9	$mg\,kg^{-1}$
	Ca	14.5 ± 0.2	15.26 ± 0.15	$g\,kg^{-1}$
	Fe	68 ± 1	83 ± 5	$mg\,kg^{-1}$
	Mg	2.49 ± 0.04	2.71 ± 0.08	$g\,kg^{-1}$
	Mn	49.7 ± 0.7	54 ± 3	$mg\,kg^{-1}$
	Zn	11.9 ± 0.7	12.5 ± 0.3	$mg\,kg^{-1}$
NIST SRM 1567 (wheat flour) 30 % HNO_3	Ca	186 ± 6	190 ± 10	$mg\,kg^{-1}$
	Fe	20 ± 1	18.3 ± 1.0	$mg\,kg^{-1}$
	Zn	17 ± 4	10.6 ± 1.0	$mg\,kg^{-1}$
NIST SRM 1568 (rice flour) 30 % HNO_3	Ca	136 ± 7	140 ± 20	$mg\,kg^{-1}$
	Mn	17.5 ± 0.9	20.1 ± 0.4	$mg\,kg^{-1}$
	Zn	21.4 ± 0.9	19.4 ± 1.0	$mg\,kg^{-1}$

was $1\,mg\,L^{-1}$ for each element. The spike recoveries for all elements listed were between 94 and 105 % (RSDs below 3 % for all elements; n = 4), with the exception of Hg. For Hg the spike recovery was 89 % indicating some losses in the PFA digestion tube.

The acid concentration after flow digestion in these milk power samples was $3.8 \pm 0.1\,mol\,L^{-1}$ (mean ± standard uncertainty; 95 % confidence level). The high acidity in the digested samples is typical for conventional acid digestion. It is interesting to note that recently new digestion techniques for lower sample acidity adverted: they involve the use of UV radiation during digestion and allow a significant reduction of acid consumption [33].

3.4. Conclusion

With the presented high pressure flow digestion system it was possible to digest samples fully automated at a pressure of up to 40 bar. The reason for the relatively high RCC values for glycine can be expected to originate from the inefficient coupling of microwave energy

Table 3.5.: Comparison with other flow digestion systems reported in the literature.

	Presented high pressure flow digestion system	Ambient pressure continuous flow digestion systems	Ambient pressure closed flow and stopped flow digestion systems	Medium pressure continuous flow digestion systems	Medium pressure stopped flow digestion systems	Conductively heated high pressure flow digestion systems
Reference(s)		[10, 17, 19, 34, 35]	[36–38]	[11, 39]	[13, 14, 40]	[7, 28, 29]
System pressure	40 bar	1 bar		2 – 25 bar		up to 200 bar
Digestion temperature	~ 230 °C	~ 120 °C		180 – 200 °C		up to 300 °C
System tolerates HF, HCl and/or H_2O_2	Yes	Yes	Yes	No	No	No

into the small sample volume (6 mL) situated in the rather large multimode cavity. This is consistent with data obtained at a very low carrier flow of 0.5 mL min^{-1}. The reduction of the RCC under these conditions can be explained by the long residence time of the sample in the microwave irradiated zone. Nevertheless, good agreement with certified values was achieved and the results were similar to closed vessel batch digestion. In contrast to most published pressurized flow digestion systems the present system did not limit the selection of the digestion reagents. Even prolonged system operation with acid cocktails of HNO_3, HF and HCl did neither result in sample contamination by dissolved structural materials nor in significant corrosion of the system. Furthermore, no signs of element specific losses [30] were encountered. Another advantage of the presented system is the fully automated processing of samples. After loading the sample slurries to the autosampler the digestion process is performed autonomously and without the risk of contamination due to various sample handling steps commonly necessary in closed vessel batch digestion protocols. The presented high pressure flow digestion system is capable of digesting up to six samples per hour using the operating conditions listed in table 3.1. A comparison with other flow digestion systems reported in the literature is shown in table 3.5.

3.5. Acknowledgements

The authors acknowledge the help of Armin Bacher for his support in the initial optimization experiments. Günter Fellner is thanked for machining most of the components of the presented system.

CHAPTER 4

Microwave Induced Combustion

Sandra M. Cruz, Paul Tirk, Flavia M. Dalla Nora, Lucas Schmidt, Helmar Wiltsche, Cezar A. Bizzi, Günter Knapp and Erico M. M. Flores

The following chapter was published in "Fuel", Volume 160 (2015), pages 108 – 113 under the title "Feasibility of Sulfur Determination in Diesel Oil by Inductively Coupled Plasma Optical Emission Spectrometry after Microwave-Induced Combustion Using Flame Retardant" [2].

Abstract

Diesel oil sample preparation for further sulfur determination in fuels is considered a critical step during the analytical sequence mainly due to the high volatility of this sample. Combustion systems have been a suitable alternative to conventional digestion methods but its applicability for highly volatile matrices like diesel oil is restrict to low sample masses due to the high pressure generated during combustion. In order to overcome this limitation, the possibility of employing glass wool as a flame retardant for the microwave-induced combustion (MIC) method was investigated in the present work for further sulfur determination by inductively coupled plasma optical emission spectrometry. Using flame retardant it was possible to burn up to 400 mg of diesel oil without increasing the pressure in dangerous levels. Nitric acid (2, 4, 7 or 14.4 mol L^{-1} HNO_3) was evaluated as absorbing solution and no significant difference was observed in sulfur recoveries for solutions. Digestion efficiency was evaluated by means of residual carbon content determination, which presented values always lower than 1 % showing the high digestion efficiency. For comparison of results, S was also determined by the ASTM D 5453-12 method and an agreement better than 95 % was obtained. The accuracy was better than 97 % (analysis of certified reference material), blanks were negligible and the limit of detection was considered as suitable for quality control (2 µg g^{-1}).

4.1. Introduction

Diesel oil belongs to a class of products obtained by crude oil processing and generally covers the range of boiling temperatures between 175 and 375 °C mainly presenting compounds with about eight to twenty-four carbon atoms (C_8 to C_{24}) [41, 42]. Sulfur is an ubiquitous element in crude oil and the presence of sulfur compounds in diesel oil or in the middle distillate crude oil fraction can cause corrosion leading to damage of metallic parts of refineries as well as of combustion engines of automobiles [41, 43, 44]. Other implications include changes in color, odor and instability of the final product. Remaining sulfur also contributes to the release of sulfur oxides into the atmosphere causing environmental pollution like acid rain [43, 45, 46]. Furthermore, it can poison the catalysts used in emission control systems, consequently, reducing the oxidation effectiveness of carbon monoxide, hydrocarbons and volatile organic compounds [41, 43, 44]. Sulfur compounds are distributed in several crude oil distillation fractions and may also be present in the final products [47]. Depending on the origin of formation and maturation conditions of the preceding crude oil, a variety of sulfur compounds can be found [47] and their presence, especially in low and ultralow sulfur content diesel oil, is generally belonging to the group of benzothiophenes (BT) and dibenzothiophenes (DBT) as well as derivatives of these compounds containing alkyl substituents, such as 4,6-dimethyl-dibenzo-thiophene (4,6-DMDBT) [43, 48].

Refineries and manufacturers are subject to meet the requirements set by governmental organizations. The Environmental Protection Agency (EPA, United States) limits the allowed sulfur concentration for ultra low sulfur diesel to $15\,\mathrm{mg\,kg^{-1}}$ [49]. Similar restrictions also exist in European Union as the directive 98/70/EC which sets a limit even lower ($10\,\mathrm{mg\,kg^{-1}}$) [50]. In order to comply with these regulations the continuous monitoring of sulfur is of high importance in the production and quality control of diesel oil.

For sulfur determination in diesel oil, sample preparation can be considered as a critical step and several methods have been applied in last years [4]. Direct injection of diesel oil for further inductively coupled plasma based analysis has been currently used for routine analysis. However, some drawbacks still remain as the need for high dilution factors to maintain a stable plasma [51], oxygen addition to nebulization gas and also the use of reference solutions especially prepared in organic medium [52]. Even using matrix-matched reference samples, changes in plasma can occur making direct injection of organic substances prone to some inconveniences for trace S determination [53–55]. Alternatively, sulfur determination in crude oil and its fractions has been carried out by X-ray fluorescence (XRF) and also by sample combustion with further titration or infrared

Table 4.1.: Analysis of lubricating oil, diesel oil and crude oil products using oxygen flask and combustion bomb for further S determination.

Sample	Digestion method	Technique of determination	LOD	References
Lubricating oil	Combustion bomb	IC	1.62 %	[63]
Diesel oil	Combustion bomb	ICP-OES	—	[64]
Fuel	Combustion bomb	IC	0.07 µg mL^{-1}	[66]
Crude oil products	Combustion bomb	Titration	0.01 %	[67]
Fuel oils	Oxygen flask	IC	0.007 %	[68]

detection [56–60]. Despite some automatic sulfur analyzers allow the direct analysis of diesel oil, common procedures for S determination by other techniques involve a previous step of sample preparation [25]. However, acid digestion procedures can present limitations due to the relatively long time required [61] and low digestion efficiency [62]. As an example, Ulrich *et al.* [53] proposed a procedure involving a 12 h pre-digestion on a hot plate before applying microwave radiation for 30 min.

On the other hand, combustion systems provide some advantages over closed vessel wet digestion when dealing with organic samples. Due to the high temperature during combustion (> 1000 °C) complete oxidation of sample matrix can be achieved, resulting also in low residual carbon content (RCC) [63]. Classical combustion is normally performed in bombs or oxygen flasks [63, 64]. Both systems present some advantages mainly related to sample ignition and low risk of contamination, respectively [9, 63]. However, for combustion bombs, the use of acid solutions must be avoided to prevent damage to the metallic vessel walls and low analytical frequency may be considered as one of the main limitations for this system [63]. The oxygen flask method presents restriction to the maximum sample mass and consequently poor limit of detection (LOD). In addition, both systems need continuous attention by the analyst, only one sample is processed in each run and digestion time is relatively long (up to 3 h considering the cooling step in case of combustion bombs) that decreases the throughput [63]. Normally, for the oxygen flask system, samples of 10 to 50 mg are burnt in vessels with a volume of 250 to 500 mL [65]. Table 4.1 summarizes some selected applications using combustion bombs and oxygen flask, for the subsequent determination of sulfur in oils, fuels, lubricants oil and crude oil products [63, 64, 66–68].

Alternatively, microwave-induced combustion (MIC) can overcome some of the mentioned difficulties and often provides an easy and rapid way for decomposing organic samples [62, 69, 70]. Essentially, solid samples are pressed as pellets and ignited using microwave radiation with a suitable igniter solution [71]. Analytes are retained in a convenient absorbing solution [65] and it should be noticed that the acid concentration can be much lower using the MIC method when compared to conventional closed vessel wet digestion

because the oxidation of organic matter is mainly promoted by the oxygen present in the gas phase [72]. As a result, interferences during measurement step by inductively coupled plasma based techniques are minimized and the use of hazardous substances are reduced thus leading to a greener procedure [55, 73, 74]. Furthermore, microwave heating can be used for a reflux step without opening the combustion vessel in order to improve analyte recovery [71].

However, problems are observed when working with viscous or liquid samples because they can not be prepared as pellets and keeping sample on the sample holder is crucial to ensure complete combustion. In case of combustion of crude oil, a method using polyethylene film to wrap the samples was developed in a previous study for S determination in extra heavy crude oil after MIC by inductively-coupled plasma optical emission spectrometry (ICP-OES) [71]. However, taking into account the presence of highly flammable organic substances, a rapid pressure increase could occur resulting in risks of explosion.

Taking into account the combustion reaction of highly flammable matrices such as diesel oil and the possibility of using a solid flame retardant, it is expected to achieve a safe combustion procedure without decreasing the sample mass [75]. Flame retardants are known to act chemically and/or physically in solid, liquid or gas phase [76]. By employing this kind of material it is possible to decrease the combustion rate, making the oxidation reaction safer when it is applied to highly flammable or volatile samples.

In this sense, the present work aims to evaluate the use of glass wool as a flame retardant for digesting a relatively high mass of diesel oil by the MIC method. Final digests were analyzed by ICP-OES for sulfur determination. The absorbing solution was optimized in order to obtain quantitative analyte recoveries. The maximum sample mass allowing a safe and complete combustion was evaluated by considering the efficiency of sample decomposition (assessed by RCC determination). In addition, a certified reference material (NIST SRM 1084a, wear metals in lubricating oil) and a method recommended by ASTM D 5453-12 [77] were used in order to check the accuracy of the proposed method.

Table 4.2.: Operational conditions used for sulfur and carbon determination by ICP-OES.

Parameter	
RF power	1400 W
Plasma gas flow	15.0 L min^{-1}
Auxiliary gas flow	0.90 L min^{-1}
Nebulizer gas flow	0.75 L min^{-1}
Sample flow rate	2.1 mL min^{-1}
Spray chamber	Cyclonic
Nebulizer	GemCone®
Wavelength	S 180.669 nm C 193.030 nm

Table 4.3.: Operational conditions used for sulfur determination by using an automatic sulfur analyzer (Antek 9000NS).

Parameter	
Ar carrier flow	140 mL min^{-1}
O_2 carrier flow	20 mL min^{-1}
O_2 flow in combustion tube	450 mL min^{-1}
Temperature of combustion tube	1050 °C
Injection volume	10 µL

4.2. Materials and methods

4.2.1. Instrumentation

A microwave oven (Synthos 3000, Anton Paar, Austria) equipped with high-pressure quartz vessels (80 mL, maximum pressure and temperature of 80 bar and 280 °C, respectively) was used for digestions using the MIC method. In this system, the sample is placed on a quartz holder, which is introduced into the vessel. For visualization of combustion a polycarbonate protection wall (45 × 60 cm, 10 mm thickness) was used in front of the microwave oven as a shield to assure safe conditions during these experiments. However, it was not necessary for normal application of combustion system as vessels are equipped with vent valves and rotor is covered with a polypropylene shield.

An inductively coupled plasma optical emission spectrometer (Optima 4300 DV, Perkin Elmer, United States) was used for the determination of S (and also C for digestion efficiency evaluation). Sulfur determination was also performed using a sulfur analyzer (9000NS, Antek Instruments Inc., United States) according to the ASTM D 5453 method [77]. The operational conditions for both ICP-OES and the sulfur analyzer are described in Tables 4.2 and 4.3, respectively.

Diesel samples and glass wool used as flame retardant were weighed using an analytical balance (model AY 220, max. 220 g, 0.1 mg of resolution, Shimadzu, Japan) and introduced into the vessels using a homemade quartz holder.

Argon (99.999 %, White Martins-Praxair, Brazil) was used for plasma generation in ICP-OES and the sulfur analyzer. Oxygen (99.6 %, White Martins-Praxair) was used in the MIC system and the sulfur analyzer.

All statistical comparisons were performed using statistical software (GraphPad InStat Software Inc., Version 3.00, 1997). A significance level of 95 % was selected for all comparisons.

4.2.2. Samples, reagents and standards

High purity water (18.2 MΩ cm) was used for preparing all reagents and standard solutions. Nitric acid (65 %, Merck, Germany) was previously purified in a sub-boiling system (Duopur, Milestone, Italy). Reference solutions for the calibration of ICP-OES were prepared by dilution of a multielement stock solution (10 mg L^{-1} SCP33MS, SCP Science, Canada) in HNO_3 (0.7 mol L^{-1}). Absorbing solutions (2, 4, 7 and 14.4 mol L^{-1} HNO_3) for MIC digestion were prepared by dilution of concentrated acid with water. A solution of 6 mol L^{-1} NH_4NO_3 (Merck) was used as igniter solution for the MIC method [65].

Filter paper (15 mm of diameter, 12 mg, Black Ribbon Ashless, Schleicher and Schuell, Germany) was previously cleaned with 2.8 mol L^{-1} HNO_3 during 20 min in an ultrasonic bath (TI-H-5, 750 W, 35 kHz, Elmasonic, Germany), rinsed with water and dried in a class 100 laminar flow bench before use.

For the optimization of the MIC method, diesel oil samples purchased from local market were used (samples 1, 2 and 3; total organic carbon of 85 %). A standard reference material (NIST SRM 1084a, wear metals in lubricating oil, National Institute of Standards and Technology, United States) with informed value of sulfur content was used to evaluate the accuracy of the proposed procedure.

Glass wool (Pyrex, United States, diameter 0.08 mm) made in borosilicate glass, was used for holding oil samples on the quartz holder (100 ± 5 mg). Glass wool was previously cleaned with 14.4 mol L^{-1} HNO_3 during 15 min (200 °C) using a microwave oven with closed vessels. After, glass wool was rinsed with high purity water and further dried in a laminar flow bench.

4.2.3. Sample digestion by the proposed MIC method

Diesel oil samples were carefully dropped onto glass wool (around 100 mg) using a syringe (glass wool was wetted with diesel oil). In order to assure a suitable adsorption of the samples, the glass wool was prepared in a spherical shape. Subsequently, glass wool with adsorbed diesel oil was kept in a laminar flow bench before combustion (this time was optimized in order to achieve a reproducible combustion). In this work two filter papers were used, contrarily to conventional application of MIC for solid samples where only one filter paper is needed. It allowed a more reproducible combustion that was sometimes incomplete when using only one filter paper. The glass wool containing the adsorbed diesel was placed on the top of filter papers wetted with NH_4NO_3 solution, previously positioned in the quartz holder, which was further inserted into the quartz vessel already filled with 6 mL of the absorbing solution (2, 4, 7 or 14.4 mol L^{-1} HNO_3). Each vessel was pressurized with 20 bar oxygen and microwaves were irradiated during 5 min (1400 W, combustion and reflux step) followed by a cooling step (0 W, 20 min). Final digests were made up with water to 25 mL for further sulfur determination by ICP-OES.

It is important to consider that the allowed pressure rate used in the digestion system had to be adjusted from 0.8 bar s^{-1} to 3 bar s^{-1} because of the rapid increase in pressure occurring during combustion. Between each combustion run the quartz holders and vessels were cleaned with 6 mL of 20 % HNO_3 during 10 min at 1400 W and 20 min of cooling step.

4.2.4. Evaluation of MIC digestion efficiency using a flame retardant

In order to evaluate the digestion efficiency of the proposed MIC method, C determination was performed in final digests using ICP-OES as previously described [78]. For external calibration, carbon reference solutions were prepared by dissolution of citric acid (Merck) in water (concentration ranging from 5 up to 500 mg L^{-1} of carbon), and all samples, blanks and reference solutions were prepared with yttrium as internal standard (1 mg L^{-1}, SpexCertiPrep, United States) [72]. The volatile carbon present in all samples and standards was removed before determination by purging all solutions with argon (0.1 L min^{-1}, 2 min) [72]. The RCC was expressed as the percentage of C that remained in the final digests in relation to the C originally present in the sample.

4.2.5. Evaluation of the proposed procedure accuracy

Accuracy of the proposed procedure was evaluated by using a standard reference material (NIST SRM 1084a, wear metals in lubricating oil), which was performed using the optimized conditions of the MIC method using glass wool. The determination of sulfur was also performed by the direct injection of sample into an automated analyzer equipment for sulfur determination by ultraviolet fluorescence according to the ASTM D 5453-12 method [77] and the obtained results were used as reference values.

4.3. Results and Discussion

4.3.1. Initial experiments without using flame retardant

Initially, the evaluation of the maximum sample mass to be combusted was performed by conventional MIC approach using 50 mg of diesel oil (without the use of glass wool). In this case the diesel oil sample was involved in a small polyethylene (PE) film which was then placed on the quartz holder. The preparation of the PE film, successfully applied to crude oil samples, was described elsewhere [79]. For these tests, using diesel oil combustion was not reproducible, being incomplete in some cases and resulting in final digests presenting suspended black particles. However, using two disks of filter paper, a reproducible combustion was obtained without solid residues in the final digests. Taking into account highly flammable organic substances, the digestion in closed systems presents a risk of rapid pressure increase and therefore, the digestion of higher diesel oil masses by using MIC was carefully performed.

Using sample masses up to 100 mg of diesel the maximum pressure in the system was around 30 bar, which is related to a fast increase of pressure of about 10 bar during combustion (figure 4.1). However, when the sample mass was increased to 200 mg, the maximum pressure was 45 bar corresponding to an increase of 25 bar compared to the initial pressure of oxygen (20 bar). Based on these results, the evaluation of diesel oil masses higher than 200 mg was considered dangerous and no further experiments were performed using PE film or without flame retardant.

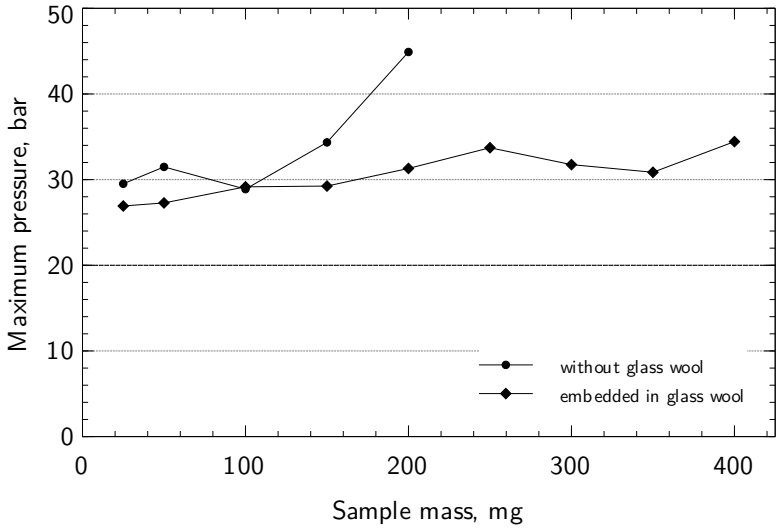

Figure 4.1.: Influence of diesel mass on the maximum pressure during MIC. Combustion method performed without glass wool (•) and using glass wool (◆). Dashed line indicates the inital O_2 pressure of the digestion system (n = 3).

4.3.2. Use of glass wool as a flame retardant

Glass wool was used to reduce the kinetics of the combustion reaction, which was performed by increasing the sample mass step by step while monitoring the maximum pressure in quartz vessels during combustion. Glass wool masses between 75 to 200 mg were evaluated as flame retardants. By using glass wool mass of 100 ± 5 mg or higher (with adsorption time of 120 min) the diesel oil combustion was always complete. Under this condition, the combustion of diesel oil was stable without spillage, and a peak of pressure increase was not observed as before when using PE films. Then, a mass of 100 mg of glass wool was selected for further experiments. In order to obtain reproducible conditions, the time necessary for the adsorption of diesel oil on the glass wool was also evaluated (figure 4.2).

The evaluation of the adsorption time was performed using 200 mg of sample adsorbed on 100 ± 5 mg of glass wool. After diesel oil adsorption, the digestion vessel was pressurized with oxygen and microwave heating program started. When diesel oil was added on the glass wool and vessels were immediately pressurized with oxygen for further microwave heating (considered 0 min of sample adsorption), the sample combustion was not complete. In this case, the peak of maximum pressure during combustion was higher than 45 bar (figure 4.2). This result was similar to those results previously obtained using PE films. (without using glass wool). It was observed for sample adsorption times ranging from 15 to 90 min (pressure peaks of 44 and 38 bar, respectively). Even for the last condition (90 min) presenting a relatively lower increase of pressure, the sample combustion was not

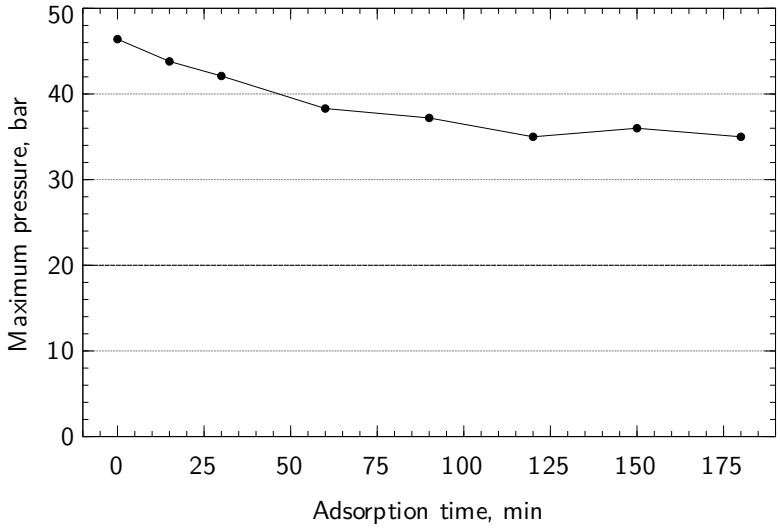

Figure 4.2.: Influence of diesel oil adsorption time on glass wool for the MIC method. Combustion performed using 100 ± 5 mg of glass wool and 200 mg of diesel oil. Dashed line indicates the initial O_2 pressure of the system (n = 3).

reproducible. On the other hand, using higher adsorption time (ranging from 120 up to 180 min), it was observed a practically constant peak pressure (which was always lower than 36 bar). After 120 min of diesel oil adsorption, it presented a stable aspect in glass wool allowing a convenient manipulation (transportation, positioning on quartz holder, *etc.*). As a result, a more strong and stable interaction of glass wool surface with diesel oil was observed, which contributed for decreasing the kinetics of combustion reaction and then reducing the peak pressure. An important aspect to be observed refers to the relatively high amount of oxygen available inside the digestion vessels (20 bar) where, even in this condition, a reproducible and safe combustion could be performed. On the other hand, during combustion, melting of glass wool was observed. The melting process during combustion removes heat from flame that helps to explain the lower increase of pressure during diesel oil combustion. Further experiments were carried out using 100 ± 5 mg of glass wool and 120 min (adsorption time).

Using the selected conditions, higher diesel oil masses (up to 400 mg) were investigated and the maximum pressure observed during sample combustion was relatively low (up to 35 bar, figure 4.1). It can be considered as a low value taking into account that diesel oil combustion should be faster when compared to other solid organic samples [4]. This result shows that the MIC method provides a safe sample preparation even for relatively high diesel oil masses.

Table 4.4.: Determination of S in diesel oil by ICP-OES after digestion using MIC (400 mg of sample mass) with HNO_3 as absorbing solution (results presented as mean ± standard deviation, n = 3).

HNO_3 $mol\,L^{-1}$	Sulfur concentration $\mu g\,g^{-1}$
2	226 ± 8
4	224 ± 8
7	234 ± 13
14.4	230 ± 15

4.3.3. Evaluation of the digestion efficiency

Digestion performed using the MIC method usually results in colorless solutions due to the high oxidation efficiency of organic matter during combustion [62]. It is important to notice that the oxidation efficiency is practically independent of the absorbing solution, which allows the use of very low acid concentration for complete analyte retention. Additionally, it results in further advantages to the subsequent determination step, as well as full compatibility to the selected technique for most of cases.

It is well known that high values of RCC in final digests can cause several interferences in the following determination step especially in case of inductively coupled plasma based techniques [73, 80]. Therefore, an important aspect of MIC for further analysis by ICP-OES or inductively-coupled plasma mass spectrometry (ICP-MS) is that digests can be analyzed practically free of interferences by residual carbon or even by excessive acid concentration. In the present work, a critical evaluation was performed in order to quantify the efficiency of oxidation by measuring the RCC of MIC digests [80–83]. Obtained results were similar to those previously obtained, showing digestion efficiency higher than 99 % (RCC lower than 1 %), even when 400 mg of diesel oil were burnt. It can be considered as an important advantage by taking into account the difficulties involved for digesting such kind of matrix as diesel oil.

4.3.4. Evaluation of the absorbing solution

It has been already discussed in literature that the choice of absorbing solution for MIC method is important to achieve quantitative recoveries and analytes stability in solution [79]. The absorbing solution must be suitable to the kind of analyte and determination technique. In order to evaluate the influence of the absorbing solution on the analytes recovery, nitric acid solutions ranging from 2 to 14.4 $mol\,L^{-1}$ were evaluated (table 4.4).

It was observed that all the evaluated solutions allowed sulfur recoveries higher than 95 %. Although no statistical difference (ANOVA, $P > 0.05$) was obtained between all the

Table 4.5.: Results obtained for the determination of sulfur in diesel oil samples by total sulfur analyzer and by ICP-OES after digestion using MIC (400 mg of sample mass) with 2 mol L^{-1} HNO_3 as absorbing solution (mean ± standard deviation in µg g^{-1}, n = 3).

Diesel oil	MIC µg g^{-1}	Sulfur analyzer (Antek 9000 NS) µg g^{-1}
1	226 ± 8	223 ± 10
2	287 ± 1	275 ± 13
3	< 2[a]	1.49 ± 0.12

[a] Limit of detection

solutions, the results presented in table 4.4 show that in case of using diluted acids the relative standard deviation (RSD) was slightly lower. Therefore, a 2 mol L^{-1} HNO_3 was selected as absorbing solution for further studies. Finally, the possibility of minimizing the acid consumption and consequently reducing the risk of interferences in the determination step by ICP-OES can be pointed out as additional benefits of the proposed method.

4.3.5. Sulfur determination in diesel oil samples after the MIC method

The MIC method was also applied to the digestion of a certified reference material with a similar composition to diesel oil (NIST SRM 1084a, wear metals in lubricating oil), which presents informed values of sulfur concentration. No statistical difference between results obtained by MIC (1714 ± 67 µg g^{-1}, $P > 0.05$) and the informed value (1700 µg g^{-1}) was observed. For comparative purposes diesel oil samples (identified as 1, 2 and 3) were also analyzed according to the ASTM D 5453-12 using an automatic sulfur analyzer for direct analysis of diesel oil. The results were in good agreement with results obtained by the MIC method using diluted HNO_3 (2 mol L^{-1}) and 400 mg of diesel oil (table 4.5).

Using the proposed method, blanks were always negligible and up to eight samples can be processed by each run in 25 min.

Limit of detection and limit of quantification (LOQ) were calculated based on three and ten times, respectively, the standard deviation of sulfur determination in blanks (n = 10). Using the selected conditions the LOQ was considered suitable for S determination in commercial diesel oil samples (6.9 µg g^{-1}) and in agreement with the established limits for S in diesel oil [49, 50].

4.4. Conclusions

In this work, the MIC method was modified in order to circumvent the limitations for combusting highly flammable liquid fuels for further sulfur determination by ICP-OES. By employing glass wool as flame retardant the method was found to be suitable for a safe combustion of diesel oil. Using the optimized MIC conditions, quantitative recoveries of sulfur were obtained after 5 min (combustion and reflux step) using a diluted nitric acid solution (2 mol L^{-1} HNO_3) as absorption medium. The use of glass wool allowed to burn up to 400 mg of diesel oil sample with very low RCC values. Additionally, a high digestion efficiency (> 99 %) was obtained for relatively high sample mass, also avoiding the use of concentrated reagents, and significantly reducing possible interferences in analysis by ICP-OES. Due to the use of relatively high sample mass and diluted absorbing solutions, the LOD was significantly lower (2 µg g^{-1}). Finally, the proposed procedure is in agreement with green chemistry recommendations because it allows the use of diluted solutions, which minimize the generation of residues.

4.5. Acknowledgments

The authors are grateful to CNPq, CAPES and FAPERGS for grants and fellowships.

Part II.

Analysis

CHAPTER 5

Atomic Spectrometry

The term "atomic spectrometry" has its origins in the Latin word "spectrum" (image, apparition) and the Greek word "metria" ($\mu\varepsilon\tau\rho\iota\alpha$, metron = $\mu\varepsilon\tau\rho\rho\nu$, to measure). Quantum theory tells us that matter can interact with electromagnetic radiation. Transitions between different energy levels can be achieved by radiation of the appropriate energy. The excited state can then again release the energy by emitting a photon of the same energy/wavelength. Discovered and described by Kirchhoff and Bunsen, this principle is used in atomic spectrometry to quantify the amount of a certain element by measuring the absorption or emission of light.

Figure 5.1 shows the general schematic of optical atomic spectrometry. Atomization of a sample occurs by means of an energy source such as a flame, a graphite furnace or an inductively-coupled plasma (ICP). Depending on the degree of excitation of the atoms either the emission or the absorption of light is measured. In case of atomic absorption spectrometry (AAS) an additional light source is needed. The light is then received by the spectrometer which discriminates the wavelengths resulting in a spectrum. Lastly, the photons are registered by the detector and evaluated.

Because most of the projects done for this thesis were dealing with ICP-OES, chapter 6 therefore will provide more information about the principles of ICP-OES and its application in analytical instruments. The remaining chapter further explains the fundamentals of atomic spectrometry and the properties of the measured atomic emission/absorption lines.

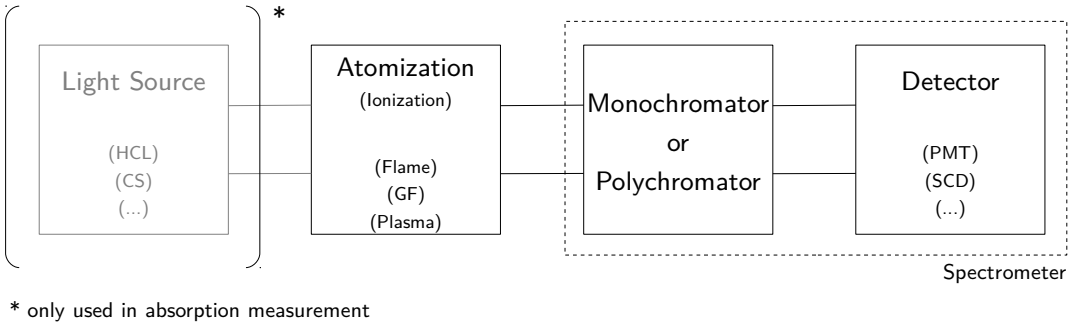

Figure 5.1.: Block diagram of optical atomic spectrometry.

5.1. Fundamentals

One of the most fundamental laws of quantum physics, Planck's law, states that energy can only exist in "packets", so-called "quants". Their minimum amount of energy is h, the Planck constant. Equation 5.1 shows the relation between frequency, wavelength and energy.

$$E = h\nu = \frac{hc}{\lambda} \tag{5.1}$$

For an atomic transition, not only the energy of the incident photon is important, but there are also rules which allow or prohibit certain transitions between different energy levels. A crucial role is played by the transition dipole moment between two states m and n. It is defined as the integral 5.2.

$$\mu_{n,m} = \int \Psi_n^* \hat{\mu} \Psi_m d\tau = \langle \Psi_n \,|\, \hat{\mu} \,|\, \Psi_m \rangle \tag{5.2}$$

The dipole operator $\hat{\mu}$ is constructed by the sum of the individual charges multiplied by their position. In case of the atom it is the sum of the negatively charged electrons and the positively charged protons (equation 5.3).

$$\hat{\mu} = \sum_i q_i r_i = -e \sum_i r_i + e \sum_j Z_j R_j \tag{5.3}$$

The transition between the two states m and n is allowed only when the transition dipole moment is not zero.

The actual intensity of an atomic absorption/emission is dependent on a number of factors such as the transition probabilities $A_{n,m}$, the population of the participating energy levels, the energy difference between the levels and of course the total number of emitting atoms (N, comparable to a concentration). At a given temperature some of the atoms are in the ground state while another part is in the excited state. We can describe the equilibrium between two states by a BOLTZMANN distribution. The probability to find a particle in the state n is given by equation 5.4. It is weighted by the degeneracy g_n and normalized by the partition function $Q(T)$ which represents the sum over all available states (equation 5.5).

$$p_n = \frac{n_n}{N} = \frac{1}{Q(T)} g_n e^{-\frac{E_n}{kT}} \tag{5.4}$$

$$Q(T) = \sum_i g_i e^{-\frac{E_i}{kT}} \tag{5.5}$$

Taking into consideration the factors we mentioned above we can now write out the emission intensity as:

$$I_{n,m} = \frac{h\nu_{n,m}}{4\pi} A_{n,m} n_n \tag{5.6}$$

By substituting n_n with equation 5.4 we get:

$$I_{n,m} = \frac{1}{4\pi} \frac{hc}{\lambda_{n,m}} A_{n,m} \frac{N}{Q(T)} g_n e^{-\frac{E_n}{kT}} \tag{5.7}$$

It should be noted, that even if all quantities are known it is not an easy task to measure absolute line intensities. First of all, emission occurs spherically so the light has to be collected from all sides. Additionally, the spectrometer must be calibrated for the desired wavelengths.

5.2. Spectral Lines

Even though physics and its calculations might give the impression of atomic lines with a definite, "exact" wavelength and a "line"-like appearance, in reality we rather observe an intensity distribution over a certain range of wavelengths. Every atomic absorption/emission line is subject to several broadening processes which alter the appearance – both the width and the profile – of the line. Spectral lines are therefore described by their central wavelength, their line width and their shape. In case of a symmetric peak profile the width can be expressed as full width at half maximum (FWHM) or full width at half area (FWHA). As a consequence for the evaluation of the line intensity the peak area has to be considered (see equation 5.8).

$$S = \int I(\nu) d\nu \tag{5.8}$$

The following sections describe some of the most important causes of line broadening as well as the resulting peak profiles.

5.2.1. Line Broadening

Natural Line Width

If we consider the relaxation of a system from an excited state n to its lower state m we can define the change in the total number of the two states as $-\mathrm{d}N_n = A_{n,m} N_n \mathrm{d}t$. Integrating and setting the initial condition of N_0 particles in state n at the time $t = 0$ gives:

$$N_n(t) = N_0 e^{-A_{n,m} t} \tag{5.9}$$

We can now define the mean lifetime τ of the particles in the excited state as the normalized average (or expected) value for the time.

$$\tau = \langle t \rangle = \frac{\int_0^\infty t N_n(t) \mathrm{d}t}{\int_0^\infty N_n(t) \mathrm{d}t} = \frac{\int_0^\infty t N_0 e^{-A_{n,m} t} \mathrm{d}t}{\int_0^\infty N_0 e^{-A_{n,m} t} \mathrm{d}t} = \frac{1}{A_{n,m}} \tag{5.10}$$

We can conclude that the mean lifetime is indirectly proportional to the transition probability $A_{n,m}$.

Because Heisenberg's uncertainty principle is a fundamental law in the (known) universe all atomic emission lines also suffer from its influences. It states that the impulse and the location of a quantum particle can never be determined both with infinite accuracy. Instead, an uncertainty of around h, the Planck constant, remains.

$$\Delta x \Delta p \sim h \tag{5.11}$$

Another interpretation of the Heisenberg uncertainty principle relates the energy difference to the lifetime of a state.

$$\Delta \tau \Delta E \sim \frac{h}{2\pi} \tag{5.12}$$

Every state has a finite lifetime resulting in a natural line width. Since $E = h\nu$ we can express the uncertainty in lifetime and energy as a wavelength:

$$\Delta \nu = \frac{\Delta E}{h} \sim \frac{1}{2\pi \Delta \tau} \tag{5.13}$$

If the lower state also has a finite lifetime (*i.e.* is not the ground state) we have to combine both the individual lifetimes of two states m and n. Likewise, the probability factors can be added.

$$\Delta \nu = \frac{1}{2\pi} \left(\frac{1}{\Delta \tau_m} + \frac{1}{\Delta \tau_n} \right) \tag{5.14}$$

The exponential decay of the excited states can also be seen as a damped oscillation with a frequency ω_0 (equation 5.15).

$$f(t) = e^{-\frac{t}{\tau}} e^{\mathrm{j}\omega_0 t} = e^{-\frac{t}{\tau}+\mathrm{j}\omega_0 t} = e^{-t\left(\frac{1}{\tau}-\mathrm{j}\omega_0\right)} \tag{5.15}$$

It is possible to describe it as a superposition of frequencies. Using the Fourier transform we can obtain the frequency spectrum of the oscillation $g(\omega)$. The magnitude of the resulting complex function then gives us the frequency distribution as it is recorded in a spectrometer (equation 5.17). This distribution has the form of a LORENTZ function.

$$g(\omega) = \mathcal{F}\left(f(t)\right) = \int_0^\infty f(t) e^{-\mathrm{j}\omega t} \mathrm{d}t = \frac{1}{\frac{1}{\tau} + \mathrm{j}\left(\omega - \omega_0\right)} \tag{5.16}$$

$$I(\omega) = \mathrm{Mag}(g(\omega)) = \frac{1}{\sqrt{\frac{1}{\tau^2} + \left(\omega - \omega_0\right)^2}} \tag{5.17}$$

We can then finally use the expression $\omega = 2\pi\nu$ to convert the angular frequencies ω and ω_0.

$$I(\nu) = \frac{1}{\sqrt{\frac{1}{\tau^2} + 4\pi^2\left(\nu - \nu_0\right)^2}} \tag{5.18}$$

Natural line widths lie in the range of 10^{-5} nm. In comparison to pressure/collisional and DOPPLER broadening this is usually negligible in line width considerations.

Pressure/Collisional Broadening

It is obvious that collisions between particles can shorten the lifetime of a transition. This so-called collisional deactivation is dependent on the rate of collisions which in turn can be influenced by changing the pressure (and to some extent the temperature) in the system. If the number density of particles increases, the likelihood of collisions and therefore the mean free path length and the lifetime of a state are getting shorter. Depending on the type of particle we can distinguish between the STARK effect (for electrons and ions), the VAN DER WAALS broadening (caused by induced dipole fields of atoms) and resonance broadening (energy exchange between same types of particles). The contribution to the line shape is lorentzian for all these effects.

Doppler Broadening

In a plasma the radiating particles are moving rapidly in all directions. As a consequence the apparent frequencies of the emitted photons are changed due to the relative motion from or towards the observer (*i.e.* the spectrometer). This phenomenon is called the Doppler effect. The velocities of the particles are distributed according to a Maxwell distribution. Because the particle speed is well below light speed, we are allowed to define the apparent frequency as $\nu = \nu_0 \left(1 + \frac{v}{c}\right)$. Then, the velocity distribution of the particles becomes (with $\frac{\mathrm{d}n(v)}{N}$ being the fraction of particles with the respective velocity v):

$$\frac{\mathrm{d}N(v)}{N} = \sqrt{\frac{m}{2\pi kT}} e^{-\frac{mv^2}{2kT}} \mathrm{d}v \tag{5.19}$$

Substituting v by ν we obtain

$$v = \frac{c(\nu - \nu_0)}{\nu_0} \qquad \mathrm{d}v = \frac{c\mathrm{d}\nu}{\nu_0} \tag{5.20}$$

$$\frac{\mathrm{d}N(\nu)}{N} = \frac{c}{\nu_0}\sqrt{\frac{m}{2\pi kT}} e^{-\frac{mc^2(\nu-\nu_0)^2}{2kT\nu_0^2}} \mathrm{d}\nu \tag{5.21}$$

The resulting equation can be identified as a Gauss function with a halfwidth of:

$$\Delta\nu = \nu_0 \sqrt{\frac{8kT\ln 2}{mc^2}} \tag{5.22}$$

5.2.2. Line Profile

The previous sections discussed the different aspects and mechanisms of line broadening. We have seen that depending on the underlying mechanism the resulting line profile can be gaussian or lorentzian.

Generally, if the broadening mechanism is homogeneous, *i.e.* all emitters have the same transition probabilities, the result is a lorentzian-shaped line. These include the natural line width as well as pressure/collisional mechanisms. The individual contributions can

be combined linearly into the total LORENTZ component $L(x,\gamma)$ (see equation 5.26). Its FWHM is 2γ.

$$L(x,\gamma) = \frac{1}{\pi\gamma\left(1+\left(\frac{x}{\gamma}\right)^2\right)} = \frac{1}{\pi\gamma}\left(\frac{\gamma^2}{x^2+\gamma^2}\right) = \frac{\gamma}{\pi\left(x^2+\gamma^2\right)} \tag{5.23}$$

On the other hand, the random motion of the emitters as it does appear in the DOPPLER effect are considered inhomogeneous and cause a gaussian broadening. It is represented by $G(x,\sigma)$ in equation 5.26. The FWHM is given by equation 5.25. It should be noted, that contributions of different GAUSS profiles are added quadratically.

$$G(x,\sigma) = \frac{1}{\sigma\sqrt{2\pi}} e^{-\frac{x^2}{2\sigma^2}} \tag{5.24}$$

$$\mathrm{FWHM}_{Gauss} = 2\sqrt{2\ln(2)}\sigma \tag{5.25}$$

In reality the line's actual form is composed of the individual portions of all the mentioned broadening phenomena. It is therefore a combination of a GAUSS and a LORENTZ profile and can be expressed by a folding integral of the two functions $L(x,\gamma)$ and $G(x,\sigma)$ (equation 5.26, note that for $L(x,\gamma)$ x has been replaced by x'). The resulting function is called VOIGT profile. No analytical solution exist for this integral. In pre-computer times tabulations of the VOIGT shape were used for different gaussian-to-lorentzian ratios (for example [84, 85]). With modern computers it is possible to solve the folding integral (equation 5.26) numerically by utilizing the FADDEEVA function (see octave scripts in appendix: A.2 and A.3). The GAUSS component dominates the center of the peak while the lorentzian influence is notable more as a broadening at the wings of the spectral line.

$$\Psi(x,\gamma,\sigma) = \int_{-\infty}^{\infty} L(x',\gamma)G(x-x',\sigma)dx' \tag{5.26}$$

Figure 5.2 illustrates the convolution of the lorentzian and gaussian profiles. At every point of the GAUSS function (black) a LORENTZ function is placed and scaled by the gaussian value (green). Summation over all functions result in the VOIGT profile (blue). We can notice the broadening in the wings compared to the original GAUSS profile.

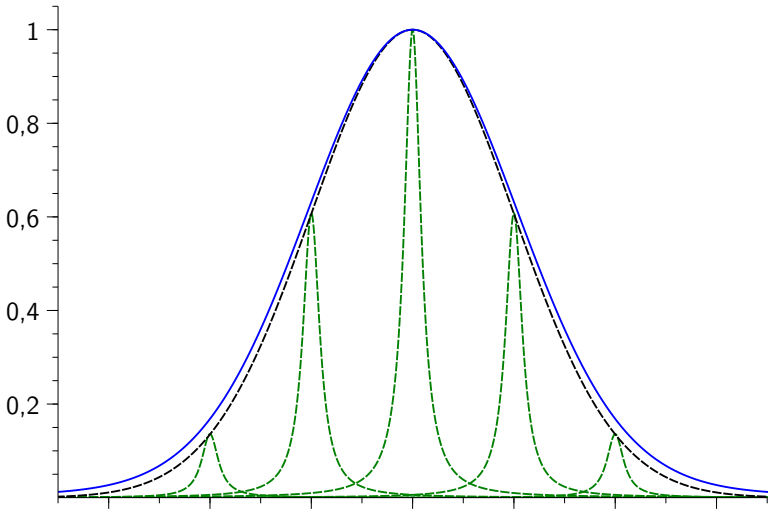

Figure 5.2.: VOIGT line profile. The green curves represent the lorentzian profiles which are scaled by the value of the gaussian function (black) and summed up for every position into the VOIGT profile (shown in blue).

In addition to the aforementioned broadening mechanisms and their resulting line profiles, there is always the influence of the measuring instrument (*i.e.* the spectrometer) which also contributes to the final appearance of the spectral line. The instrument profile can be of gaussian, voigt, triangular or other shape and has to be convoluted again with the existing profile function.

CHAPTER 6

Inductively-Coupled Plasma Optical Emission Spectrometry (ICP-OES)

In the previous chapter the fundamentals of atomic spectrometry were discussed. Now I want to give a short overview of the ICP-based atomic spectrometry instruments which were used in the different portions of my work. The term ICP stands for "inductively-coupled plasma" which has become one of the most routinely used excitation sources in atomic spectrometry. Principally, a gas (*e.g.* Argon) is initially ionized by an electric discharge. The partially ionized state in the argon gas is then sustained through the energy of an electromagnetic field which is produced by a radiofrequency (RF) generator. The RF field is coupled into the ionized argon through a coil. It causes the negatively charged electrons and the positively charged argon nuclei to move in different directions, thus causing collisions and maintaining the ionization equilibrium. As a result, the plasma core is formed. The described process takes place in a special quartz tube called the "torch" (see figure 6.1). Due to the geometry of the RF coil the plasma core has the shape of a toroid and rotates slightly around the z-axis.

The plasma torch is shown in more detail in figure 6.1. It consists of three concentric quartz tubes. The tubes are connected to their respective gas supplies: the outer (or cooling) gas, the intermediate (or plasma) gas and the (inner) sample aerosol coming from the spray chamber. The outermost glass tube shields the RF coil from the plasma. It also confines the plasma to the space inside the coil as without it the ignition could also take place between the windings of the coil itself. The inlets of the outer gas flow are situated tangentially and

produce a vortex-shaped flow. This helps to keep the quartz tube cool and stabilizes the plasma core.

A typical typical ICP-OES analysis is summarized in figure 6.2. The part in the box was already treated in the "sample preparation" part (refer to part I). After retrieving the sample solution, its way continues through the sample introduction stages of the instrument. The nebulizer creates a aerosol which is suitable to be supplied to the plasma through the innermost injector tube. While flowing through the aerosol channel the droplets are dried, atomized and excited. The so-called "normal analytical zone" names the region where the recombination and emission of light occurs. As we move further away from the plasma core towards the tail, the temperature is decreasing and as a consequence, atomic absorption is observed. In axial view the tail of the plasma has to be cut off in order to be able to detect the atomic emission. This can be done by either a shear gas, which blows off the plasma tail, or by an optical plasma interface. When using radial view of the plasma the aforementioned measures are not necessary. At the end the spectrometer detects and integrates the emitted light.

6.1. Enclosed Plasma Interface

If we consider the gas flows through the torch, typically around $15\,\mathrm{L\,min^{-1}}$ are needed. The largest part is consumed by the outer (cooling) gas stream. All the plasma gases are removed by the ventilation of the plasma chamber. Depending on the type of plasma gas this circumstance contribute a significant amount to the running costs of the inductively-coupled plasma optical emission spectrometer (ICP-OES). Figure 6.3 shows a modification of the optical plasma interface which seals the tip of the torch to the spectrometer interface. This makes it possible to collect the gases and reutilize parts for the outer gas stream of the torch, saving almost 80 % of the argon consumption. The publication which was prepared for this project can be found in chapter 8 and provides more details.

Due to the size constraints of the published article, the experimental procedure for the argon recycling shall be described here in more detail.

Figure 6.4 shows a schematic representation of the argon recycling apparatus. In the initial state valves E and H (figure 6.4) are completely open in order to let the collected plasma gases escape freely without creating too much pressure inside the enclosed plasma interface. Valve N (figure 6.4) is closed to the point that the argon supplied from the instrument's

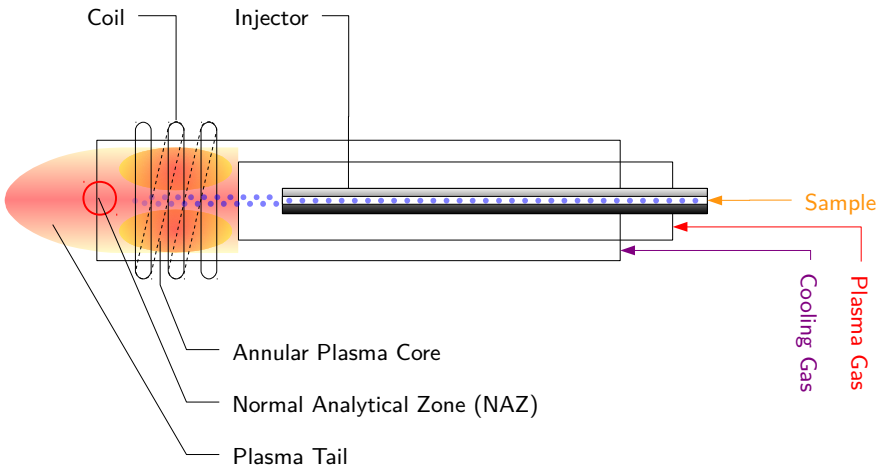

Figure 6.1.: ICP torch schematic. Tangential inlets for plasma and cooling gas are not shown.

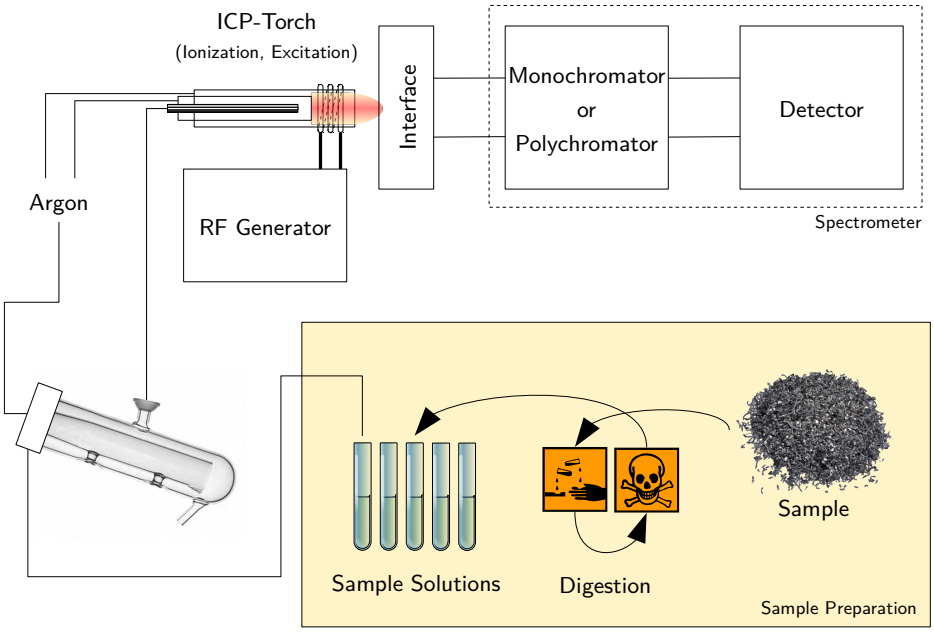

Figure 6.2.: Schematic overview of an ICP-OES analysis.

internal gas box is fed through to the torch. The plasma is then ignited conventionally through the instrument's procedure. All the collected gases are vented through valve E (figure 6.4). With the bypass valve (figure 6.4, G) completely open, the pump (figure 6.4, F) can safely be started without altering the pressure inside the enclosed plasma interface. Now, valve E (figure 6.4) is closed up to the point that the system vents through valve H (figure 6.4). At the same time the bypass valve (figure 6.4, G) is adjusted to achieve the desired low pressure on the enclosed plasma interface side. Now, valve H (figure 6.4) is used to set the necessary pressure for the mass flow controller (around 1.5 bar). Together with valve K (figure 6.4) which mixes in "fresh" argon, the flow through valve H was then fixed to about 1.6 normal liters per minute (calibrated for air) without changing the other pressures. This involved iterating through valves G, H and K in order to achieve the wanted pressures and flow. In this state, the system was ready for switching to argon recycle mode. The transition is done by turning valve M (figure 6.4). The outer gas flow of the torch is then supplied with recycled argon while the argon from the internal gas box of the instrument leaves the system through valve N (figure 6.4) and could now be turned off.

6.2. "Carbon Enhancement Effect"

The second publication (chapter 9) deals with the so-called "carbon enhancement effect" which is haunting ICP-OES users for many years. In the presence of carbon certain elements appear to show higher signal intensity than without. So far, no conclusive explanation has been given for this observation. Recently, Wiltsche *et al.* investigated the behavior of the RF generators of several ICP-OES instruments when the plasma is loaded with different carbon species [3]. It was discovered that the "carbon enhancement effect" is partially caused by an insufficient control of the generator's power output into the plasma. Other influences include changes in the nebulization, the thermal pinch effect and carbon-induced charge transfer reactions. Also, a thermal pinch effect of the plasma was observed where the plasma changes its size.

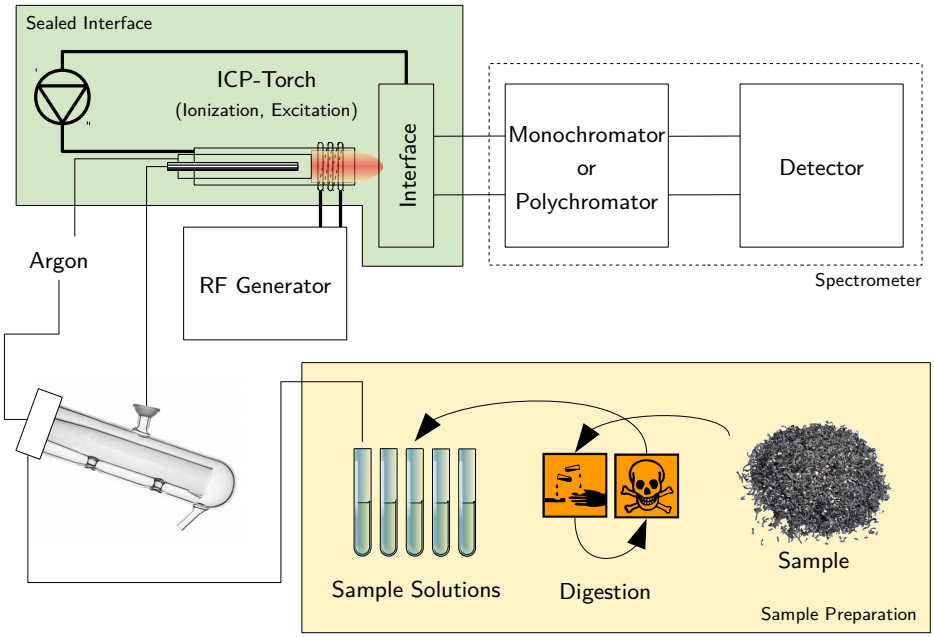

Figure 6.3.: Schematic overview of an ICP-OES analysis with the enclosed plasma interface.

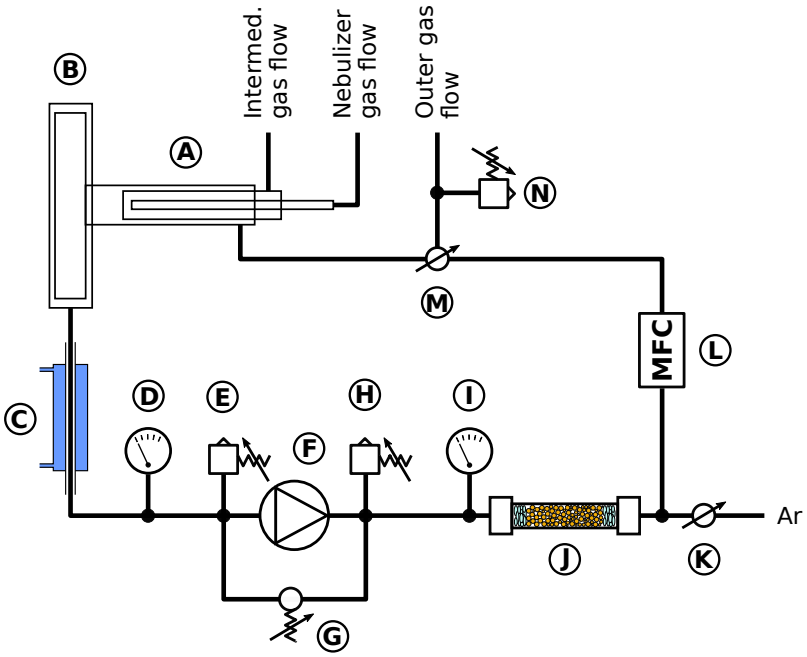

Figure 6.4.: Gas recycling flow schematic. A: ICP torch; B: enclosed plasma interface; C: cooling of exiting gas; D, I: manometers; E, H, N: pressure relief valves; F: membrane pump; G: pump bypass valve; J: gas drying device; K: valve for additional argon makeup gas; L: mass flow controller; M: switching valve.

CHAPTER 7

Plasma Diagnostics

"Photons are clean." (Gary M. Hieftje)

New developments or changes to parts of an ICP-OES typically influence the formation or the characteristics of the plasma. During the investigation these deviations have to be observed and recorded. Therefore, a set of parameters have been established to characterize the plasma. Due to the rather harsh conditions present in a plasma we can imagine that special ways to measure these properties had to be found. These techniques are summed up under the term "plasma diagnostics". In ICP-OES the most convenient approach is obviously to utilize the (already present) spectrometer and extract information from emission intensity measurements.

The following sections give a short overview of the most important plasma parameters and how they can be determined experimentally.

7.1. Temperature

The biggest part of plasma diagnostics deals with the concept of temperature. Generally, the term "temperature" is linked to the movement of particles. In everyday life we refer to the motion of the molecules in the air. We can then define the temperature T as their mean kinetic energy $E_{kin} = \frac{3}{2}kT$. Since a plasma is comprised of a number of different types of particles, which do not necessarily have the same energy distribution, these simple point

of view is not applicable in this case. Therefore we now expand the concept of temperature to a set of different temperatures which can be used to describe the underlying physical processes. Almost all equations contain an exponential term similar to the BOLTZMANN equation, the same we have already encountered as equation 5.4.

A detailed explanation of the different temperatures is out of scope but a short introduction shall be given.

Translational or Kinetic Temperature (T_{kin}) In the section about DOPPLER broadening (section 5.2.1) we have already encountered the MAXWELL distribution which gives us the velocities of particles (equations 5.19 and 5.21). From this function we can extract the kinetic temperature T_{kin} which also describes the temperature of the system in case of a complete thermodynamic equilibrium (CTE). The kinetic temperature can be seen as a measure to describe the efficiency of the atomization process in the plasma.

Excitation Temperature (T_{exc}) The BOLTZMANN equation gives us the fraction of a certain energetic state in a population of bound electrons (equation 5.4). Here, it is a function of the excitation temperature T_{exc}. It should be noted, that the excitation temperature is not necessarily the same for all elements.

Rotational Temperature (T_{rot}) Similar to the excitation temperature T_{exc}, it is possible to calculate the rotational temperature of a plasma using rotational emission lines of diatomic molecules. It is often used interchangeably with T_{kin} because they are of the same magnitude.

Ionization Temperature (T_{ion}) The ionization process of the plasma can be described by the SAHA equation, which provides the ratio of ions and atoms.

$$\frac{n_i n_e}{n_a} = \frac{2Q_i(T)}{Q_a(T)} \left(\frac{2\pi m_e kT}{h^2} \right)^{\frac{3}{2}} e^{-\frac{E_i}{kT}} \tag{7.1}$$

n_a, n_i and n_e are the number densities of atoms, ions and electrons, respectively, $Q_i(T)$ and $Q_a(T)$ their partition functions and m_e is the mass of the electron while E_i is the ionization potential. Again, we can combine it with the relation for the line intensity (equation 5.7) and yield:

$$\frac{n_e(I^+_{kl}A_{pq}\lambda^+_{kl})}{I_{pq}A^+_{kl}\lambda_{pq}} = \frac{2g_k}{g_p}\left(\frac{2\pi m_e kT_{ion}}{h^2}\right)^{\frac{3}{2}} e^{-\frac{E_i+E^+_k-E_p}{kT_{ion}}} \tag{7.2}$$

By evaluating the emission line intensity ratio of the ions to atoms it is possible to determine the ionization temperature T_{ion}. We should keep in mind that T_{ion} is different for each element.

Electron Temperature (T_e) The free electrons in a plasma are not bound to any energy levels. Therefore, the radiative recombination with argon ions can be observed as a continuum in the spectrum. It is governed by its electron temperature T_e.

Radiation Temperature (T_{rad}) If the system is in thermal equilibrium the radiation density can be calculated by PLANCK's formula of radiation. T_{rad} is then equal to the blackbody temperature and, in a CTE, also to the overall temperature T of the system.

7.1.1. Temperature Determination Using Absolute Line Intensities

The temperature T_{exc} can be determined by either directly evaluating the absolute line intensities or by using relative methods. Absolute line intensities require the knowledge of the transition probabilities and number densities of the participating species as well as an accurate calibration of the optical system. The line intensity was already described as equation 5.7. For the actual measurement we can add the observation length l, similar as in LAMBERT-BEER's law.

$$I_i = \frac{l}{4\pi}\frac{hc}{\lambda_i}A_i\frac{N}{Q(T_{exc})}g_i e^{-\frac{E_i}{kT_{exc}}} \tag{7.3}$$

7.1.2. Temperature Determination Using Relative Line Intensities

Because of the reasons mentioned above, methods taking advantage of relative line intensities are more easily applicable. One possibility is the so-called BOLTZMANN plot method. It uses a set of emission line intensities to extract the exponential factor of the underlying

distribution. Firstly, we take the formula for the emission intensity (equation 7.3) and bring all line specific coefficients to the left side, resulting in equation 7.4.

$$\frac{I_i \lambda_i}{g_i A_i} = \frac{lhcN}{4\pi Q(T_{exc})} e^{-\frac{E_i}{kT_{exc}}} \tag{7.4}$$

By taking the logarithm, the function can be linearized. Then we plot the left hand side using our set of emission lines with their parameters against the excitation energy. The slope k of the line equation is then proportional to the excitation temperature T_{exc}.

$$\underbrace{\ln\left(\frac{I_i \lambda_i}{g_i A_i}\right)}_{y} = \underbrace{\ln\left(\frac{lhcN}{4\pi Q(T_{exc})}\right)}_{d} - \underbrace{E_i}_{x} \underbrace{\frac{1}{kT_{exc}}}_{k} \tag{7.5}$$

Depending on the chosen emission lines, the BOLTZMANN plot gives the temperature of the distribution which is governing the respective process in the plasma.

Another simple way of obtaining the temperature is by using a pair of emission line intensities. This works essentially like a BOLTZMANN plot but with only two data points.

It should be kept in mind, that detector sensitivity can differ between wavelengths depending on the construction of the detector. Obviously, line intensities with varying detector sensitivity cannot be compared without further corrections. As a consequence, the easiest solution is to only use wavelengths which are projected onto the same detector array.

7.1.3. Thermodynamic Equilibrium

The terms complete thermodynamic equilibrium (CTE) and local thermodynamic equilibrium (LTE) have been used a number of times in the previous sections. In general, a system is in thermodynamic equilibrium if there is no macroscopic net flow of energy or matter in the system. Another interpretation can be that the time scales of the exchange of energy or matter are much longer than the mean time between collisions. The free electrons in the plasma are primarily responsible for collisions because of their large speed and short mean free path. Therefore, the electron density n_e of a plasma can be used to estimate a thermodynamic equilibrium. Methods for obtaining n_e are covered in section 7.3.

We can speak of a global thermodynamic equilibrium when the intensive parameters such as the temperature of the system are homogeneous throughout the whole system. In contrast, a LTE exposes variation of the parameters in space and time but at a very slow rate so that an equilibrium between neighboring spaces can still be assumed.

If the plasma is in a LTE all temperatures from the different distribution functions except T_{rad} have the same value and it can be described by a single temperature T (see equation 7.6). A CTE extends the concept by also setting T_{rad} equal. This only applies to blackbodies as there is no transfer of radiative energy allowed. A blackbody then is solely described by its temperature $T_{rad} = T$ which is only achieved through the absence of any temperature gradient and – hence – no radiative transport.

$$T = T_e = T_{ion} = T_{exc} = T_{kin} \tag{7.6}$$

Because a luminous plasma radiates energy it is obviously not a blackbody and as a consequence cannot be described only by Planck's radiation law. Temperature gradients between different zones in the plasma cause radiative energy transfer, therefore the assumption of an LTE is not valid. It should be remarked that for its analytical application the ICP is not required to be in LTE.

7.2. Plasma Robustness

Apart from rather elaborate procedures for determining the different plasma temperatures and the plasma's deviation from LTE, a simpler method exists. Mermet [86] suggested the use of magnesium emission lines (Mg (II) 280.270 nm / Mg (I) 285.231 nm) for determining the deviation of the plasma from LTE. This ratio is now called "plasma robustness". It is based on the fact that atomic lines are less sensitive to changes of the plasma operating conditions than ionic lines. Therefore this simple ratio can serve as an indicator for alterations in the atomization and excitation conditions.

7.3. Electron Density

The electron density of a plasma is one of its fundamental properties as it is a measure for the degree of ionization. It is defined as the number of electrons per volume (n_e, electrons m^{-3}). Even though the definition is rather easy (compared to the temperature, refer to section 7.1), the determination is challenging.

It is possible to extract the electron density from the temperature measurements we have seen previously. The ionization temperature T_{ion} can be used by transforming the SAHA equation (equation 7.1). Another possibility is the continuum radiation of the electron recombination although it requires the knowledge of the electron temperature T_e.

When discussing line broadening mechanisms (section 5.2.1) we already encountered the STARK effect. The electrical field of the electrons in the plasma cause the broadening of various emission lines. Therefore, one very convenient method for obtaining the electron density is measuring the width of these spectral lines. The width of the analytes' emission lines in the ICP is dominated by DOPPLER broadening but the lines of the hydrogen BALMER series exhibit a strong sensitivity of their line shape towards electrons and a linear STARK effect. In addition, the wavelengths are readily observable in the available spectrometers which makes them suitable for electron density measurements in ICP-OES.

GIGOSOS *et al.* [87] simulated the emission line profiles for the first three lines of the hydrogen BALMER series using different parameters for ion dynamic effects (masses, temperatures and kinetic equilibrium). By combining the results of the simulation they were able to develop a formula which is only dependent on either the FWHM or FWHA of the experimentally obtained line profile.

Because the instrument used for this work (Spectro Ciros Vision EOP) does not have detector coverage for the most commonly used H_β line, the H_γ line (434.047 nm) was recorded instead. However, it was found difficult to accurately measure the FWHM of the H_γ line because of its unusual shape. In argon plasmas there are also two strong background emission lines overlapping the rather broad hydrogen peak (see figure 7.1).

One solution was to write an Octave[1] script which uses the data from the detector pixels to integrate the H_γ line and also tries to remove the interfering peaks by subtracting a VOIGT profile. The FWHA is then extracted from the cumulative value of the integral

[1] GNU Octave, a high-level language for numerical computations – `http://www.gnu.org/software/octave/`

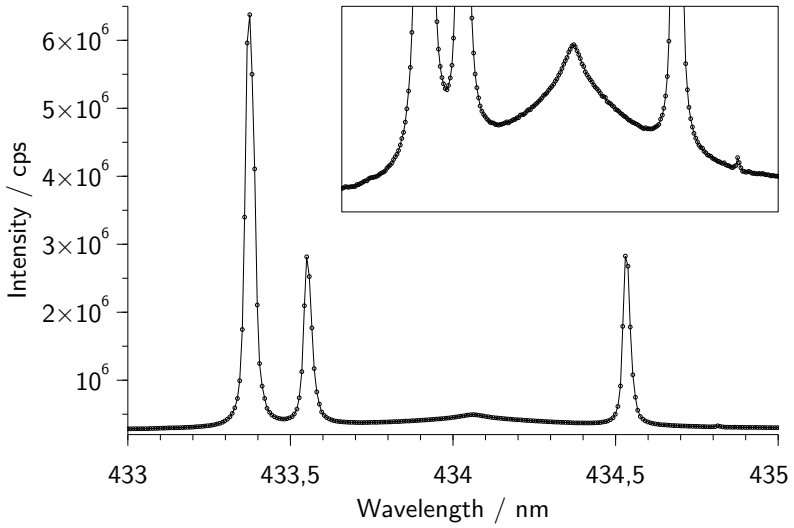

Figure 7.1.: H_γ emission line recorded with the Spectro Ciros Vision EOP instrument while aspirating only wash solution (3 % HNO_3 v/v). The small box shows a zoomed view of the line profile.

by subtracting the value at 1/4 from the one at 3/4 of the area. It is then evaluated using Gigosos' formula. The script can be found in the appendix A.

The electron density of a plasma can also be obtained by a Langmuir probe. It consists of a tungsten wire coated by a ceramic material which is introduced into the plasma. The plasma's characteristic curve can be recorded by applying a voltage and measuring the corresponding current. It has to be kept in mind that the probe itself causes a disturbance of the measurement.

In conclusion, electron density measurements are generally difficult and require a lot of assumptions and additional parameters or equipment. Nevertheless, it was still possible to extract values for comparison during my research using the Octave script.

7.4. Radiofrequency Generator Characteristics

Although not directly related to the plasma, the RF generator can give information about the state and changes in the plasma. Parameters that can be measured directly include the frequency and the voltage and current to the RF generator circuit. The relevant instrumentation and procedures are described by Wiltsche *et al.* [3, 88].

The frequency of the generator can be monitored by a special pickup coil which is mounted inside the plasma compartment of the instrument. A frequency counter then registers the RF field emitted by the load coil.

For the generator's input power measurement, the control input of the high voltage power supply was tapped. The voltage and current feedback of the generator was then recorded using an analog-digital converter (ADC). Appendix B.2 includes the schematics of the ADC circuit.

CHAPTER 8

Enclosed Plasma Interface

Paul Tirk, Matthias Wolfgang and Helmar Wiltsche

The following chapter was submitted to "Analytical Chemistry" under the title "Reduction of argon consumption to $< 2\,\mathrm{L\,min^{-1}}$ by gas recycling in inductively-coupled plasma optical emission spectrometry".

Abstract

An innovative interface between the torch and the entrance optics for inductively-coupled plasma optical emission spectrometry (ICP-OES) is proposed. This system is capable of collecting all argon which was initially supplied to the torch, cooling and cleaning it and feeding most of the argon back to the outer gas port of the torch. Thereby, the total argon consumption could be reduced from 14 to $1.4\,\mathrm{L\,min^{-1}}$ using a standard torch and without restricting the RF power. The excitation- and rotational temperature of the plasma were identical when comparing the traditional setup with the enclosed plasma interface. However, the limits of detection (LODs) and limits of quantification (LOQs) of 27 elements investigated were degraded about 5-fold, though this fact can be expected to stem from a change of the observed zone in the plasma caused by the slight over-pressure of 2000 Pa within the interface. Though the enclosed plasma interface was located close to the load coil, the RF power coupled to the interface was well below 1 W and no RF arcing was observed for two different RF generator designs.

8.1. Introduction

Although the inductively-coupled plasma (ICP) has been used in many analytical applications for over 50 years, its principal mode of operation has not changed significantly. The plasma discharge is located inside a quartz tube and usually expands under atmospheric pressure into the surrounding air. In total, argon gas flow rates of $10-20\,\mathrm{L\,min^{-1}}$ are needed during operation resulting in a significant fraction of the running costs of any ICP-based instrument.

Several approaches for reducing the ICP's argon consumption have been reported: as the outer gas flow is commonly the largest, a lower gas consumption can be attained by decreasing the diameter of the torch [89, 90] or by fostering the torch cooling with an additional flow of air [91, 92] or water [93, 94]. However, both approaches have limitations: decreasing the torch diameter was found to result in RF coupling into the analyte channel which in turn caused greater matrix effects [95]. Cooling the outer wall of the torch with a stream of compressed air was found to be superior compared to water cooling, as in the latter case steam bubbles produced local hot spots and devitrification of the quartz tube [95]. However, a low outer gas flow could only be maintained at reduced RF power. Praphairaksit *et al.* [96] concluded that for a stable and analytically useful plasma in ICP-MS an outer argon gas flow of at least $4\,\mathrm{L\,min^{-1}}$ is necessary at 850 W. However, at 1000 W the outer gas flow had to be increased to $5\,\mathrm{L\,min^{-1}}$ to prevent torch damage. Hasan *et al.* [91] extended this research to ICP-OES and concluded, that at an outer gas flow of $7\,\mathrm{L\,min^{-1}}$ the torch life was not compromised when an additional cooling by $20\,\mathrm{L\,min^{-1}}$ air was used. On the downside, however, the limits of detection of emission lines below 200 nm were degraded by a factor of two [91].

By replacing the helical load coil with a plate induction coil, Morrisroe [97] was able to reduce the outer gas flow to $8\,\mathrm{L\,min^{-1}}$ without changing the torch's geometry. It is interesting to note, that Ripson *et al.* [92] used a plate induction coil for the design of an air cooled torch already in 1982.

Klostermeier *et al.* [98] demonstrated that by using a bulb shaped, pressurized air-cooled torch the total argon consumption can be further reduced to $0.6\,\mathrm{L\,min^{-1}}$ although an ultrasonic nebulizer and a desolvation system [99] had to be utilized for sample introduction.

Even lower argon consumption could only be attained by circulating the argon in a closed loop or maintaining the plasma in a container without any gas flow. Jahl *et al.* [100]

designed a spherical discharge container which allowed them to produce either a static or a low flow inductively-coupled plasma at atmospheric pressure. Despite the longer residence time of the analyte in the discharge region, which improved sensitivity, a complex gas handling equipment and lifetime-limiting devitrification of the discharge tube hampered the system. A further restriction to widespread application was the requirement of a gaseous analyte. A comparable approach was reported by Breer *et al.* [101] who used a cylindrical discharge container fed by a low flow of gases. Although it was possible to introduce liquid samples, the setup was limited to rather short periods of operation due to stability problems with the discharge tube.

The unifying disadvantage of all these approaches is their inability to work at RF power levels in the range of 1500 – 1700 W as often required for the analysis of volatile organic substances. Particularly for the miniaturized torches, only limited argon consumption savings can be claimed.

The aim of this work was to design and build a simple and rugged interface between the ICP torch and the entrance optics of an ICP-OES capable of collecting all argon which was initially fed into the torch – despite the high temperature present. Moreover, the operation of the ICP should not be restricted in terms of RF power level, gas flows or sample introduction by this interface. The low argon consumption was thought to be attained by recycling most of the argon back into the outer gas flow of the torch. To avoid contamination, corrosion and instable plasma conditions, water, acids and salts initially introduced through the aerosol will have to be removed. The intermediate gas flow and the nebulizer gas flow continue to be supplied from an external argon supply.

8.2. Experimental

8.2.1. Enclosed plasma interface

The enclosed plasma interface is a gas-tight enclosure that is mounted onto the entrance optics of the ICP-OES on one side and surrounds the torch on the other side. Hence, all argon initially fed to the torch can be extracted as hot gas from this enclosure through a single pipe.

The presented enclosed plasma interface was designed to fit into the plasma compartment of a commercial ICP-OES (Spectro Ciros Vision EOP, Spectro, Kleve, Germany). It consists

of two parts, both machined from brass. The main part (figure 8.1, section 2) is mounted to the spectrometer entrance optics (Optical Plasma Interface – figure 8.1, section 1) and together with the lid (figure 8.1, section 3) it forms a chamber, that contains the plasma upon leaving the torch. The hot gases are directed through a set of eight inclined channels (figure 8.1, C) to the gas collector ring (figure 8.1, B) from where the gas stream leaves the enclosed plasma interface through a brass pipe (not shown in figure 8.1) towards the argon recycling apparatus.

The plasma chamber's lid, which is thereafter referred to as the "shield" (figure 8.1, section 3) is mounted onto the main part through four holes (figure 8.1, I). The corresponding holes in the main part (figure 8.1, E) are bigger in diameter which enable the adjustment in x and y direction of the torch together with the shield. The screws are fixed at the back with washers and nuts. In order to provide a tight connection between the main part and the shield while still maintaining the possibility of torch adjustment, an inflatable silicon rubber gasket (Flohreus GmbH, Germany – figure 8.1, D) is installed in a groove in the main part. By pressurizing the gasket with water it expands and presses towards the shield thus tightening and sealing the connection between the parts. This arrangement was considered crucial for aligning the spectrometer to the center of the ICP's analyte channel. A fixed connection between the main part and the shield might have been simpler to construct but lacks the ability for instrument tuning after exchanging the torch. In addition, the water in the gasket contributes to the cooling of the gasket itself and the interface.

The shield's inner bore surrounds the tip of the torch providing a gas tight seal between the plasma and the air surrounding the torch. This was deemed important as otherwise the recycled argon gas stream might slowly become contaminated with air bleeding into the interface resulting in degradation and ultimately extinction of the plasma discharge. Considerable effort has been put into the development of this seal, as it has to withstand the hot quartz surface of the torch while still being flexible enough to compensate for the different thermal expansion of quartz and brass. Initially silicate-based high temperature cement was investigated but constant cracking and difficult application led to the development of a copper foil lip seal: the torch seal was made of a 0.2 mm copper foil with a hole for the torch punched in the middle (figure 8.1, G). This opening was about 0.5 mm smaller than the diameter of the torch. Upon inserting the torch into the soft copper foil, the hole expanded slightly, forming a stable, endurable lip seal.

While the main part (figure 8.1, section 2) is cooled through the existing spectrometer interface (figure 8.1, section 1) by thermal conduction, both the shield (figure 8.1, section 3) and the inflatable gasket (figure 8.1, D) are cooled by water.

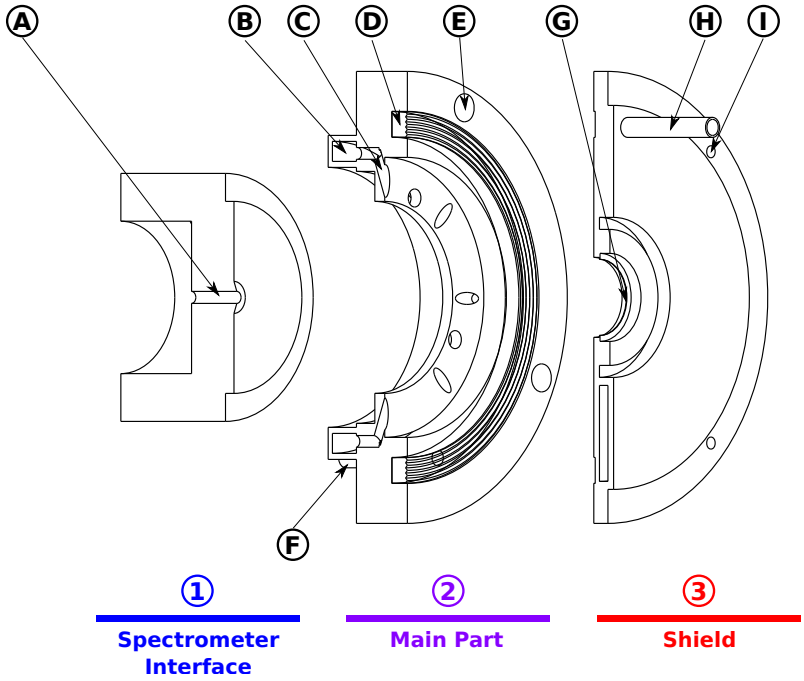

Figure 8.1.: Sectional drawing of the sealed plasma interface parts. A: optical path to the spectrometer; B: gas collector ring; C: inclined gas collector holes; D: inflatable gasket; E: mounting holes for the shield; F: inflatable gasket connector; G: copper torch seal; H: water cooling connector; I: mounting holes of the shield.

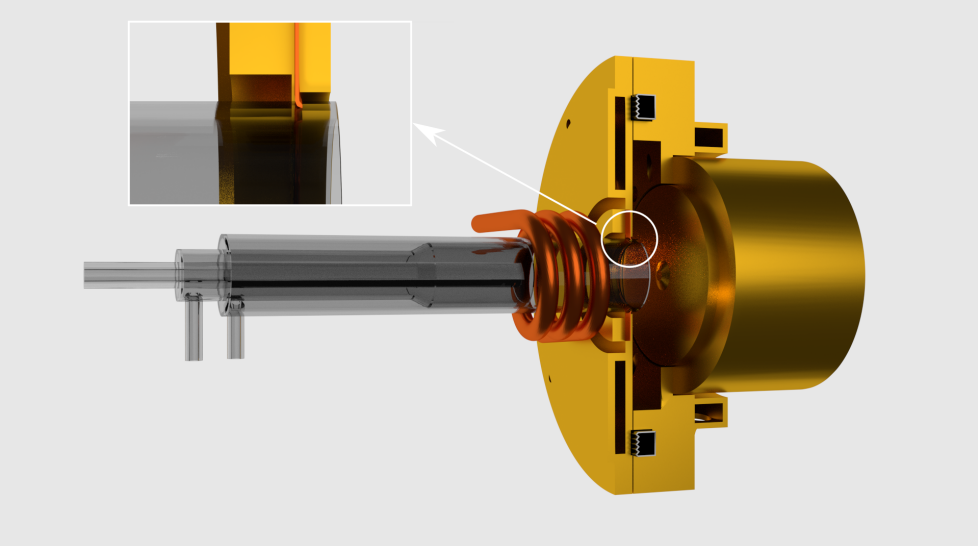

Figure 8.2.: Illustration of the interface.

8.2.2. Argon recycling

Figure 8.3 describes the apparatus for the plasma gas recycling: after being collected in the sealed plasma interface (figure 8.3, B) the argon is fed through a gas cooler (figure 8.3, C). Then the pressure is increased to about 2 bar by a membrane pump (LaboPort N 840, KNF Neuberger GmbH, Germany – figure 8.3, F). This is necessary to allow the mass flow controller (EL-FLOW Base, Bronkhorst, Netherlands – figure 8.3, L) to operate within specifications. In order to protect the mass flow controller from condensation of potentially corrosive substances, a gas drying device (figure 8.3, J; 400 mm × 12.7 mm inner diameter steel pipe filled with 4 Å molecular sieve) was installed after the membrane pump. Manometers (figure 8.3, D and I) and pressure relief valves (figure 8.3, E and H) are used to monitor and set the pressure before and after the membrane pump. The valves also act as safety devices in case of unexpected pressure rise in the system. Because of the fixed pump rate of the membrane pump the bypass valve (figure 8.3, G) is used to adjust the pressure before and after the pump. The mass flow controller (figure 8.3, L) then regulates the flow rate of the argon to the outer gas port of the torch. A combined total argon flow of $14\,\mathrm{L\,min^{-1}}$ is fed to the torch and consequently reaches the gas recycling apparatus. $12.5\,\mathrm{L\,min^{-1}}$ are recycled while the remaining argon vents through valve H in figure 8.3.

A makeup argon flow can be admixed into the recycled stream by an additional valve (figure 8.3, K), though this option was only used during the short transition period between conventional and argon recycling mode.

The presented setup could be operated either without (conventional mode) or with argon recycling. When the ICP is running conventionally the exiting gas leaves the system through pressure relief valve E or H (figure 8.3), depending on the state of the membrane pump (figure 8.3, F) and the bypass valve (figure 8.3, G). In this mode, the argon for the outer gas flow is provided by the internal gas box of the ICP-OES.

8.2.3. Instrumentation

An axially viewed ICP-OES (CIROS Vision EOP, Spectro, Germany) equipped with a cross-flow nebulizer, a Scott-type spray chamber and a standard torch with a 2.5 mm inner diameter injector was used, except for the initial RF stray field experiments. If not stated otherwise the plasma parameters were 1400 W RF power, $12.5\,\mathrm{L\,min^{-1}}$ outer gas flow, $0.60\,\mathrm{L\,min^{-1}}$ intermediate gas flow and $0.83\,\mathrm{L\,min^{-1}}$ nebulizer gas flow. Initial RF

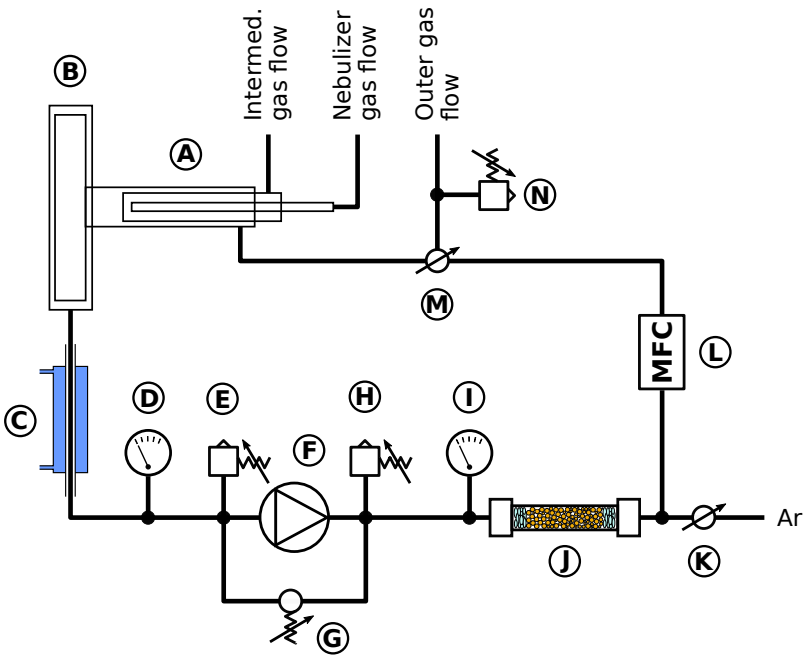

Figure 8.3.: Gas recycling flow schematic. A: ICP torch; B: Enclosed plasma interface; C: Cooling of exiting gas; D, I: Manometers; E, H, N: Pressure relief valves; F: Membrane pump; G: Pump bypass valve; J: Gas drying device; K: Valve for additional argon makeup gas; L: Mass flow controller; M: Switching valve.

stray field experiments were conducted on an axially viewed ICP-OES (Optima 3000 XL, PerkinElmer, USA).

The excitation temperature T_{exc} and the rotational temperature T_{rot} were determined by the Boltzmann plot method. Details on the used emission lines and fundamental constants are reported in a previous publication [88]. The plasma robustness [86] was calculated from the Mg (II) 280.270 nm / Mg (I) 285.213 nm ratio. The electron number densities were obtained from the width of the H_γ emission line (434.047 nm) using the predicted formulas as described by Gigosos *et al.* [87]. Limits of detection (LODs) and limits of quantification (LOQs) were calculated using the calibration method (calibration in the range of $0-1\,\mathrm{mg\,L^{-1}}$; 5 concentration levels; 5 replications; 95 % confidence level).

8.2.4. Reagents

Purified water (18 MΩ cm, Barnstead Nanopure, Thermo Fisher Scientific, USA) and high purity acids (HNO_3, purified by subboiling) were used throughout. The ICP excitation temperature was determined using a $300\,\mathrm{mg\,L^{-1}}$ Fe solution containing 3 % HNO_3 (v/v) prepared from a $10\,\mathrm{g\,L^{-1}}$ Fe single element stock solution (Alfa Aesar, Germany). Standard

solutions for instrument calibration were prepared from a 100 mg L^{-1} multi-element stock solution (Ag, Al, As, B, Ba, Be, Bi, Ca, Cd, Co, Cr, Cu, Fe, K, Li, Mg, Mn, Mo, Na, Ni, Pb, Sb, Se, Sr, Ti, Tl, V, and Zn, Roth, Germany) by dilution with 3 % HNO_3 (v/v).

8.2.5. RF stray field

Due to the fact, that the shield is in close proximity to the load coil, initial experiments were conducted to assess the feasibility of the presented approach. Three processes were considered potentially troublesome: 1) high voltage arcing from the load coil to the grounded shield, 2) inductive coupling of RF stray fields to the metallic shield and 3) capacitive coupling of the RF field to a non-ground referenced shield. Particularly the second process was thought to result in excessive heating of the shield followed by reduced power coupling to the argon plasma torus.

The ICP-OES used for spectrometric characterization (Spectro Ciros Vision EOP) employs a RF generator based on a Huth-Kühn type power oscillator. The load coil of this instrument is grounded on one end making an investigation of high voltage arcing impossible. Therefore, a second ICP-OES was used for the initial experiments whose RF generator is based on a 40 MHz Colpitts power oscillator that creates a high voltage sine of about 3 – 4 kV on the load coil (PerkinElmer Optima 3000XL). Neither side of this RF generators load coil is grounded, but only a "virtual" grounding exists near the center of the load coil.

The RF stray fields in close proximity to the torch were probed with a copper disk (100 mm diameter, 2 mm thick) that could be actuated along the axis of the torch. This disk had a 22 mm hole in the center for the torch to penetrate the disk and a 2 mm slot from the outer rim to the center hole. It essentially resembled a flat, single turn coil. Two wires were connected from the two ends of this "coil" to a high-speed diode-based (MBR16-150 Schottky diodes) full wave rectifier. A RC network with selectable resistors (2.55 Ω to 1 MΩ) and a constant filtering capacitor of 3.3 nF provided further low pass filtering. The copper disk was attached via a sheet of FR4 epoxy (45 mm isolation distance to the grounded chassis) to a lead screw, which was actuated by a stepper motor. Thereby, the slotted copper disk could be moved along the axis of the torch, starting in 2 mm distance to the load coil. For safety reasons, a standard glass bonnet was attached to the torch. A thermocouple was also mounted to the copper disk for temperature measurements. An image of the setup is shown in the supplementary material (section 8.7, figure 8.7). All experiments were conducted at 1300 W RF power. The RF power coupled to the copper disc was calculated from the current induced between the two ends of the slotted copper

disc using the well-known formula $P = I^2R$. It is important to note, that power calculations based on current are more reliable because the voltage measurements are more susceptible to RF noise.

8.3. Results and discussion

8.3.1. RF stray field

In a series of experiments [102], the following facts were established: even in 2 mm distance from the load coil no RF arcing was observed when the quartz bonnet was in place. Moreover, as shown in figure 8.4 the RF stray field coupling to a metallic disc brought into close proximity of the load coil was small: at a distance to the load coil of 2 mm only about 0.3 W were coupled, quickly dropping to 0.06 W at 12 mm and 0.02 W at 27 mm. It may be concluded from these data, that the RF coupling to the copper disc is minimal, even very close to the load coil. This is reflected in the temperature readings of the slotted disk that were recorded for a short circuit condition: the temperature of the copper disc did not increase upon approaching the load coil within the uncertainty of the measurement.

As pointed out in a previous publication [88], the frequency response of a free running RF generator can be used as sensitive indicator for changes in the ICP. Figure 8.5 shows that the frequency of the RF generator did not change significantly if the copper disc was positioned more than 17 mm away from the load coil. From 17 mm to 2 mm the frequency increased by 55 kHz. Though this change is significant, it is small compared to the 900 kHz frequency jump determined for this RF generator during ignition. Moreover, it shows that the RF generator is still capable of compensating for the minor alterations of the RF field around the load coil caused by the copper disc.

It is interesting to note, that no visual disturbance of the plasma was observed during these experiments.

8.3.2. Thermal considerations

As shown in figure 8.2 the plasma interface encloses the space between the spectrometer's optical plasma interface and the tip of the torch, collecting and cooling the argon. The

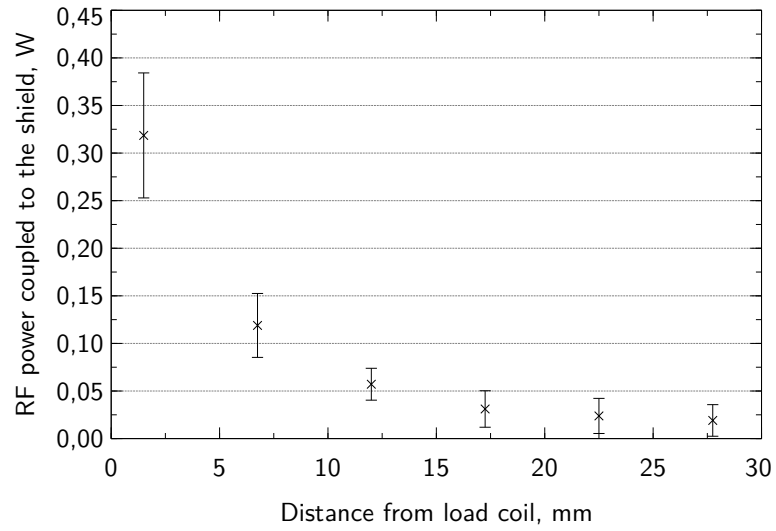

Figure 8.4.: RF power coupled to the slotted copper disk as a function of the distance from the load coil.

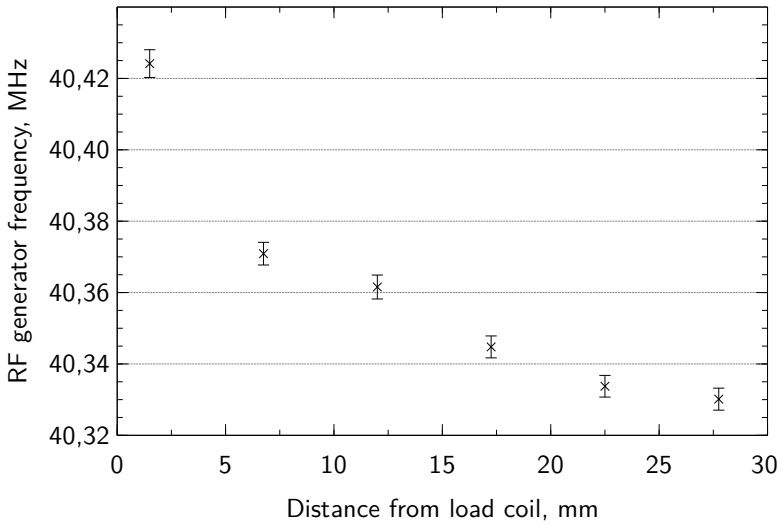

Figure 8.5.: Frequency of the free running RF generator as a function of the distance from the load coil.

boundary region between the outer tube of the quartz torch and the brass shield is subject to extreme thermal and mechanical stress. The temperature measured 10 minutes after plasma ignition on the foremost tip of the torch and in the absence of the shield was $250 \pm 20\,^{\circ}\mathrm{C}$ at a RF power level of 1100 W and increased nearly linear to $540 \pm 20\,^{\circ}\mathrm{C}$ at 1500 W. Contrary to Engelhard *et al.* [103] the temperature was measured by a thermocouple directly attached to the torch and not by infrared thermography. The RF stray field pickup was attenuated by feeding the thermocouple leads several times through EMI suppression ferrite toroids. Though only one spot was monitored by this approach, the temperature could be read directly without cumbersome calibration of a thermographic camera. The torch temperature acquired was comparable between these two approaches: at 1400 W RF power the thermocouple reading was $440 \pm 20\,^{\circ}\mathrm{C}$, while Engelhard *et al.* [103] report a

temperature of 380 to 560 °C for this power level and region on the torch surface (remark: the outer gas flow in this work was 0.5 L min^{-1} higher than the one used by Engelhard).

Clearly, at this temperature polymer seals between the torch and the brass shield are inadequate. Even PTFE failed within seconds. High temperature glass cement was found to fill the gap between the torch and the shield well. However, due to the different thermal expansion between quartz and brass, the cement could not withstand more than 2 or 3 plasma ignitions. In addition, the small plasma compartment of the used ICP-OES instrument made it very difficult to apply the cement evenly around the narrow bore between the torch and the shield. Contrary to this, the copper lip seal described above was stable and tight for more than 6 months, even with regular torch exchanges.

8.3.3. Analytical characterization of the enclosed plasma

The excitation and rotational temperature (T_{exc} and T_{rot}), the electron number density n_e and the plasma robustness (Mg (II) / Mg (I) ratio) were determined with and without the enclosed plasma interface installed. The results listed in table 8.1 show that the excitation and rotational temperature did not change when comparing the traditional ICP-OES setup with the enclosed plasma interface. However, the plasma robustness was lower in the case of the enclosed plasma (4.6 ± 0.2 compared to 6.6 ± 0.1 obtained for the traditional setup). Neither the frequency of the free running RF generator nor the power drawn by the tank circuit changed significantly, though they were shown to be sensitive indicators for changes in the ICP [88]. Consequently, the observed decrease in plasma robustness can be expected to stem from a change of the observed zone in the plasma. This hypothesis is supported by the fact that the pressure of the argon leaving the enclosed interface was found to be about 2000 Pa above ambient pressure. Thereby, the enclosed plasma interface caused a backpressure inside the torch, shifting the zone of maximum analyte emission intensity. Interestingly, this backpressure was not high enough to disrupt the swirl of the outer gas flow which could have resulted in torch destruction. Much contrary to this, the ICP was found to operate very stably even when intentionally increasing the backpressure, by slightly closing valve E (figure 8.3).

LODs and LOQs of 27 elements were determined with and without the enclosed plasma interface installed. With the traditional setup, the obtained LODs and LOQs were about 5 times lower (median of the 27 elements). This finding again indicates a pressure-induced shift in the plasma observation zone when the interface was installed.

Table 8.1.: Characteristics of the enclosed plasma interface and the traditional setup; uncertainty of the temperature determination is dominated by the uncertainty of the linear regression in the Boltzmann plot.

Parameter	Enclosed plasma interface	Traditional setup	
T_{exc}	6500 ± 100	6600 ± 100	K
T_{rot}	4400 ± 100	4600 ± 100	K
n_e	$9 \cdot 10^{21} \pm 1 \cdot 10^{21}$	$5 \cdot 10^{21} \pm 1 \cdot 10^{21}$	electrons m^{-3}
Mg (II) / Mg (I)	4.6 ± 0.2	6.6 ± 0.1	

8.3.4. Argon recycling and contamination

Because of the continuous recycling of the outer gas stream the accumulation of water and decomposition products of acids and samples must be removed, as they would otherwise cause plasma stability problems or severe contamination. Using a pipe filled with molecular sieve, water and potentially some of the particulate matter produced by condensation from the hot plasma during the cooling step can be trapped.

The enclosed plasma was operated for more than 4 h while constantly nebulizing diluted nitric acid (3 % $^{v}/_{v}$) without any detectable degradation of the plasma by N_2 or O_2.

As the reintroduction of particulate matter via the outer gas stream was considered a potential source of contamination, a pathological test setup was selected: a solution containing 50 g L^{-1} NaCl was nebulized for 5 minutes. During the following 30 minutes, diluted nitric acid (3 % $^{v}/_{v}$) was nebulized while recording the signals of Na and Cl.

From figure 8.6 it is apparent that no contamination of the ICP by particulate matter from a previous analysis was encountered for the enclosed plasma interface as the signal decay of the Cl 135.165 nm emission line recorded with the traditional setup closely matches the one obtained while the argon recycling was in operation. Clearly, rinse-out effects in the large surface spray chamber dominated the transient Cl signal. It is interesting to note, that a similar pattern was obtained for Na.

Another source of potential contamination was the brass used for constructing the enclosed plasma interface. Particularly the parts of the interface that were in direct contact with the plasma turned reddish after several hours of operation indicating an evaporation of Zn from the brass. However, neither Zn 213.857 nm nor Zn 206.200 nm showed signals above the background, even after prolonged system operation. A similar finding was encountered with an early test setup installed on the second investigated ICP-OES (Optima 3000, PerkinElmer).

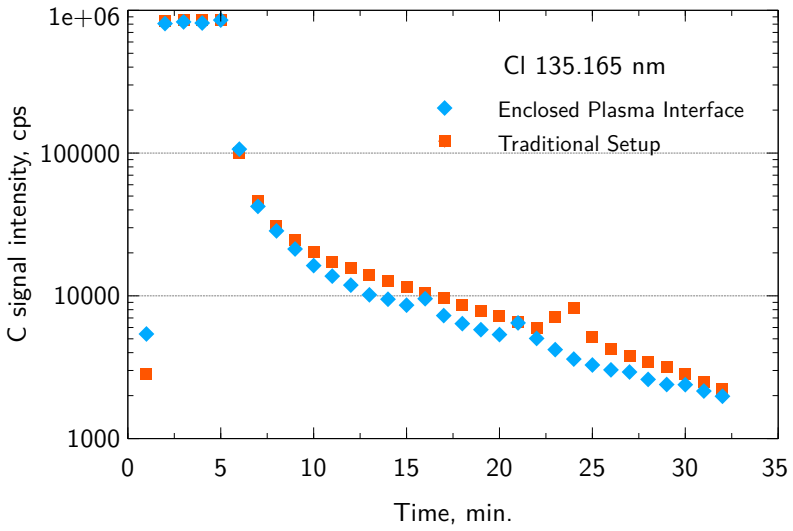

Figure 8.6.: Transient signal of Cl 135.165 nm while nebulizing 50 g L^{-1} NaCl solution for the traditional setup and the enclosed plasma interface with argon recycling. Note the logarithmic scale on the y axis.

8.4. Outlook

By using the enclosed plasma interface, not only the argon consumption of the ICP can be drastically reduced. As the entire space around the end of the torch is filled with argon, diffusion of nitrogen or oxygen into the plasma can be circumvented. As shown by Jin *et al.* [104] this can minimize oxygen- and nitrogen-based polyatomic interferences in ICP-MS when using laser ablation for sample introduction. However, Jin *et al.* flushed the entire surrounding of the torch including the load coil with helium in an attempt to exclude air entrainment. This arrangement neither allows the recycling of argon nor is it applicable to vacuum tube based RF generators as the helium around the load coil would immediately ionize, causing high voltage arcing between the turns of the load coil. It is interesting to note, that this effect is also known to cause destruction to the load coil in case of argon if the plasma compartment is not vented appropriately.

Not only could the enclosed plasma interface attached to an ICP-MS reduce the oxygen- and nitrogen-based polyatomic interferences when laser ablation or gas chromatography is coupled to the instrument, but it would also potentially allow the quantification of these elements by ICP-MS or ICP-OES. Current experiments based on ICP-OES indicate indeed great potential of this approach.

The enclosed plasma interface also allows the calorimetric quantification of RF power delivered to the ICP, as all gas and cooling water streams can be quantified in terms of temperature and mass flow. This is particularly attractive when considering that changes

in the sample composition can result in plasma impedance changes that are followed by RF power level variations [3]. To the best of our knowledge, no other technique than calorimetry is capable of monitoring the RF generator online while altering the sample composition and maintaining an acceptable level of uncertainty.

Another possibility of the enclosed plasma interface is the use of helium instead of argon in the plasma. Though several publications investigated the potential and limitation of this approach [105–108] the costly nature of helium impeded widespread application. However, by adding the possibility to recycle the helium this approach might become attractive again.

8.5. Conclusion

The presented work shows that it is possible to enclose an ICP and recycle most of the used argon. Therefore, the enclosed plasma interface allows to significantly reduce the argon consumption to about $1.4 - 2\,\mathrm{L\,min^{-1}}$ without the need of changing the torch geometry, the sample introduction system or to accept compromise conditions in terms of maximum RF power. Neither the ICP's stability was significantly degraded, nor did the overall excitation condition of the discharge change when using the enclosed plasma interface. Though simple, the cleaning of the argon collected in the interface was effective even for volatile elements like Cl. As this argon was only recycled for the outer gas flow, the initial experiments indicate that no elaborate gas cleaning apparatus is necessary.

The main shortcoming of the current design is the increased pressure inside the enclosed plasma interface resulting in degraded LODs and lower-than-expected plasma robustness. These issues will be corrected in a new interface currently under construction.

8.6. Acknowledgements

Günter Fellner is thanked for skillfully machining the components of the interface. The help of David Puntigam and David Moser is acknowledged.

8.7. Supplementary Material

This section includes the electronic supplementary material of the article. It contains a picture of the RF stray field experiments (figure 8.7).

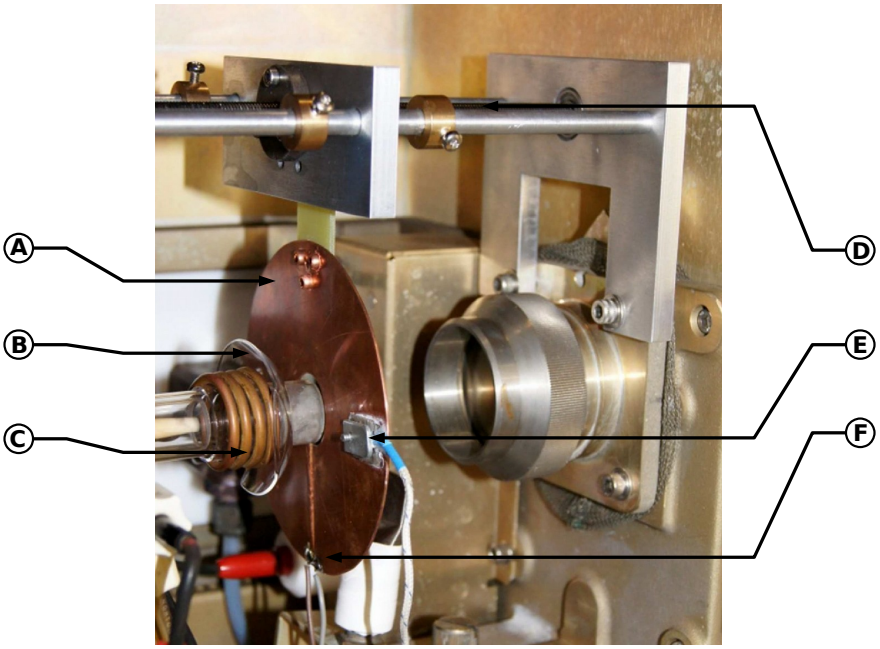

Figure 8.7.: Experimental setup for determining the magnitude of the RF stray field. A: slotted copper disk; B: quartz bonnet; C: load coil; D: actuator for moving the slotted brass disk along the axis of the torch; E: temperature sensor; F: electrical connection to the high speed rectifier.

CHAPTER 9

Carbon Enhancement Effect

Helmar Wiltsche, Monika Winkler and Paul Tirk

The following chapter was published in the "Journal of Analytical Atomic Spectrometry", Volume 30 (2015), pages 2223 – 2234 under the title "Matrix effects of carbon and bromine in inductively coupled plasma optical emission spectrometry" [3].

Abstract

In inductively-coupled plasma (ICP) based techniques the signal enhancing effect of carbon on some elements like arsenic or selenium is well documented. However, there is a large spread in the reported magnitude of this effect and whether it can be observed for other elements too. In this investigation we studied the effect of larger amounts of carbon on a total of 157 emission lines of 36 elements. A strong instrument dependence of the "carbon enhancement effect" was encountered in inductively-coupled plasma optical emission spectrometry (ICP-OES), despite the use of the same sample solutions and the same sample introduction system. Several potential enhancement sources (carbon in the form of methanol, phenylalanine and CO_2 as well as bromine) were compared. By tapping the high voltage power supply of the RF generator, current and voltage fed to the power oscillator could be recorded simultaneously with the emission line signal. From these data it was concluded that the carbon-based matrix effect is a combination of five factors: (1) depending on the source of carbon, changes in the sample nebulization; (2) carbon induced charge exchange reactions; (3) plasma impedance changes caused by the introduction of large quantities of carbon into the ICP: depending on the RF generator used, this effect causes power regulation problems and results in higher RF power coupled to the discharge; (4) thermal pinch effect – the ICP discharge shrinks and becomes smaller; (5) the state of matter (gaseous or liquid) of the introduced carbon sources is relevant to the magnitude of the carbon enhancement effect.

9.1. Introduction

The introduction of larger quantities of carbon into the inductively-coupled plasma (ICP) instrument is reported to increase the sensitivity of elements with the ionization potential (IP) in the range of about 9 to 12 eV [51, 61, 109–120]. This enhancement has been observed in both inductively-coupled plasma optical emission spectrometry (ICP-OES) and inductively-coupled plasma mass spectrometry (ICP-MS). Although this "carbon enhancement effect" was reported nearly 25 years ago [61], the understanding of the underlying mechanism is still unsatisfactory as apparent from the many conflicting results published since then.

By far the largest number of studies describing the "carbon enhancement effect" have been performed using ICP-MS as the speciation analysis of As and Se received great attention and these two elements exhibit in general the largest enhancement by carbon. The differences in the attained level of enhancement are striking: whereas some authors reported a carbon-induced suppression of the As and Se signal in the range of 50 – 70 % (1350 W RF power, 2 % methanol $^{v}/_{v}$) [114], most authors observed a signal enhancement by a factor of 2 – 5 (*e.g.* ref. [73, 111–113, 115, 119, 121]). Even an 11-fold enhancement of the Se-signal has been reported [120]. Indeed, it is difficult to compare these data as different sources of carbon were used. Several authors [73, 119, 121] concluded that the change in nebulization efficiency caused by C-sources such as methanol cannot explain the carbon induced signal enhancement, particularly when considering that the same effect is caused by glycerin [61, 73], glucose [121], ammonium acetate [121] and urea [122]. By using methane as the carbon source Allain *et al.* [61] confirmed that differences in the nebulization efficiency are not the sole reason for the "carbon enhancement effect". Despite the different carbon sources used, most authors [51, 61, 109, 111, 113–115, 119] found that in ICP-MS the As and Se signal initially increases with increasing carbon content of the sample solution, and then reaches a plateau and decreases again. The maximum enhancement of As and Se appears to be a function of the carbon source and of the instrument used.

The reports on the enhancement or suppression of other elements by carbon are even more confusing. Whereas for Au (IP 9.23 eV) [61, 119, 123] and Be (IP 9.32 eV) [51] carbon induced signal enhancement is reported, for Zn (IP 9.39 eV), S (IP 10.36 eV), Hg (IP 10.44 eV) and I (IP 10.45 eV) both carbon induced enhancement [51, 61, 73, 111, 113, 119, 121, 122] and the absence of this effect [61, 73, 118] are reported.

Fewer authors have so far investigated the carbon enhancement effect in ICP-OES. Machát *et al.* [116] found that the small spectral interference on the Se (I) 196.026 nm emission line is caused by CO band emission. The authors noted an instrument dependent enhancement of Se by 20 to 58 % when 10 g L^{-1} C (glycerol; data corrected for nebulization efficiency changes) was introduced into the ICP and that As and Te were enhanced too. Moreover, they found that S, P and Br (from H_2SO_4, H_3PO_4 and HBr, respectively) enhanced the signals of As, Se and Te significantly. Grindlay *et al.* [110] investigated the carbon-related matrix effect and found As and Se enhanced by up to 30 % in the presence of 20 g L^{-1} C from citric acid. Simultaneously low excitation energy atomic lines (EP < 6 eV) were suppressed by up to 15 %, while ionic lines remained unaffected.

A thorough discussion about the potential mechanism behind the "carbon enhancement effect" is given only in few publications. Abou-Shakra *et al.* [124] proposed a charge exchange mechanism between C^+ and selenium atoms. According to this hypothesis, excited Se^+ ($4p^3$ $2D^0$) is formed whose upper level energy of 1098 kJ mol^{-1} is sufficiently close to the IP of carbon (1086 kJ mol^{-1}). Thereby, both the enhancement in ICP-OES and ICP-MS could be explained. Grindlay [73] extended and refined this theory further, as a charge transfer reaction requires not only the minimum energy difference between the involved levels, but obliges the fulfillment of the Wigner spin conservation rule. The authors determined by ICP-MS that the dominant carbon species in the ICP are C^+ and CO^+ and concluded that a high charge transfer probability exists for As, Au, Hg, I, Ir, Os, P, Pt, S, Sb, Se, Te, and Pd. Experimentally Grindlay *et al.* found a carbon induced signal enhancement only for As, Au, Hg, I, Sb, Se, and Te.

As listed above, reports on the carbon enhancement effect presented in the literature rely heavily on ICP-MS data. Particularly for mechanistic studies, the lack of additional information on fundamental plasma parameters such as electron number densities or ionization temperature is unsatisfying. The processes happening in the interface region are another source of potential bias for mechanistic studies: just behind the sample cone a supersonic jet is formed, wherein the broad velocity distribution of atoms from the ICP is turned into a much narrower one, centered around the velocity of Ar [125]. Moreover, this zone is a source of collisions and reactions between the constituents of the expanding gas. It seems not entirely unlikely that, in parts, the large differences in the signal enhancement of As and Se observed for different ICP-MS instruments are caused in this region, as carbon is added in a very high concentration. Another factor that could cause additional bias when studying the carbon enhancement effect is the reported shift of the region of maximum ion density in the ICP [115, 126] that necessitates the readjustment of the sampling depth. Particularly for ICP-MS instruments that alter the sampling depth by

changing the nebulizer gas flow, additional bias from different nebulized sample masses might be introduced.

The situation is different for ICP-OES: once the radiation is emitted from an excited state, the factors that could affect the signal thereafter are minute compared to the expansion of a hot atmospheric pressure plasma into the high vacuum of the mass spectrometer, the associated supersonic expansion and charge separation. Particularly for axially viewed ICP-OESs slight changes in the zone of maximum excitation will not affect the overall signal intensity as much as in ICP-MS, as the observed region inside the normal analytical zone will be averaged by the optical setup.

The aim of this work is to provide insights into the factors that affect the signal enhancement of high IP elements by carbon in the ICP in order to distinguish between spectroscopic and instrumental effects. As apparent by the foregoing discussion, ICP-OES was mainly used for this purpose.

9.2. Experimental

9.2.1. Instrumentation

An axially viewed ICP-OES (CIROS Vision EOP, Spectro, Germany) with a fixed viewing depth was used in this work. The instrument dependence of the investigated effect was also studied using two other ICP-OESs (Optima 3000 XL and Optima 5300 DV; both PerkinElmer, USA) under instrument conditions comparable to those provided in table 9.1 as well as one ICP-MS (Elan DRC+, PerkinElmer, USA). The ICP-OES operating conditions listed in table 9.1 are compromise conditions for multi-element analysis. They were optimized for aqueous (3 % HNO_3 $^{v}/_{v}$) solutions for the highest signal to background ratio for the observed emission lines of As, Ca, Cl, Fe, P, S, Se, and Zn.

A 4-turn probe coil connected to a frequency counter (TF930, TTi Thurlby Thandar Instruments Limited, UK) recorded the frequency response of the free running RF generator. Details of this setup were published previously [88].

Current and voltage delivered to the RF generator were constantly recorded by taping the low voltage control lines between the high voltage power supply (HV-PSU) and the generator control board with analog-digital converters (ADCs). These control lines provide voltages

Table 9.1.: ICP-OES operating conditions (CIROS Vision EOP, Spectro, Germany).

Spectrometer	PASCHEN-RUNGE mount with [127] charge-coupled device (CCD) line-detectors
RF generator	27 MHz, free running HUTH-KÜHN [127] type power oscillator; also known as the tuned plate tuned grid oscillator [128]
Plasma power, W	1350
Outer gas flow, $L\,min^{-1}$	12
Intermediate gas flow, $L\,min^{-1}$	0.6
Nebulizer gas flow, $L\,min^{-1}$	0.83
Sample flow rate, $mL\,min^{-1}$	1.8
ICP torch	Standard torch with 2.5 mm inner diameter injector; fixed (one piece) torch
Nebulizer	Cross-flow
Spray chamber	Scott type
Number of measurements	4
Integration time, s	24

proportional to the output current ($1\,V \equiv 200\,mA$) and output voltage ($1\,V \equiv 1000\,V$) of the HV-PSU. Four 16 bit ADCs (ADS1115, Texas Instrument) controlled by a microcontroller (ATSAM3X8E on an "Arduino Due - open source electronics prototyping platform"[1]) delivered 475 samples/second for each channel to the control PC. The schematic of the ADC board is shown in the ESI[2] of this article (see appendix B.2). As the ADS1115 includes a programmable gain amplifier, no operational amplifier buffer stage was deemed necessary and the connection to the HV-PSU control lines was made directly with a $10\,k\Omega$ resistor. The ADC board fulfilled the noise-, gain- and drift-specifications given in the ADS1115 datasheet. However, due to the lethal voltage present at the HV-PSU output, no attempt was made to check the factory calibration between the high voltage output and the low voltage control lines.

The nebulization efficiency and mass flow of samples introduced into the ICP were determined using the well-established method of continuous weighing [129]. Contrary to the setup employed previously for this purpose [130] two beakers located at the balance were used rather than one: the first beaker contained the sample solution whereas the second was used to collect the liquid returned from the spray chamber. Thereby the density of each solution could be measured independently with a density meter (DMA4500, Anton Paar, Austria).

An external thermal-based mass flow controller (100 sccm, Mass-Flo 1179, MKS Instruments, Germany) controlled the flow of CO_2. The appropriate gas correction factor was used to correct the response of the nitrogen calibrated mass flow controller for the different physical properties of CO_2 as recommended by the manufacturer.

[1] `https://www.arduino.cc`
[2] Electronic supplementary information (ESI) available at DOI:10.1039/c5ja00237k

9.2.2. Reagents

Purified water (18 MΩ cm, Barnstead Nanopure, Thermo Fisher Scientific, USA) and high purity acids (HNO_3, purified by sub-boiling) were used throughout. Standard solutions were prepared from a 100 mg L^{-1} multi-element stock solution (Al, Ag, As, B, Ba, Be, Bi, Ca, Cd, Co, Cr, Cu, Fe, K, Li, Mg, Mn, Mo, Na, Ni, Pb, Sb, Se, Sr, Ti, Tl, V, and Zn, Roth, Germany), several 1 g L^{-1} single element stock solutions (As, Au, B, Bi, Hg, Pb, Se: Merck, Germany; Br, S, P: SCP Science, USA) and in the case of I from KIO_3 (pa, Merck, Germany) by dilution with 3 % HNO_3 (v/v). The ICP excitation temperature was determined using a 300 mg L^{-1} Fe solution containing 3 % HNO_3 (v/v) prepared from a 10 g L^{-1} Fe single element stock solution (Alfa Aesar, Germany). Water saturated with bromine was prepared by equilibration of high purity water with Br_2 (Sigma Aldrich, ACS reagent, Germany) for one week in a dark glass bottle. Methanol (Normapur, VWR, Germany), NaCl (Fluka, Germany), and phenylalanine (f. biochemistry, Merck, Germany) dissolved in 3 % HNO_3 (v/v) were used to study plasma based matrix effects. Argon was of 5.0 quality (Messer, Austria) and carbon dioxide of Biogen C quality (Linde, Austria).

9.2.3. Optical emission-based plasma diagnostics

The magnesium ion to atom ratio (plasma robustness criteria [86]) was calculated from the Mg (II) 280.270 nm / Mg (I) 285.213 nm emission line intensity ratio using a 10 mg L^{-1} Mg solution.

The Boltzmann plot method [131] was used to determine the Fe (I) excitation temperature T_{exc}. Details on the emission lines used and fundamental constants are reported elsewhere [88].

9.2.4. Experimental procedure and processing of the spectra

In order to record a consistent set of data, the effects of gaseous (CO_2) and liquid reagents (Br_2, aqueous solutions (3 % HNO_3 v/v) of NaCl or phenylalanine, or methanol) were investigated using a standardized procedure with five test standards: after recording the blank spectra, standard solutions 1 to 4 were measured. Between the samples, the sample introduction system was rinsed with diluted nitric acid (3 % v/v) for 60 seconds. The elements and their concentrations in each standard solution were: solution 1: 2 mg L^{-1}

of Al, Be, Ca, Cd, Co, Cr, Cu, Fe, K, Li, Mg, Mn, Mo, Na, Ni, Sb, Sr, Ti, Tl, V, Zn, 10 mg L^{-1} of B, Bi, Pb, and 20 mg L^{-1} As and Se; solution 2: 10 mg L^{-1} of Au, Br, Hg, P, S; solution 3: 30 mg L^{-1} I; solution 4: 300 mg L^{-1} Fe.

Gases were added either to the intermediate gas stream of the ICP torch using a small T-piece, or to the spray chamber through a 2 mm inner diameter PTFE tube. For experiments with liquid reagents, the aforementioned four test standards and a blank solution were prepared from the appropriately diluted reagent (methanol, water saturated with Br_2, solutions of NaCl or phenylalanine) and the relevant single or multi-element stock solution.

All analyte signals were normalized to the aqueous standard (3 % HNO_3 $^{v}/_{v}$) using the following procedure: background correction was applied to all spectra. In the first step of the data treatment, the emission signals of the blank solutions for each reagent concentration level were compared with the emission signals of the respective analyte-containing standard. If the signal in the blank solution was larger than 10 % of the uncorrected standard, the line was rejected for further processing, as a spectral interference could not be excluded. Otherwise, if the emission signal passed this criterion, the blank signal was subtracted from the analyte signal and the data were then normalized to the respective aqueous signal (3 % HNO_3 $^{v}/_{v}$).

9.3. Results and discussion

9.3.1. Repeatability of the excitation temperature determination

The interpretation of the results presented in this work relies heavily on the excitation temperature of Fe (I) determined by the Boltzmann plot method. Particularly when comparing data recorded over a period of about one month, the repeatability of the excitation temperature (T_{exc}) is of vital importance. It is important to note that the T_{exc} reported here represents an average temperature of the region in the ICP that is observed by the spectrometer.

The excitation temperature of Fe (I) was determined on four consecutive days. Before recording the emission spectra the RF generator was allowed to "warm up" for 30 min [88]. The excitation temperature was 6470 ± 15 K, 6450 ± 20 K, 6450 ± 10 K, 6460 ± 10 K (mean value ± s; n = 5) using the plasma conditions listed in table 9.1. Then the ICP torch was removed, acid cleaned, reinstalled and the excitation temperature was again recorded

on the following days: $6530 \pm 20\,\mathrm{K}$, $6540 \pm 20\,\mathrm{K}$, $6520 \pm 20\,\mathrm{K}$, $6520 \pm 10\,\mathrm{K}$. After installing the torch again, the observation position of the spectrometer was tuned following the instrument manufacturer's recommendations and similar signal intensities were obtained for the Mn tuning solution. Simultaneously with the observed small change of the excitation temperature, the plasma robustness increased slightly from 6.8 ± 0.1 to 7.0 ± 0.1 when the torch position was slightly altered in the cause of the cleaning process.

The significant difference in the excitation temperature before and after the torch cleaning can be attributed to small changes in the position of the ICP torch within the load coil. Clearly, any investigation on the effect of an external parameter must be recorded without removing or changing the ICP torch, as otherwise an uncontrolled experimental bias is introduced. It is important to note that in the instrument used there is no mechanical indicator for the torch alignment but only the recommendation to introduce the torch into the load coil until the distance between the inner glass tube and the first turn of the load coil is 1 mm. Although for the experiment reported above the exact position of the torch was not determined, a later investigation with a caliper indicated a positioning repeatability of about $\pm 0.2\,\mathrm{mm}$.

It seems also important to note that the precision of the excitation temperature determination was very high: for five independent recordings the standard deviation was always found to be between 10 and 20 K. The uncertainty of the slope of the least square fitted line in the Boltzmann plot was about 100 K. As both the short term (5 repetitions) as well as the long term (4 consecutive days) precision of the excitation temperature determination were much higher, it must be concluded that the uncertainty of the slope in the Boltzmann plot is dominated by the uncertainty of the transition probability data. Consequently, the absolute value of the reported excitation temperatures might be biased, but relative changes can be expected to be identified correctly.

9.3.2. Instrumental dependence of the effect of carbon on the signal of Se

When comparing the degree of enhancement of Se by carbon reported in the literature, the differences in the magnitude of the enhancements are striking, though the various experimental conditions and reagents make a direct comparison difficult. The effect of methanol ($0-10\,\%$ $^{\mathrm{m}}/_{\mathrm{m}}$) on selenium was investigated on three different ICP-OES and one ICP-MS instruments. As the torch geometries of these instruments are different, it

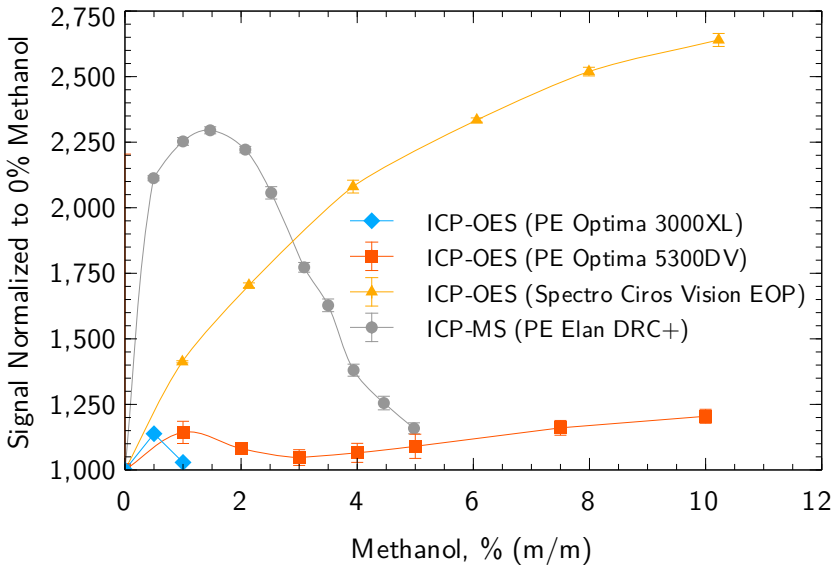

Figure 9.1.: Effect of increasing methanol concentration on the signal of Se in ICP-OES (Se 203.985 nm) and ICP-MS ($^{m}/_{z} = 78$) recorded on different instruments. The Se concentration was 10 mg L^{-1} in ICP-OES and 10 µg L^{-1} in ICP-MS. No internal standard was used; the Einzel-lens of the ICP-MS was tuned for aqueous solutions. Error bars: standard deviation, n = 5.

was not possible to maintain similar outer- and intermediate gas flows. Consequently, these flow rates were selected to match typical conditions used for the analysis of aqueous (diluted HNO_3) samples: both Optima instruments were operated at 15 L min^{-1} outer gas flow and 0.5 L min^{-1} intermediate gas flow; the ICP-MS used 15 L min^{-1} outer gas flow and 1.3 L min^{-1} intermediate gas flow. The RF power, nebulizer gas flow and sample flow rate were kept constant as listed in table 9.1, as well as the nebulizer and spray chamber. Thereby comparable experimental conditions were achieved as evident from the similar plasma robustness (Mg (II) 280.270 nm / Mg (I) 285.213 nm ratio in 3 % HNO_3 $^{v}/_{v}$) that were 7.0 ± 0.1, 6.8 ± 0.1 and 6.5 ± 0.1 for the Spectro CIROS Vision, PerkinElmer Optima 3000 XL and Optima 5300 DV (the data of the two Optima instruments were corrected for differences in the spectrometers' echelle grating efficiency by applying the correction factor 1.85 to the Mg-ratio [132, 133]).

For the ICP-MS experiment, the nebulizer gas flow was optimized for maximum signal intensity in an aqueous solution (3 % HNO_3 $^{v}/_{v}$).

The differences in the instrument dependent effect of carbon are shown in figure 9.1. In ICP-MS the ^{78}Se signal first increased by a factor of up to 2.3 at 1.5 % methanol ($^{m}/_{m}$) and then decreased again. This pattern is consistent with ICP-MS data reported by other authors [51, 109, 115, 121], though the maximum enhancement factor and the corresponding methanol concentration appear to differ from instrument to instrument.

A different behavior was recorded on the three ICP-OES instruments investigated: PerkinElmer Optima 3000XL showed little tolerance to increased methanol load to the plasma and above 1 % methanol (m/m) the ICP extinguished. Interestingly, only a rather small Se signal enhancement of 14 % was recorded on this instrument at 0.5 % methanol (m/m). Using a PerkinElmer Optima 5300DV (axially viewed), the ICP discharge was stable up to a maximum methanol concentration of 10 % (using a 1.8 mm inner diameter injector tube), but the enhancement of selenium was only 20 % at the highest methanol concentration tested.

Using the Spectro Ciros Vision EOP ICP-OES, a steady and large signal enhancement of Se was encountered. At 10 % methanol (m/m) a signal enhancement by a factor of 2.6 was observed for Se (I) 203.985 nm. This enhancement was consistent on all investigated Se emission lines and factors of 2.5 and 2.2 were recorded for Se (I) 196.090 nm and Se (I) 207.479 nm, respectively.

Machát *et al.* [116] also encountered different Se enhancement factors on different ICP-OES instruments, but different sample introduction systems were used.

9.3.3. Effect of methanol

As the Spectro Ciros Vision ICP-OES showed the largest enhancement of Se and allowed the simultaneous acquisition of the entire relevant spectrum, this instrument was used for further investigations. A total of 157 emission lines of 36 elements were investigated. Table 9.2 lists the effect of 10 % methanol (m/m) on selected lines. The data can be classified broadly into four groups.

The first group of emission lines was suppressed by about 10 – 20 % and includes some ion lines of Ba and Sr as well as some atom lines of Mn, Na and Ni. These lines have a very low excitation potential (2 – 3 eV) in common.

The effect of methanol was small on the second group of elements (enhancement by a factor of 0.9 to 1.1). In general, the excitation energies of atom lines in this group were between 3 and 5 eV. For ion lines the total line energy (ionization + excitation energy) was between 9 and 11 eV.

Table 9.2.: Signal enhancement/suppression factors (emission line signal obtained in the given reagent divided by the signal obtained in 3 % HNO_3 v/v) of selected emission lines by various reagents. A complete list of 157 emission lines of 36 elements is available in the ESI (appendix B.1). ND: not determined; Int: spectral interference defined as blank signal > 10 % of the signal in the analyte containing solution before blank subtraction; RSD < 3 % for all emission lines; for an aqueous solution (3 % HNO_3 v/v) the plasma robustness was 7.0 ± 0.1 and the excitation temperature T_{exc} was 6610 ± 20 K.

Emission line, nm	Total line energy, eV	Methanol 10 %	Phenylalanine 8 g L^{-1} C	15 sccm CO_2 added to the aerosol gas stream	15 sccm CO_2 added to the intermediate gas flow	Br_2 34 g L^{-1}	NaCl 30 g L^{-1}
Al (I) 396.152	3.14	1.00	0.98	0.76	1.27	1.06	0.79
Al (II) 167.078	13.41	1.50	1.02	1.04	1.83	0.95	0.69
Ar (I) 404.442	14.69	1.97	0.98	1.36	2.49	0.88	0.90
As (I) 197.262	6.29	1.92	1.08	1.47	1.98	1.03	0.84
As (I) 189.042	6.56	1.97	1.08	1.52	2.08	1.04	0.83
As (I) 193.759	6.40	1.90	1.07	1.48	2.01	1.04	0.84
Au (I) 267.595	4.63	1.09	1.00	0.89	1.17	1.02	0.82
Au (I) 242.795	5.11	1.18	1.00	0.92	1.25	1.03	0.81
B (I) 249.773	4.96	1.16	0.97	0.94	1.26	1.01	0.76
Be (I) 234.861	5.28	1.18	0.99	0.93	1.28	0.96	0.75
Be (II) 313.042	13.28	1.42	1.08	1.07	1.40	1.05	0.66
Br (I) 148.845	8.33	1.57	0.98	0.93	1.59	ND	ND
Br (I) 144.990	8.55	Int	0.98	1.05	1.73	ND	ND
Cd (I) 228.802	5.42	1.31	1.02	0.98	1.44	0.97	0.79
Cd (II) 214.438	14.77	1.57	1.04	1.07	1.85	0.91	0.67
Cl (I) 134.724	9.20	1.77	0.99	1.20	2.03	0.83	Int
Co (II) 230.786	13.75	1.19	1.02	0.85	1.40	0.90	0.65
Cr (II) 205.552	12.80	1.20	1.03	0.86	1.36	0.95	0.67
Hg (I) 253.652	4.89	0.97	0.99	0.84	1.12	0.99	0.83
Hg (I) 184.950	6.70	1.45	1.00	1.16	1.79	0.98	0.85
Hg (II) 194.227	16.82	1.41	1.01	1.05	1.77	0.91	0.77
I (I) 183.038	6.77	1.52	1.04	1.20	1.86	Int	0.76
I (I) 178.276	6.95	1.69	1.05	1.61	2.07	Int	0.83
Mg (I) 285.213	4.35	1.00	0.96	0.73	1.28	0.95	0.79
Mg (II) 280.270	12.07	1.14	1.00	0.84	1.35	0.95	0.61
P (I) 213.618	7.21	2.09	1.03	1.63	2.20	1.14	0.86
P (I) 169.403	8.73	2.08	1.05	1.71	2.21	1.13	0.81
P (I) 138.147	8.97	2.00	1.03	1.65	2.16	1.13	0.88
S (I) 180.731	6.86	1.59	0.97	1.18	Int	1.18	0.94
S (I) 182.034	6.86	1.64	0.98	1.17	1.67	1.19	0.91
Se (I) 207.479	5.97	2.24	1.22	1.65	2.37	1.85	0.71
Se (I) 196.090	6.32	2.51	1.20	1.98	2.89	1.86	0.78
Se (I) 203.985	6.32	2.64	1.22	2.02	2.97	1.83	0.78
Tl (I) 276.787	4.48	1.06	0.95	0.79	1.27	1.04	0.81
Tl (II) 132.171	15.49	2.13	1.03	1.36	2.68	Int	0.72
Zn (I) 213.856	5.80	1.28	1.01	0.94	1.41	0.93	0.77
Zn (II) 202.548	15.51	1.81	1.05	1.23	2.10	0.91	0.69
Plasma robustness		8.2 ± 0.1	7.5 ± 0.1	7.8 ± 0.1	7.2 ± 0.1	7.1 ± 0.1	5.4 ± 0.1
T_{exc}, K		6980 ± 10	6590 ± 10	6800 ± 10	6840 ± 20	6550 ± 20	6510 ± 20

The third group of emission lines was enhanced by about 20 – 50 %. The excitation energy of these lines was in general between 5 and 6 eV and the total line energy of ion lines was between 11 and 14 eV.

Signal enhancements compared to an aqueous solution (3 % HNO_3 $^{v}/_{v}$) of more than 50 % were observed for atom lines with an excitation potential greater than 6 eV and for some high energy ion lines in the region of about 15.5 eV. This fourth group included the atom lines of Ar, As, Br, Cl, I, P, S, and Se as well as some high energy ion lines of Ag, Cd, Tl, and Zn.

It is important to note that the listed energy ranges of the four groups are not sharply defined and that some emission lines do not follow the listed general trend. Moreover, there is no clear correlation between the total line energy (excitation potential for atom lines) and the enhancement, but only a trend.

The power drawn by the RF generator plotted as a function of the methanol concentration nebulized during the measurement is shown in figure 9.2a. The HUTH-KÜHN type power oscillator used is current controlled. For every RF power level that can be selected in the instrument software, a corresponding current is set by the HV power supply. The current is derived from a factory power calibration. The power oscillator behaves purely resistive during normal operation – OHM's law therefore applies and the power drawn by the power oscillator is the product of current (RMS) and voltage (RMS) read directly from the HV power supply.

From figure 9.2a it is evident that with increasing methanol concentration the power drawn by the RF generator increases significantly (about 250 W when changing from diluted nitric acid (3 % HNO_3 $^{v}/_{v}$) to 10 % methanol). As expected from a current controlled power oscillator, the power vacuum tube plate current remained constant, but the plate voltage increased from 3565 V to 4000 V when the sample solution was switched from 3 % HNO_3 ($^{v}/_{v}$) to 10 % methanol ($^{m}/_{m}$). At the same time the frequency of the power oscillator decreased by 26.1 kHz. It seems interesting to note that for aqueous aerosols an increase of the RF generator power is accompanied by a small increase in the frequency. The observed linear decrease of the RF generator frequency (figure 9.2b) and the simultaneous linear increase in the power uptake when the methanol concentration in the sample solution is increased indicates destabilization of the plasma as also observed previously [88]. In addition, this can also be concluded from the rising SDs of the plate voltage that increased the SDs of the generator input power when the methanol concentration rose.

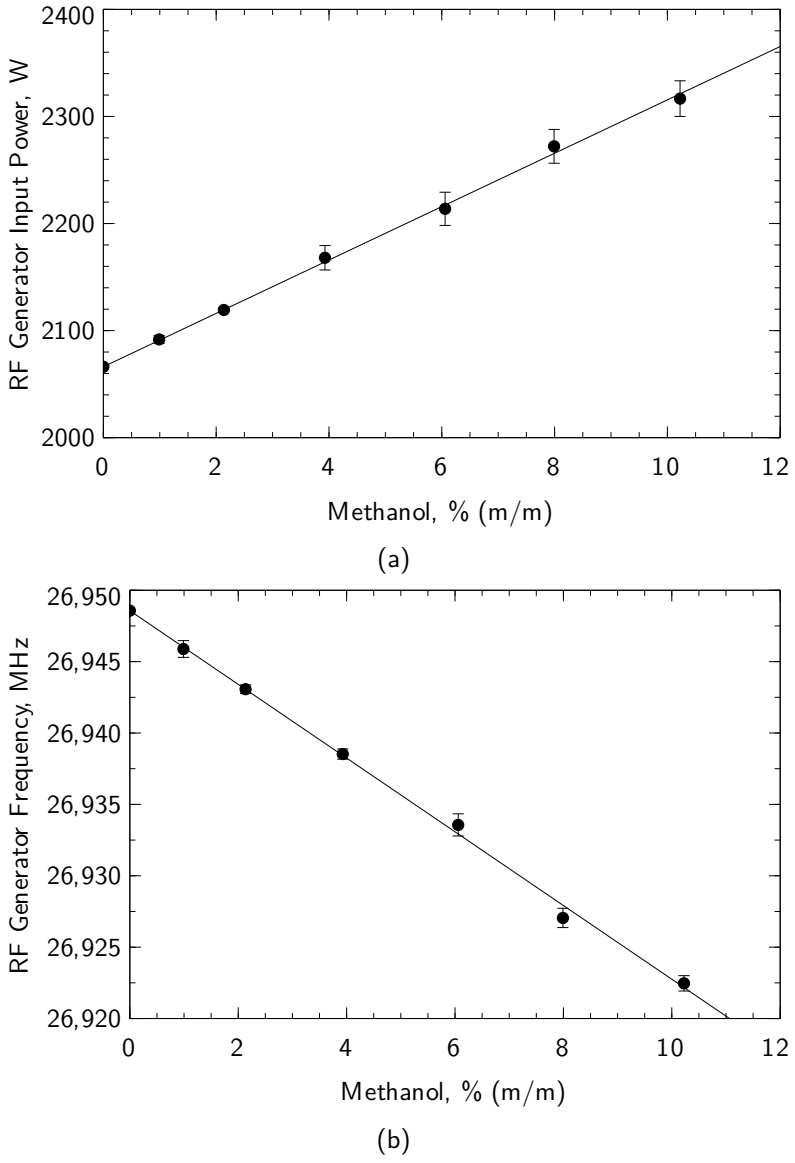

Figure 9.2.: Power drawn by the RF generator for a nominal output of 1350 W (a) and frequency response of the generator (b) as a function of the methanol concentration nebulized during measurement. The error bars represent the standard deviation of five independent experiments.

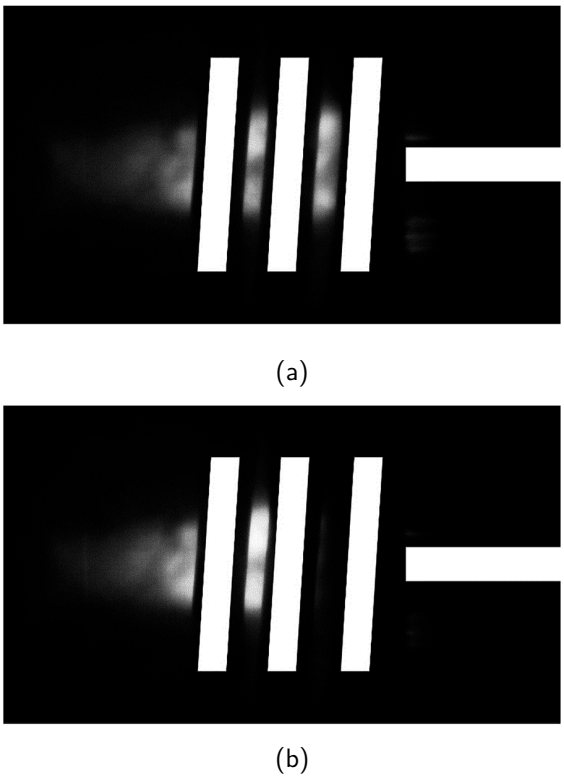

Figure 9.3.: Effect of methanol on plasma volume. (a) Introduction of 3 % HNO_3 $^{v}/_{v}$; (b) introduction of 10 % methanol ($^{m}/_{m}$). The positions of the three turns of the load coil and the injector are represented with white bars for clarity. Both images were recorded under identical photographic conditions (aperture setting, exposure time). Note that in image (b) the plasma withdrew from the space between the first and the second turn of the load coil.

The reason for the observed increase of power drawn by the RF generator can be expected to be a significant impedance change of the plasma caused by the large quantities of carbon introduced. However, only a part of the additionally drawn power will be coupled to the plasma, while the rest is converted to heat in the RF generator.

The reported increase of power uptake of the RF generator has, to the best of our knowledge, not been reported in the literature. However, Larsen and Stürup [113] noted that "the upper practical RF power input was 1320 W" because otherwise the cooling capacity of the ICP-MS interface would have been exceeded. As aqueous solutions could indeed be analyzed at higher RF power levels, this finding could be attributed to a higher power uptake of the RF generator.

When increasing the methanol concentration in the nebulized sample solution, the ICP was found to shrink in size and withdraw from the injector tip. This thermal pinch effect [134] results in a smaller, brighter discharge. From figure 9.3 it is evident that by nebulizing 10 % methanol ($^{m}/_{m}$), the plasma completely withdrew from the injector region and the plasma base was located just after the second turn of the load coil. Yet, the quantification of this effect is difficult, as the load coil hides the most important region of the ICP.

The shifting of the plasma base away from the injector can also be expected to affect the recorded analyte emission intensities: although the plasma was axially viewed and the

viewing depth was not changed, the zone within the ICP imaged onto the entrance slit of the spectrometer will follow the shift of the plasma base to some extent. Simultaneously the plasma power density changed the behavior of the emission lines, which is not easily predictable. Chan and Hieftje [135] showed that the magnitude of matrix effects in the ICP is not constant when changing the observed location within the ICP. However, the large focal length of the spectrometer's entrance optics might reduce this effect when compared to the plasma cross-sections investigated by Chan and Hieftje or radial viewing.

In conclusion, the large quantities of carbon introduced by nebulizing 10 % methanol altered plasma impedance and thereby led to an increase of the power vacuum tube's plate voltage. This in turn increased the RF power delivered to the ICP. Simultaneously, the plasma decreased in size and became hotter as evident from the rise in the excitation temperature from 6610 ± 20 K (3 % HNO_3 $^{v}/_{v}$) to 6980 ± 10 K (10 % methanol). It is apparent that an increase of RF power delivered to the ICP combined with a decrease of the plasma volume is associated with a change in the analyte emission signal intensity.

While all analyte emission lines that were significantly enhanced by carbon showed a steady signal increase with rising methanol concentration, plasma robustness only increased up to 6 % methanol ($^{m}/_{m}$) (peak value 8.8) and then decreased again to 8.2 at 10 % methanol ($^{m}/_{m}$).

One of the inherent problems of using methanol as the source of carbon is the difficulty of quantifying the exact amount of carbon introduced into the ICP. The density of all methanol containing solutions was measured prior to the introduction into the spray chamber and in the waste solution that left the spray chamber after system equilibration.

Moreover, the mass flow of aerosol leaving the spray chamber was determined by the method of continuous weighing. From these data a mass balance was calculated assuming a constant liquid flow rate from the peristaltic pump of $1.82\,\mathrm{mL\,min^{-1}}$: by subtracting the mass flow of methanol in the drained solution from the mass flow of methanol pumped to the spray chamber the mass flow of methanol introduced into the ICP was calculated. Using this method corrects for differences in aerosol formation and preferential evaporation of methanol from the surface of the spray chamber and aerosol droplets. Mora *et al.* [136] found that the D_{50} (droplet distribution diameter below which 50 % of the cumulative aerosol volume is found) of the primary aerosol of a water–methanol mixture decreases with increasing methanol content of the mixture. However, this effect was found to be rather small (D_{50} changed by 3 %) when comparing water with 10 % methanol.

The carbon mass flow introduced into the ICP increased almost linearly with rising methanol concentration in the sample solution fed to the nebulizer. However, below 4 % methanol ($^{m}/_{m}$) the function bends, indicating less pronounced vaporization of methanol in the spray chamber. At the maximum concentration of 10 % methanol ($^{m}/_{m}$), 8.4 mg min^{-1} carbon was introduced into the ICP. The uncertainty of this calculation was found to be dominated by the method of continuous weighing: whereas the removal of the liquid from the sample beaker was constant with time, the draining of the waste solution was discontinuous, as individual droplets formed on the lower end of the SCOTT-type spray chamber's inner tube. Thereby a fluctuating signal was created. The error of the slope was below 6 % for the used recording time of 10 minutes.

It is interesting to note, that without the described correction for the preferential vaporization of methanol in the spray chamber the mass flow of carbon introduced into the ICP would have been underestimated by a factor of 1.7.

9.3.4. Effect of phenylalanine and CO_2

Methanol is a volatile liquid that is introduced into the ICP not only as a liquid contained in the aerosol but also as vapor. Though the total mass flow of methanol transported to the ICP was quantified, we attempted to separate the effects of these two phases on the analyte signal. Firstly, carbon was introduced in the form of a polar, well-soluble but non-volatile substance – phenylalanine was chosen for this purpose. Secondly, a gaseous carbon source (CO_2) was investigated, whereby any nebulization-induced bias could be excluded. CO_2 was added either to the aerosol or to the intermediate gas stream.

As shown in table 9.2 the effects of these three carbon sources on the investigated analytes are quite different: 8 g L^{-1} carbon introduced into the ICP as phenylalanine did not change the signal intensity of most investigated emission lines by more than 5 %. The only exceptions were As, Be (II), and Se with signal enhancements of 10 – 20 %. It is also interesting to note that of all carbon containing reagents investigated only phenylalanine did not alter the emission intensity of the Ar (I) 404.442 nm emission line. Phenylalanine neither changed the excitation temperature significantly nor did it alter the RF generator frequency appreciably (about 1 kHz). The power vacuum tube's plate voltage also remained constant. Combined, these facts suggest that carbon introduced as phenylalanine did not alter the plasma impedance and the enhancement of As, Be (II), and Se is not caused by changes in the ICP itself, as observed when using methanol as the carbon source. It is important to note that the enhancement of As, Be (II), and Se increased with greater

phenylalanine concentration in the solution, reaching its maximum at the highest tested reagent concentration (close to the limit of solubility).

In contrast to phenylalanine, CO_2 as the gaseous carbon source showed a markedly different behavior, as listed in table 9.2. When introduced into the aerosol gas stream, a signal enhancement pattern comparable to that of methanol was recorded, although the signal enhancement factors were between 20 and 40 % lower than when using methanol as the carbon source. The excitation temperature was lower too (6800 ± 10 K *vs.* 6980 ± 10 K). Similar to methanol, a pronounced thermal pinch effect was observed when increasing the flow of CO_2. The plasma impedance was also found to change, as evident from the higher power vacuum tube plate voltage (at 15 sccm a plate voltage of 3993 V was recorded). The frequency of the power oscillator decreased by 28.9 kHz when switching from 0 to 15 sccm CO_2. When CO_2 was introduced into the intermediate gas flow of the ICP, 5 – 20 % higher signal enhancement factors were encountered when compared to methanol, as listed in table 9.2. The excitation temperature was slightly higher and the plasma robustness was lower. Just as with methanol, when CO_2 was introduced into the aerosol gas stream, a strong thermal pinch effect was observed, which again was accompanied by high plate voltage and frequency excursion (3950 V and 27.4 kHz).

In figure 9.5a the carbon emission signal (C (I) 193.091 nm) of the investigated carbon sources is plotted as a function of the carbon mass flow delivered to the ICP. This mass flow was calculated from the determined nebulization efficiency in the case of phenylalanine, or by using the ideal gas law for CO_2. For methanol, the method described above that also includes the preferential vaporization was used. The emission signals did not increase in a linear fashion as the mass flow of carbon was extremely high. For CO_2 the C emission signal was surprisingly similar, despite the different gas flows it was introduced into. Although below 5.5 mg min^{-1} carbon from CO_2, the C emission signal was higher when introducing the gas into the aerosol stream rather than into the intermediate stream, the difference was only about 30 % at 1 mg min^{-1} and 9 % at 2.7 mg min^{-1}. From figure 9.5b it can be deduced that CO_2 introduced into the intermediate gas stream of the ICP acts stronger on the plasma core than when introduced into the aerosol gas stream, as the power vacuum tube's plate voltage rises faster due to the impedance changes of the plasma core. As already noted, higher C-loading of the ICP caused the base of the discharge – the region where the aerosol gas stream enters the plasma – to withdraw from the region between the end of the injector tube and the first turn of the load coil ("normal position") to the space between the first and the second turn of the load coil (thermal pinch effect). The increased distance between the injector tube and the base of the ICP can be expected to allow a higher diffusional exchange between the aerosol and the intermediate gas stream.

Thereby the carbon loading is not restricted to one of these streams, explaining the observed effects.

Another interesting feature shown in figure 9.5 is the effect of low concentrations of methanol on the ICP. Whereas high C loading resulting from methanol causes comparable effects on the plate voltage to similar mass flows of C from CO_2, low concentrations of methanol showed significantly less effect on the plate voltage than in the case of CO_2. This trend was even stronger for phenylalanine, where no effect on the plate voltage was found. These effects could be explained by considering that phenylalanine is introduced only in the form of an aerosol. Carbon is released only after decomposition inside the analyte channel and consequently the diffusion of C into the plasma core can be expected to start much later than in the case of a similar mass flow of CO_2. Thereby, the mass of C reaching the plasma core is much lower and the plate voltage reflects this trend. Following this hypothesis, two processes must be considered in the case of methanol: the vapor phase behaves similarly to gaseous reagents (CO_2) whereas the methanol inside the liquid droplets of the aerosol behaves like phenylalanine. At low methanol concentrations the evaporation of methanol in the spray chamber is not as dominant as at higher concentrations; the lower C emission signal and the smaller change in plate voltage for $1.7\,\mathrm{mg\,min^{-1}}$ C from methanol can be related to this mechanism.

Generally speaking, the enhancement factors of As and Se reported in the literature for non-volatile carbon sources (glucose, citric acid, oxalic acid or glycerol) were always lower than for more volatile reagents such as methanol or even for gases (CH_4), both in ICP-OES [110, 116, 117] and in ICP-MS [51, 61, 109, 112, 113, 115, 119–121].

9.3.5. Effect of bromine

As already noted many attempts to explain the signal enhancing effect of carbon rely on the hypothesis of a charge transfer between C^+ and the high IP element. If carbon with an IP of 11.26 eV is behaving in this manner, Br with an IP of 11.81 eV can be expected to show similar effects.

In contrast to previous reports [116] we wanted to avoid variations in the nebulization efficiency and therefore used water saturated with bromine rather than HBr. Seven concentration levels ($0-34\,\mathrm{g\,L^{-1}}$ Br_2) were prepared from bromine-saturated water. The Br_2 concentration was calculated assuming a solubility of Br_2 in water [137] of $33.56\,\mathrm{g\,L^{-1}}$. All bromine concentrations given below correspond to the mass of bromine dissolved in

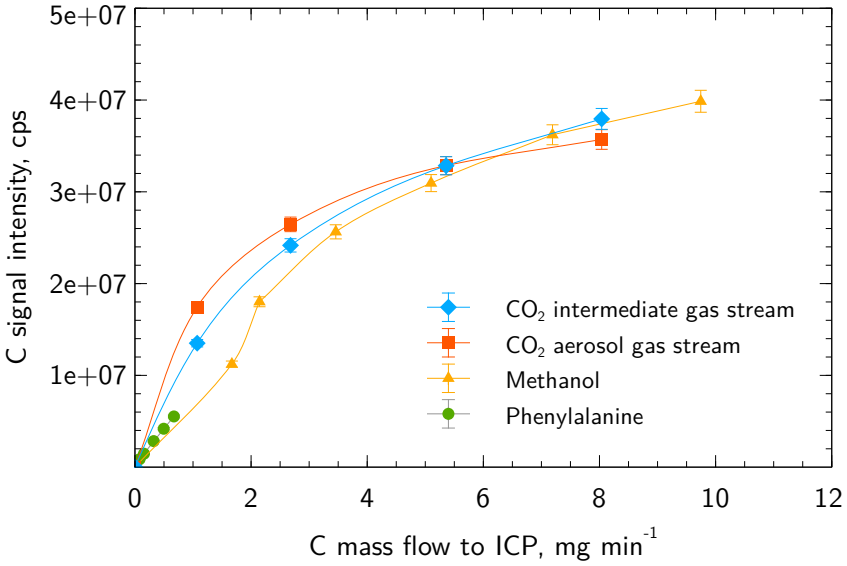

(a)

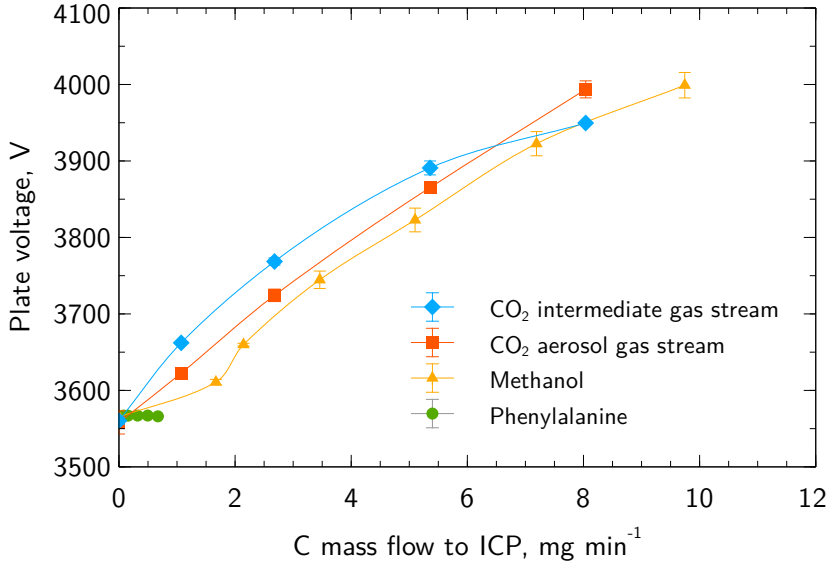

(b)

Figure 9.5.: Signal intensity of the C (I) 193.091 nm emission line and power vacuum plate voltage as a function of the carbon mass flow introduced into the ICP for the investigated carbon sources. The error bars represent the standard deviation of five independent experiments.

water. Due to the toxicity of bromine, we have not attempted to quantify the mass flow of bromine reaching the plasma.

Bromine had little to no effect on most of the investigated emission lines. The signal intensities recorded in a $34\,\mathrm{g\,L^{-1}}$ Br_2 solution differed by less than $\pm\,10\,\%$ from the signal recorded from an aqueous solution ($3\,\%$ HNO_3 $^{v}/_{v}$). The only exceptions were P, S and Se. For P and S the signal intensities initially rose quickly with increasing Br_2 concentration reaching a plateau at about $3.4\,\mathrm{g\,L^{-1}}$ Br_2 with signal intensities of about $13\,\%$ and $20\,\%$ (P and S respectively) higher than in an aqueous standard. For Se the signal increased almost linearly up to $6.7\,\mathrm{g\,L^{-1}}$ Br_2 ($67\,\%$ higher signal than in diluted nitric acid) and then leveled off, reaching about $85\,\%$ signal enhancement at $34\,\mathrm{g\,L^{-1}}$ Br_2. It is most interesting to note that neither As was enhanced by Br_2, nor were Au or Hg.

Plasma robustness and the excitation temperature remained constant when switching from an aqueous solution ($3\,\%$ HNO_3 $^{v}/_{v}$) to $34\,\mathrm{g\,L^{-1}}$ Br_2 and neither the plate voltage nor the power drawn by the RF generator changed significantly. The frequency of the RF generator dropped slightly but significantly by $2.6\,\mathrm{kHz}$.

From these findings it must be concluded that the introduction of bromine did not affect the RF generator and it can be assumed that the power delivered to the ICP remained unchanged. The signal enhancement of P, S and particularly Se cannot be attributed to changes in the nebulization efficiency as other elements would have been affected too. Therefore, the effect of bromine on P, S and Se appears to be a true matrix effect of bromine on these three elements.

If a charge transfer process is the underlying mechanism of the observed effects, two conditions must be met: firstly, the Wigner spin conservation rule [138] must be fulfilled; secondly, the reaction energy defect should be minimal. Grindlay *et al.* [73] assumed that this type of reaction is likely to happen if the involved energy levels differ by between $-1.0\,\mathrm{eV}$ and $+0.5\,\mathrm{eV}$.

From the data listed in table 9.3 we can draw the conclusion that the Wigner spin conservation rule is fulfilled for every examined element. However, the energy difference between the involved levels appears to explain most of the observed effects of bromine: with the exception of Au, I, P, S, and Se the energy difference between the involved levels is too large. Iodine was not investigated, as the Br_2 used was slightly contaminated with this element. For P, S and Se a signal enhancement was observed that could consequently be attributed to a charge transfer reaction. However, for Au no significant signal increase

Table 9.3.: Electronic states and energy defects (ΔE) for the charge transfer reaction between Br^+ and selected elements. Br ionization potential: 11.81 eV; Br ground state ^2P; Br^+ ground state: ^3P; data from ref. [139].

		Energy level of the electronic state closest to the IP of Br			Spin	
Element	Atom ground state term	Term	Energy (eV)	ΔE (eV)	S_i	S_p
As	^4S	^1D	11.04	0.77	5/2, 3/2, 1/2	1/2
Au	^2S	^3D	11.41	0.40	3/2, 1/2	3/2, 1/2
Be	^1S	^2P	13.28	–1.47	1, 0	1, 0
Cd	^1S	^2P	14.47	–2.66	1, 0	1, 0
Cl	^2P	^3P	12.97	–1.16	3/2, 1/2	3/2, 1/2
Hg	^1S	^2S	10.44	1.37	1, 0	1, 0
I	^2P	^1D	12.15	–0.34	3/2, 1/2	1/2
P	^4S	^1D	11.59	0.22	5/2, 3/2, 1/2	1/2
S	^3P	^2D	12.20	–0.39	2, 1	1, 0
Se	^3P	^2D	11.46	0.35	2, 1	1, 0
Zn	^1S	^2S	9.39	2.42	1, 0	1, 0

was encountered when using Br_2, though the energy difference of the involved levels was only slightly larger than in the case of Se. This finding is unexpected, as the Au signal was enhanced in the presence of C.

9.3.6. Effect of NaCl

The presence of high concentrations ($> 1\,g\,L^{-1}$) of easily ionizable elements (EIEs) such as Na is reported to cause plasma related signal variations [140] in the emission line intensities of other elements. Consistent with our previous work [88] we encountered a small, but significant decrease of the RF generator frequency (2.2 kHz) and a severe drop of plasma robustness (from 7.0 to 5.4 when increasing the NaCl concentration in the sample solution from $0\,g\,L^{-1}$ to $30\,g\,L^{-1}$). However, the excitation temperature decreased only to $6510 \pm 20\,K$ over the same interval. Dennaud *et al.* [141] calculated the theoretical plasma robustness as a function of the temperature and found a linear correlation between these two factors, assuming local thermal equilibrium (LTE) in the plasma discharge. When plotting the excitation temperature *vs.* plasma robustness for all reagents reported in table 9.2 bromine and all carbon based reagents follow a general linear trend. However, for NaCl the excitation temperature strongly deviates from this trend. As the measured decrease of the plasma robustness agrees well with data reported in the literature (*e.g.* Brenner *et al.* [142] found that at 1350 W RF power plasma robustness decreased from 9.1 to 7.4 when increasing the NaCl concentration from 0 to $10\,g\,L^{-1}$), the surprisingly high excitation temperature might stem from a stronger deviation of the iron atom level

population from the BOLTZMANN distribution and the associated departure from the LTE. However, the BOLTZMANN plots of the Fe (I) lines were not significantly curved (calculation based on an f-test of the residual standard deviations of the BOLTZMANN plot using either a liner fit or a second order polynomial fit) as reported by KITAGAWA and HORLICK [143].

The investigated emission lines were in general all suppressed by large quantities of NaCl ($30\,\mathrm{g\,L^{-1}}$) as shown in table 9.2. In contrast to the effect of C, the power vacuum tube's plate voltage remained constant up to about $6\,\mathrm{g\,L^{-1}}$ and then dropped almost linearly by 50 V towards the highest investigated NaCl concentration of $30\,\mathrm{g\,L^{-1}}$. Though this drop is significant, the suppression of the analyte emission signals cannot be related to this reduction in RF power, as the drop of 50 V corresponds to a reduction of the RF generator input power of only about 30 W.

9.3.7. Differentiating between the factors contributing to the carbon enhancement effect

From the foregoing discussion it can be concluded that the signal enhancing effect of carbon on several elements is a combination of changes in the excitation equilibrium (*e.g.* caused by a charge transfer reaction) and higher plasma power density. The latter stems from RF generator control issues and the thermal pinch effect.

In an attempt to discriminate between these two effects, solutions containing As, Au, Be, Br, Cl, Hg, P, S, and Se (concentration of each element similar to the previously used standard solutions) in either 3 % HNO_3 (v/v) or 10 % methanol (m/m) together with the respective blank solutions (only diluted nitric acid or 10 % methanol) were measured at constant torch gas flows (as listed in table 9.1) but at different RF power levels (1300 – 1495 W; 50 W increments; setting a higher power level than 1495 W was not possible, as the instrument control software then increased the outer gas flow in an attempt to protect the torch).

As expected, a rising RF power level resulted, in both 3 % HNO_3 (v/v) and methanol, in an increase of the blank signal corrected analyte emission intensity. However, distinct differences were encountered between the investigated emission lines: methanol had little effect on low excitation energy (4 – 5 eV) atom lines (*e.g.* Au (I) 267.595 or Hg (I) 253.652 nm) as the signal intensity was similar to that in 3 % HNO_3 (v/v). This finding is consistent with data presented in table 9.2. For emission lines of higher excitation energy the analyte emission signal in methanol was always higher than in the corresponding aqueous standard for all RF power levels. This effect became more pronounced with increasing total emission

line energy, although only a general trend was encountered but no function was found to sufficiently fit all data points. When plotting the signal intensity for each emission line as a function of the RF power level used, straight lines were obtained ($R^2 > 0.999$). The slope of these lines was always lower in methanol when compared to aqueous solutions. From this finding it can be concluded that the magnitude of the carbon enhancement effect is also dependent on the RF power level used. A similar observation has been reported by Kralj and Veber [121].

To separate the effects of increased plasma power density and changes in the emission line excitation equilibrium on the analyte signal, the RF power *vs.* emission line intensity plots can be used. When assuming that there is no change in the excitation equilibrium by methanol (*e.g.* by a charge transfer reaction), any change in the emission signal caused by methanol would be dependent on the power density in the ICP discharge. Consequently, "apparent" RF power levels can be calculated from the RF power *vs.* emission line intensity plots of aqueous standards (3 % HNO_3 v/v) and the corresponding analyte signal in 10 % methanol at a fixed RF power level (*e.g.* 1350 W). These "apparent" RF power levels describe the hypothetical RF power necessary for obtaining the same emission signal for an aqueous (3 % HNO_3 v/v) solution as in 10 % methanol if the change in plasma power density was the only effect of methanol on the ICP. In table 9.4 these "apparent" RF power levels are listed for 1350 W. There is no clear correlation between these "apparent" RF power levels and the total energy of the emission line.

The tapping of the RF generator's HV power supply revealed, as reported above, that in the presence of 10 % methanol the power drawn by the RF generator increased by about 250 W. The efficiency of the RF generator (power delivered to the ICP as set in the instrument control software divided by the generator input power) was about 60 %. Thereby it can be estimated that the power level in the ICP discharge in the presence of methanol was roughly $1350\,\mathrm{W} + 250\,\mathrm{W} \times 0.6 = 1500\,\mathrm{W}$. Simultaneously, the thermal pinch effect decreased the volume of the plasma. Using the method of Greenfield and McGeachin [144] the decrease of the plasma volume estimated from figure 9.3 was 20 – 30 %. This value represents only a rough estimate, as the boundaries of the ICP are not sharply defined and the plasma can only be approximated as a geometrical combination of a cylinder and a cone. It appears questionable that these two mechanisms for increasing the power density of the ICP are simply additive. Moreover, it is not clear whether the impedance changes of the ICP are a consequence of the plasma's constriction or a change in the total gas composition, or a combination of both effects. In conclusion, too many uncertainties and unknowns are present to even estimate the true power level in the ICP discharge when loaded with methanol and only calorimetric means appear to be a viable method for providing reliable

Table 9.4.: Calculated, hypothetical RF power levels to obtain the same emission signal intensity in an aqueous solution (3 % HNO_3 v/v) as in 10 % methanol (m/m) at 1350 W if the RF power level is the only factor that alters the signal intensity.

Element and emission line, nm	Total line energy, eV	"Apparent" RF power, W
Ar (I) 404.442	14.69	1540
Ar (I) 430.010	14.51	1540
As (I) 189.042	6.56	1660
As (I) 193.759	6.40	1640
As (I) 197.262	6.29	1660
Au (I) 201.200	7.30	1480
Au (I) 242.795	5.11	1430
Au (I) 267.595	4.63	1400
Be (I) 234.861	5.28	1410
Be (II) 313.042	13.28	1480
Be (II) 313.107	13.28	1470
Br (I) 144.990	8.55	1540
Cl (I) 134.724	9.20	1540
Cl (I) 135.165	9.28	1720
Cl (I) 136.345	9.20	1540
Hg (I) 184.950	6.70	1480
Hg (II) 194.227	16.82	1480
Hg (I) 253.652	4.89	1320
Hg (I) 435.835	7.73	1440
P (I) 138.147	8.97	1620
P (I) 169.403	8.73	1630
P (I) 177.495	6.99	1640
P (I) 178.287	6.95	1620
P (I) 213.618	7.21	1650
P (I) 214.914	7.18	1660
S (I) 142.503	8.70	1530
S (I) 180.731	6.86	1560
S (I) 182.034	6.86	1590
Se (I) 196.090	6.32	1830
Se (I) 203.985	6.32	1900

data. However, the power fed to the ICP can be approximated using voltage and current drawn from the HV power supply: at 1350 W the set current is 0.58 A. As previously described, the current remains constant but the voltage fed to the RF generator increases with increasing carbon load of the ICP. Consequently, at the maximum rating of the HV power supply of 4200 V the generator can draw 4200 V × 0.58 A = 2436 W power. Using again an efficiency of 60 % results in about 1460 W that the RF generator can drive into the load – the ICP – under worst-case conditions.

Using this 1460 W, the "apparent" power levels listed in table 9.4 might allow us to distinguish between plasma power density related signal enhancement and changes of the excitation equilibrium: if the "apparent" power level of an emission line is much higher than 1460 W, a secondary process must be involved. When assuming that a difference of 200 W is significant, the following emission lines can be expected to be enhanced by other processes

rather than increased RF power: As (I) 189.042 nm, As (I) 193.759 nm, As (I) 197.262 nm, Cl (I) 135.165 nm, P (I) 138.147 nm, P (I) 169.403 nm, P (I) 177.495 nm, P (I) 178.287 nm, P (I) 213.618 nm, P (I) 214.914 nm, Se (I) 196.090 nm and Se (I) 203.985 nm. The excitation energy of these atom lines is between 6.3 and 9.3 eV. It is interesting to note that all investigated emission lines of As, P and Se follow this trend but only one chlorine line (135.165 nm) follows this trend.

On the other hand, the enhancement of emission lines with an "apparent" power level of ≤ 1460 W can be explained solely on the basis of the increased RF power coupled into the ICP. This group involves Au (I) 242.795 nm, Au (I) 267.595 nm, Be (I) 234.861 nm, Hg (I) 253.652 nm, Hg (I) 435.835 nm and potentially also Au (I) 201.200 nm, Be (II) 313.042 nm, Be (II) 313.107 nm, Hg (I) 184.950 nm and Hg (II) 194.227 nm (the "apparent" power of these lines is only 20 W above the calculated one). The energy sum of these lines spans from 4.6 to 16.8 eV.

For the remaining emission lines (Ar (I) 404.442 nm, Ar (I) 430.010 nm, Br (I) 144.990 nm, Cl (I) 134.724 nm, Cl (I) 136.345 nm, S (I) 142.503 nm, S (I) 180.731 nm and S (I) 182.034 nm) listed in table 9.4 no clear trend can be defined.

9.4. Conclusion

Carbon-based matrix effects in ICP-OES and ICP-MS arise not only from a single cause but appear to be a combination of several factors: (1) depending on the source of carbon used, changes of the sample transport efficiency in the nebulizer and spray chamber due to variations in viscosity, surface tension or density; (2) matrix-induced excitation of certain energy levels by mechanisms such as the charge transfer reaction; (3) thermal pinch effect that results in a constriction of the ICP and consequently a higher power density of the remaining discharge; (4) RF generator related effects due to changes in plasma impedance. Effects 3 and 4 can be expected to be different for every type of RF generator as the impedance changes will act differently on each specific circuit arrangement (free-running generators or crystal stabilized ones with an additional impedance matching network). Particularly the power control algorithm that regulates current and voltage fed to the power electronics can be expected to have a great influence on the stability of the RF generator when loading the ICP with large amounts of carbon. Even the dimensions of the torch or the operating frequency might cause differences in the effect of carbon. As already reported, slight changes of the torch position were found to alter the excitation temperature. The

frequency on the other hand determines the skin depth of the RF current in the ICP and is often associated with either a three or a four turn load coil (27 or 40 MHz respectively). In conclusion, the response of the RF generator to plasma impedance changes appears to be the dominant reason for the large spread of the enhancement factors reported in the literature.

Another factor that should be considered in this context is the fact that not the concentration of carbon in the sample solution determines the degree of matrix effect, but the mass flow of carbon that reaches the ICP and its state of matter. Gaseous reagents affect the plasma core more readily than non-volatile liquid ones.

Based on the findings presented here, the charge transfer reaction combined with the higher power density in the ICP discharge appears to explain most of the element enhancements by C or Br. However, the mechanism fails to explain that in the presence of sufficient carbon elements that cannot be expected to be enhanced by a charge transfer reaction (very high reaction energy defect) also were strongly enhanced (*e.g.* some emission lines of Cl). We can only but agree with Grindlay *et al.* [73] that "additional studies are required to explain these anomalies".

Conclusion

We have seen in the previous chapters that despite its long time of existence, there is still plenty of room for improvements in ICP-OES. These include both the understanding of the operating principles as well as optimizing the running costs and consumption of resources.

The same applies to the field of sample preparation. Although the principles have not changed, the methods and techniques can still be applied to different analytical questions. Furthermore, the need for more efficient and "greener" digestion procedures is still growing in the future.

In conclusion, every small development offers a huge variety of possibilities for further investigation which helps to improve the performance and usability of the ICP-OES in analytical questions.

All in all, I hope that the efforts made will be of some use to others and can serve as the starting point for even more advances both in sample preparation as well as in instrumentation for ICP-OES.

Appendices

List of Figures

List of Tables

Bibliography

[1] H. Wiltsche et al. „A novel approach to high pressure flow digestion“. *Journal of Analytical Atomic Spectrometry* 29, 2 (2014), pp. 272–279. DOI: 10.1039/c3ja50290b (cit. on pp. 1, 19).

[2] Sandra M. Cruz et al. „Feasibility of sulfur determination in diesel oil by inductively coupled plasma optical emission spectrometry after microwave-induced combustion using flame retardant“. *Fuel* 160 (July 2015), pp. 108–113. DOI: 10.1016/j.fuel.2015.07.069 (cit. on pp. 1, 35).

[3] Helmar Wiltsche, Monika Winkler, and Paul Tirk. „Matrix effects of carbon and bromine in inductively coupled plasma optical emission spectrometry“. *Journal of Analytical Atomic Spectrometry* 30 (2015), pp. 2223–2234. DOI: 10.1039/c5ja00237k (cit. on pp. 1, 64, 73, 88, 91).

[4] E. M. M. Flores. *Microwave-assisted sample preparation for trace element determination*. 1st. Amsterdam: Elsevier, 2014, p. 400 (cit. on pp. 9, 17, 36, 44).

[5] M. Würfels and E. Jackwerth. „Untersuchungen zur Kohlenstoffbilanz beim Aufschluß biologischer Probenmaterialien mit Salpetersäure“. *Fresenius Zeitschrift für Analytische Chemie* 322 (1985), pp. 354–358 (cit. on p. 15).

[6] M. Würfels. „Decomposition of Biological Samples with Acids for the Determination of Trace Elements“. *LABO* 3 (1989), pp. 7–15 (cit. on p. 15).

[7] Christiane Gräber and Harald Berndt. „Development of a new high temperature/high pressure flow system for the continuous digestion of biological samples“. *Journal of Analytical Atomic Spectrometry* 14, 4 (1999), pp. 683–691 (cit. on pp. 15, 21, 34).

[8] Thiago Linhares Marques et al. „High pressure microwave-assisted flow digestion system using a large volume reactor-feasibility for further analysis by inductively coupled plasma-based techniques“. *Journal of Analytical Atomic Spectrometry* 30, 9 (2015), pp. 1898–1905. DOI: 10.1039/c5ja00194c (cit. on p. 15).

[9] Erico Marlon Moraes Flores et al. „Microwave-Assisted Sample Combustion: A Technique for Sample Preparation in Trace Element Determination“. *Analytical Chemistry* 76, 13 (2004), pp. 3525–3529 (cit. on pp. 17, 37).

[10] M. Burguera et al. „In vivo sample uptake and on-line measurements of cobalt in whole blood by microwave-assisted mineralization and flow injection electrothermal atomic absorption spectrometry“. *Journal of Analytical Atomic Spectrometry* 10 (5 1995), pp. 343–347. DOI: 10.1039/JA9951000343 (cit. on pp. 20, 34).

[11] Stephen J. Haswell and David Barclay. „On-line microwave digestion of slurry samples with direct flame atomic absorption spectrometric elemental detection“. *Analyst* 117, 2 (1992), pp. 117–120 (cit. on pp. 20, 21, 34).

[12] Ralph E. Sturgeon et al. „Continuous-flow microwave-assisted digestion of environmental samples using atomic spectrometric detection“. *Journal of Analytical Atomic Spectrometry* 10, 11 (1995), pp. 981–986 (cit. on p. 20).

[13] Thomas J. Gluodenis and Julian F. Tyson. „Flow injection systems for directly coupling on-line digestions with analytical atomic spectrometry. Part 2. Reactions in a microwave field“. *Journal of Analytical Atomic Spectrometry* 8, 5 (1993), pp. 697–704 (cit. on pp. 20, 34).

[14] Guy Légère and Eric D. Salin. „Capsule-Based Microwave Digestion“. *Applied Spectroscopy* 49, 4 (1995), 14A–22A (cit. on pp. 20, 34).

[15] Thomas J. Gluodenis and Julian F. Tyson. „Flow injection systems for directly coupling on-line digestions with analytical atomic spectrometry. Part 1. Dissolution of cocoa under stopped-flow, high-pressure conditions“. *Journal of Analytical Atomic Spectrometry* 7, 2 (1992), pp. 301–306 (cit. on p. 20).

[16] Ulrike Pichler et al. „Microwave-Enhanced Flow System for High-Temperature Digestion of Resistant Organic Materials“. *Analytical Chemistry* 71 (1999), pp. 4050–4055 (cit. on pp. 20–23, 27–29).

[17] J. L. Burguera and M. Burguera. „Determination of lead in biological materials by microwave-assisted mineralization and flow injection electrothermal atomic absorption spectrometry“. *Journal of Analytical Atomic Spectrometry* 8, 2 (1993), pp. 235–241 (cit. on pp. 20, 34).

[18] J. L. Burguera et al. „Determination of iron and zinc in adipose tissue by on-line microwave-assisted mineralization and flow-injection graphite furnace atomic absorption spectrometry“. *Analytica Chimica Acta* 308, 1–3 (1995), pp. 349–356 (cit. on p. 20).

[19] M. Burguera, J. L. Burguera, and O. M. Alarcón. „Flow injection and microwave-oven sample decomposition for determination of copper, zinc and iron in whole blood by atomic absorption spectrometry“. *Analytica Chimica Acta* 179 (1986), pp. 351–357 (cit. on pp. 20, 34).

[20] M. Bettinelli et al. „Determination of total urinary mercury by on-line sample microwave digestion followed by flow injection cold vapour inductively coupled plasma mass spectrometry or atomic absorption spectrometry“. *Rapid Communications in Mass Spectrometry* 16, 15 (2002), pp. 1432–1439 (cit. on p. 20).

[21] S. Hinkamp and G. Schwedt. „Determination of total phosphorus in waters with amperometric detection by coupling of flow-injection analysis with continuous microwave oven digestion“. *Analytica Chimica Acta* 236 (1990), pp. 345–350 (cit. on p. 20).

[22] Andreas Meyer and Georg Schwedt. „Kopplung von Mikrowellenaufschluß und Hydrid-AAS“. *LaborPraxis* 4 (1993), pp. 44–48 (cit. on p. 20).

[23] M. L. Balconi et al. „Chemical oxygen demand determination in well and river waters by flow-injection analysis using a microwave oven during the oxidation step“. *Analytica Chimica Acta* 261, 1–2 (1992), pp. 295–299 (cit. on p. 20).

[24] M. De la Guardia et al. „On-line microwave-assisted digestion of solid samples for their flame atomic spectrometric analysis“. *Talanta* 40, 11 (1993), pp. 1609–1617 (cit. on p. 20).

[25] Henryk Matusiewicz and Ralph E. Sturgeon. „Comparison of the efficiencies of on-line and high-pressure closed vessel approaches to microwave heated sample decomposition“. *Fresenius' Journal of Analytical Chemistry* 349, 6 (1994), pp. 428–433 (cit. on pp. 20, 37).

[26] T Dülcks. „Das Mikrowellen-Aufschlußsystem SpectroPrep im Anwendungstest“. *LaborPraxis* September 1996 (1996), pp. 68–69 (cit. on p. 21).

[27] Stephan Haiber and H. Berndt. „A novel high-temperature (360 °C)/high-pressure (30 MPa) flow system for online sample digestion applied to ICP spectrometry“. *Fresenius' Journal of Analytical Chemistry* 368, 1 (2000), pp. 52–58 (cit. on pp. 21–23, 31).

[28] P. Jacob and H. Berndt. „Online element determination in biological and environmental samples by flame AAS coupled with a high-temperature/high-pressure flow digestion system“. *Journal of Analytical Atomic Spectrometry* 17, 12 (2002), pp. 1615–1620 (cit. on pp. 21, 34).

[29] Q. Z. Bian et al. „Online flow digestion of biological and environmental samples for inductively coupled plasma–optical emission spectroscopy (ICP–OES)“. *Analytica Chimica Acta* 538, 1–2 (2005), pp. 323–329 (cit. on pp. 21, 31, 34).

[30] Q. Z. Bian. „Solid Sample Analysis by ICP-Spectrometry with Femtosecond Laser Ablation and Online Flow Digestion“. PhD thesis. 2005 (cit. on pp. 21, 34).

[31] G. Knapp. *Microwave-heatable pressure reactor*. USA Patent 5,672,316. 1995 (cit. on p. 21).

[32] Markus Lafer. „Development of an automated system for trace element analysis based on a novel flow digestion technique“. PhD thesis. 2010 (cit. on p. 23).

[33] J. S. F. Pereira et al. „High-Efficiency Microwave-Assisted Digestion Combined to in Situ Ultraviolet Radiation for the Determination of Rare Earth Elements by Ultrasonic Nebulization ICPMS in Crude Oils“. *Analytical Chemistry* 85, 22 (Nov. 2013), pp. 11034–11040. DOI: 10.1021/ac402928u (cit. on p. 33).

[34] Marco A. Z. Arruda, Mercedes Gallego, and Miguel Valcarcel. „Flow-through microwave digestion system for the determination of aluminium in shellfish by electrothermal atomic absorption spectrometry“. *Journal of Analytical Atomic Spectrometry* 10, 7 (1995), pp. 501–504 (cit. on p. 34).

[35] S. Recknagel et al. „Determination of selenium in blood serum by ICP-OES including an on-line wet digestion and Se-hydride formation procedure“. *Fresenius' Journal of Analytical Chemistry* 346, 6 (1993), pp. 833–836 (cit. on p. 34).

[36] V. Carbonell et al. „On-line microwave oven digestion flame atomic absorption analysis of solid samples“. *Analytica Chimica Acta* 238 (1990), pp. 417–421 (cit. on p. 34).

[37] V. Carbonell et al. „Atomic absorption spectrometric analysis of solids with on-line microwave-assisted digestion“. *Journal of Analytical Atomic Spectrometry* 7, 7 (1992), pp. 1085–1089 (cit. on p. 34).

[38] Edenir R. Pereira-Filho and Marco A. Z. Arruda. „Mechanised flow system for on-line microwave digestion of food samples with off-line catalytic spectrophotometric determination of cobalt at ng l^{-1} levels“. *Analyst* 124, 12 (1999), pp. 1873–1877 (cit. on p. 34).

[39] Heinz Staufenberg. „Vollautomatisches Durchfluß-Mikrowellenaufschlußsystem“. *LaborPraxis* 11 (1993), pp. 58–59 (cit. on p. 34).

[40] Vassili Karanassios et al. „Rapid stopped-flow microwave digestion system“. *Journal of Analytical Atomic Spectrometry* 6, 6 (1991), pp. 457–463 (cit. on p. 34).

[41] J. G. Speight. *Handbook of petroleum product analysis*. New Jersey: John Wiley & Sons, Inc, 2002 (cit. on p. 36).

[42] J.H. Gary, G.E. Handwerk, and M.J. Kaiser. *Petroleum refining: technology and economics*. 5th. Boca Raton: CRC Press, 2007 (cit. on p. 36).

[43] Antony Stanislaus, Abdulazeem Marafi, and Mohan S. Rana. „Recent advances in the science and technology of ultra low sulfur diesel (ULSD) production“. *Catalysis Today* 153, 1–2 (2010), pp. 1–68 (cit. on p. 36).

[44] G. Corro. „Sulfur impact on diesel emission control - a review“. *Reaction Kinetics and Catalysis Letters* 75 (2002), pp. 89–106 (cit. on p. 36).

[45] A. Sydbom et al. „Health effects of diesel exaust emissions“. *The European Respiratory Journal* 17 (2001), pp. 733–746 (cit. on p. 36).

[46] J. D. McDonald et al. „Effects of low sulfur fuel and a catalyzed particle trap on the composition and toxicity of diesel emissions“. *Environmental Health Perspectives* 112, 13 (2004), pp. 1307–1312 (cit. on p. 36).

[47] Changlong Yin et al. „Study on the formation, determination, and removal of elemental sulfur in ultra-low sulfur gas oil“. *Fuel Processing Technology* 120 (2014), pp. 16–21 (cit. on p. 36).

[48] Frank Cheng-Yu Wang et al. „Speciation of sulfur-containing compounds in diesel by comprehensive two-dimensional gas chromatography“. *Journal of Chromatographic Science* 41, 10 (2003), pp. 519–523 (cit. on p. 36).

[49] *Heavy-duty engine and vehicle standards and highway diesel fuel sulfur control requirements*. Environmental Protection Agency. 2000 (cit. on pp. 36, 46).

[50] *Directive 98/70/EC of the European Parliament and of the Council of 13 October 1998 relating to the quality of petrol and diesel fuels and amending Council Directive 93/12/EEC*. Official Journal of the European Union, EU. 1998 (cit. on pp. 36, 46).

[51] Zhaochu Hu et al. „Volatile organic solvent-induced signal enhancements in inductively coupled plasma-mass spectrometry: a case study of methanol and acetone“. *Spectrochimica Acta Part B: Atomic Spectroscopy* 59, 9 (Sept. 2004), pp. 1463–1470. DOI: 10.1016/j.sab.2004.07.007 (cit. on pp. 36, 92, 99, 108).

[52] *ASTM D 4951-14, Standard Test Method for Determination of Additive Elements in Lubricating Oils by Inductively Coupled Plasma Atomic Emission Spectrometry*. Annual Book of ASTM Standards. 2014 (cit. on p. 36).

[53] A. Ulrich and A. Wichser. „Analysis of additive metals in fuel and emission aerosols of diesel vehicles with and without particle traps“. *Analytical and Bioanalytical Chemistry* 377, 1 (2003), pp. 71–81 (cit. on pp. 36, 37).

[54] A. Montaser. *Inductively coupled plasma mass spectrometry*. New York: Wiley VCH Inc., 1998, p. 964 (cit. on p. 36).

[55] José-Luis Todolí and Jean-Michel Mermet. „Acid interferences in atomic spectrometry: analyte signal effects and subsequent reduction“. *Spectrochimica Acta Part B: Atomic Spectroscopy* 54, 6 (1999), pp. 895–929 (cit. on pp. 36, 38).

[56] *ASTM D 4294-98, Standard Test Method for Sulfur in Petroleum and Petroleum Products by Energy Dispersive X-ray Fluorescence Spectrometry*. Annual Book of ASTM Standards. 1998 (cit. on p. 37).

[57] *ASTM D 129-95 (reapproved 2000), Standard Test Method for Sulfur in Petroleum Products (General Bomb Method)*. Annual Book of ASTM Standards. 1995 (cit. on p. 37).

[58] *ASTM D 1552-95, Standard Test Method for Sulfur in Petroleum Products (High-Temperature Method)*. Annual Book of ASTM Standards. 1995 (cit. on p. 37).

[59] R. I. Botto. „Sample preparation for crude oil, petroleum products and polymers“. In: *Sample preparation for trace element analysis*. Ed. by R. S. Z. Mester. Elsevier: Amsterdam, 2003. Chap. 683-718 (cit. on p. 37).

[60] S. Pessayre et al. „Deep hydrodesulfurization of diesel oils. Matrix effect in the analysis of low sulfur diesel oils by energy dispersive X-ray fluorescence spectroscopy“. *Fuel* 78, 7 (1999), pp. 857–860 (cit. on p. 37).

[61] Pierre Allain et al. „Signal Enhancement of Elements Due to the Presence of Carbon-Containing Compounds in Inductively Coupled Plasma Mass Spectrometry“. *Analytical Chemistry* 63, 14 (1991), pp. 1497–1498 (cit. on pp. 37, 92, 108).

[62] Érico M.M. Flores et al. „Sample preparation techniques based on combustion reactions in closed vessels – A brief overview and recent applications“. *Spectrochimica Acta Part B: Atomic Spectroscopy* 62, 9 (Sept. 2007), pp. 1051–1064. DOI: 10.1016/j.sab.2007.04.018 (cit. on pp. 37, 45).

[63] Y. S. Fung and K. L. Dao. „Elemental analysis of chemical wastes by oxygen bomb combustion-ion chromatography“. *Analytica Chimica Acta* 334, 1–2 (1996), pp. 51–56 (cit. on p. 37).

[64] M. G. Liu et al. „Determination of sulfur in diesel oil certified reference materials by oxygen bomb-combustion ICP-OES“. *Spectroscopy and Spectral Analysis* 23 (2003), pp. 965–967 (cit. on p. 37).

[65] Juliana S. F. Pereira et al. „Chlorine and sulfur determination in extra-heavy crude oil by inductively coupled plasma optical emission spectrometry after microwave-induced combustion“. *Spectrochimica Acta Part B: Atomic Spectroscopy* 64, 6 (2009), pp. 554–558 (cit. on pp. 37, 40).

[66] Y. S. Fung and K. L. Dao. „Oxygen bomb combustion ion chromatography for elemental analysis of heteroatoms in fuel and wastes development“. *Analytica Chimica Acta* 315 (1995), pp. 347–355 (cit. on p. 37).

[67] R. Siegfriedt, S. Wiberley, and R. Moore. „Determination of sulfur after combustion in small oxygen bomb. Rapid titrimetric method“. *Analytical Chemistry* 23 (1951), pp. 1008–1011 (cit. on p. 37).

[68] M. J. McCormick. „Determination of total sulphur in fuel oils by ion chromatography“. *Analytica Chimica Acta* 121 (1980), pp. 233–238 (cit. on p. 37).

[69] X. Li et al. „Determination of As and Se in coal and coal combustion products using closed vessel microwave digestion and collision/reaction cell technology (CCT) of inductively coupled plasma mass spectrometry (ICP-MS)“. *International Journal of Coal Geology* 124 (2014), pp. 1–4 (cit. on p. 37).

[70] S. Dai et al. „Determination of boron in coal using closed vessel microwave digestion and inductively coupled plasma mass spectrometry (ICP-MS)“. *Energy & Fuels* 28 (2014), pp. 4517–4522 (cit. on p. 37).

[71] P. A. Mello et al. „Nickel, vanadium and sulfur determination by inductively coupled plasma optical emission spectrometry in crude oil distillation residues after microwave-induced combustion“. *Journal of Analytical Atomic Spectrometry* 24, 7 (2009), pp. 911–916 (cit. on pp. 37, 38).

[72] Cezar A. Bizzi et al. „Evaluation of a digestion procedure based on the use of diluted nitric acid solutions and H_2O_2 for the multielement determination of whole milk powder and bovine liver by ICP-based techniques“. *Journal of Analytical Atomic Spectrometry* 29, 2 (2014), pp. 332–338 (cit. on pp. 38, 41).

[73] Guillermo Grindlay et al. „A systematic study on the influence of carbon on the behavior of hard-to-ionize elements in inductively coupled plasma – mass spectrometry“. *Spectrochimica Acta Part B: Atomic Spectroscopy* 86 (May 2013), pp. 42–49. DOI: 10.1016/j.sab.2013.05.002 (cit. on pp. 38, 45, 92, 93, 110, 116).

[74] Diogo L. Rocha et al. „Greening sample preparation in inorganic analysis“. *TrAC Trends in Analytical Chemistry* 45 (2013), pp. 79–92 (cit. on p. 38).

[75] G. E. Zaikov and S. M. Lomakin. *Polymeric flame retardants: problems and decisions*. M. Kutz (Ed.) Handbook of Environmental Degradation of Materials. William Andrew, Inc., Norwich, USA, 2005 (cit. on p. 38).

[76] J. H. Troitzsch. „Overview of flame retardants“. *Chimica Oggi-Chemistry Today* 16, 1-2 (1998), pp. 18–24 (cit. on p. 38).

[77] *ASTM D 5453-12, Standard Test Method for Determination of Total Sulfur in Light Hydrocarbons, Spark Ignition Engine Fuel, Diesel Engine Fuel, and Engine Oil by Ultraviolet Fluorescence*. Annual Book of ASTM Standards. 2012 (cit. on pp. 38, 39, 42).

[78] E. M.M. Flores et al. „Determination of halogens in coal after digestion using the microwave-induced combustion technique“. *Analytical Chemistry* 80, 6 (2008), pp. 1865–1870 (cit. on p. 41).

[79] Juliana S. F. Pereira et al. „Determination of metals and metalloids in light and heavy crude oil by ICP-MS after digestion by microwave-induced combustion“. *Microchemical Journal* 96, 1 (2010), pp. 4–11 (cit. on pp. 42, 45).

[80] S. T. Gouveia et al. „Determination of residual carbon by inductively-coupled plasma optical emission spectrometry with axial and radial view configurations“. *Analytica Chimica Acta* 445, 2 (2001), pp. 269–275 (cit. on p. 45).

[81] F. G. Antes et al. „Determination of toxic elements in coal by ICP-MS after digestion using microwave-induced combustion“. *Talanta* 83, 2 (2010), pp. 364–369 (cit. on p. 45).

[82] Antoaneta Krushevska et al. „Comparison of sample decomposition procedures for the determination of zinc in milk by inductively coupled plasma atomic emission spectrometry“. *Journal of Analytical Atomic Spectrometry* 7, 6 (1992), pp. 851–858 (cit. on p. 45).

[83] Antoaneta Krushevska et al. „Determination of the residual carbon content by inductively coupled plasma atomic emission spectrometry after decomposition of biological samples“. *Journal of Analytical Atomic Spectrometry* 7, 6 (1992), pp. 845–850 (cit. on p. 45).

[84] H. C. van de Hulst and J. J. M. Reesinck. „Line Breadths and Voigt Profiles“. *Astrophysical Journal* 106 (1947), pp. 121–127 (cit. on p. 58).

[85] J. Tudor Davies and J. M. Vaughan. „A New Tabulation of the Voigt Profile“. *Astrophysical Journal* 137 (1963), pp. 1302–1305 (cit. on p. 58).

[86] J.M. Mermet. „Use of magnesium as a test element for inductively coupled plasma atomic emission spectrometry diagnostics“. *Analytica Chimica Acta* 250 (Oct. 1991), pp. 85–94. DOI: 10.1016/0003-2670(91)85064-Y (cit. on pp. 71, 81, 96).

[87] Marco A. Gigosos, Manuel Á. González, and Valentín Cardeñoso. „Computer simulated Balmer-alpha, -beta and -gamma Stark line profiles for non-equilibrium plasmas diagnostics“. *Spectrochimica Acta Part B: Atomic Spectroscopy* 58 (2003), pp. 1489–1504. DOI: 10.1016/S0584-8547 (cit. on pp. 72, 81).

[88] Helmar Wiltsche, Farzaneh Moradi, and Günter Knapp. „Evaluation of the oscillator frequency of a free running RF generator as a diagnostic tool for inductively coupled plasma-optical emission spectrometry“. *Spectrochimica Acta Part B: Atomic Spectroscopy* 71-72 (May 2012), pp. 48–53. DOI: 10.1016/j.sab.2012.05.002 (cit. on pp. 73, 81, 83, 85, 94, 96, 97, 102, 111).

[89] Charly D. Allemand, Ramon M. Barnes, and Charles C. Wohlers. „Experimental study of reduced size inductively coupled plasma torches“. *Analytical Chemistry* 51, 14 (1979), pp. 2392–2394 (cit. on p. 76).

[90] R. N. Savage and G. M. Hieftje. „Development and characterization of a miniature inductively coupled plasma source for atomic emission spectrometry“. *Analytical Chemistry* 51, 3 (1979), pp. 408–413 (cit. on p. 76).

[91] Towhid Hasan, Narong Praphairaksit, and R. S. Houk. „Low flow, externally air cooled torch for inductively coupled plasma atomic emission spectrometry with axial viewing“. *Spectrochimica Acta Part B: Atomic Spectroscopy* 56, 4 (2001), pp. 409–418 (cit. on p. 76).

[92] P. A. M. Ripson, L. de Galan, and J. W. de Ruiter. „An inductively coupled plasma using 1 L min^{-1} of argon“. *Spectrochimica Acta Part B: Atomic Spectroscopy* 37, 8 (1982), pp. 733–738 (cit. on p. 76).

[93] Guy R. Kornblum, Wouter Van der Waa, and Leo De Galan. „Reduction of argon consumption by a water cooled torch in inductively coupled plasma emission spectrometry“. *Analytical Chemistry* 51, 14 (1979), pp. 2378–2381 (cit. on p. 76).

[94] Hiroshi Kawaguchi et al. „Water cooled torch for inductively coupled plasma emission spectrometry“. *Analytical Chemistry* 52, 14 (1980), pp. 2440–2442 (cit. on p. 76).

[95] Gary M. Hieftje. „Mini, micro, and high-efficiency torches for the ICP - toys or tools?“ *Spectrochimica Acta Part B: Atomic Spectroscopy* 38, 11 (1983), pp. 1465–1481 (cit. on p. 76).

[96] Narong Praphairaksit, Daniel R. Wiederin, and R. S. Houk. „An externally air-cooled low-flow torch for inductively coupled plasma mass spectrometry“. *Spectrochimica Acta Part B: Atomic Spectroscopy* 55, 8 (2000), pp. 1279–1293 (cit. on p. 76).

[97] P. J. Morrisroe and P. H. Gagne. *High frequency transistor oscillator system.* Patent 6329757. 1996 (cit. on p. 76).

[98] Andre Klostermeier et al. „New torch design for inductively coupled plasma optical emission spectrometry with minimised gas consumption“. *Journal of Analytical Atomic Spectrometry* 20, 4 (2005), pp. 308–314 (cit. on p. 76).

[99] C. Engelhard et al. „Plasma diagnostic on a low-flow plasma for inductively coupled plasma optical emission spectrometry“. *Spectrochimica Acta, Part B: Atomic Spectroscopy* 63B, 6 (2008), pp. 619–629 (cit. on p. 76).

[100] Matthias J. Jahl, Tracey Jacksier, and Ramon M. Barnes. „Sealed Inductively Coupled Plasma Atomic Emission Spectrometry: Instrumentation Development“. *Journal of Analytical Atomic Spectrometry* 7, June (1992), pp. 653–660 (cit. on p. 76).

[101] C. Breer et al. „Enclosed Inductively Coupled Plasma: Spatially Resolved Profiles of Rotational Temperatures and Analyte Atom Distribution“. *Applied Spectroscopy* 55, 11 (2001), pp. 1462–1468 (cit. on p. 77).

[102] Matthias Wolfgang. „Entwicklung und Charakterisierung eines geschlossenen, axialen optischen Interface für die ICP-OES-Spektrometrie“. MA thesis. Technische Universität Graz, 2012 (cit. on p. 83).

[103] C. Engelhard et al. „Application of infrared thermography for online monitoring of wall temperatures in inductively coupled plasma torches with conventional and low-flow gas consumption“. *Spectrochimica Acta Part B: Atomic Spectroscopy* 62B (2007), pp. 1161–1168 (cit. on p. 84).

[104] Xianzhong Jin et al. „Inductively coupled plasma mass spectrometry with ambient helium surrounding ion source“. *Spectrochimica Acta Part B: Atomic Spectroscopy* 65, 12 (Dec. 2010), pp. 1052–1055. DOI: 10.1016/j.sab.2010.11.007 (cit. on p. 87).

[105] S. Chan and A. Montaser. „A He ICP for atomic emission spectrometry“. *Spectrochimica Acta Part B: Atomic Spectroscopy* 40B, 10-12 (1985), pp. 1467–1472 (cit. on p. 88).

[106] H. B. Fannin, C. J. Seliskar, and D. C. Miller. „Studies of energy transfer and ionisation processes in a He ICP“. *Applied Spectroscopy* 41, 4 (1987), pp. 621–624 (cit. on p. 88).

[107] L. A. Iacone et al. „Formation and fundamental characteristics of novel free-running helium inductively coupled plasmas“. *Journal of Analytical Atomic Spectrometry* 15 (2000), pp. 491–498 (cit. on p. 88).

[108] K. Jorabchi and A. Montaser. „New coil geometries for the study of secondary discharge in atmospheric-pressure helium inductively coupled plasma mass spectrometry“. *Spectrochimica Acta Part B: Atomic Spectroscopy* 59B (2004), pp. 1471–1479 (cit. on p. 88).

[109] B. Gammelgaard and O. Jøns. „Determination of selenium in urine by inductively coupled plasma mass spectrometry: interferences and optimization“. *Journal of Analytical Atomic Spectrometry* 14, 5 (1999), pp. 867–874 (cit. on pp. 92, 99, 108).

[110] G. Grindlay et al. „Carbon-related matrix effects in inductively coupled plasma atomic emission spectrometry“. *Spectrochimica Acta Part B: Atomic Spectroscopy* 63, 2 (Feb. 2008), pp. 234–243. DOI: 10.1016/j.sab.2007.11.024 (cit. on pp. 92, 93, 108).

[111] M. Kovačevič and W. Goessler. „Direct introduction of volatile carbon compounds into the spray chamber of an inductively coupled plasma mass spectrometer: Sensitivity enhancement for selenium“. *Spectrochimica Acta Part B: Atomic Spectroscopy* 60B (2005), pp. 1357–1361 (cit. on p. 92).

[112] M. Kovačevič et al. „Matrix effects during phosphorus determination with quadrupole inductively coupled plasma mass spectrometry“. *Analytical and Bioanalytical Chemistry* 383, 1 (2005), pp. 145–151 (cit. on pp. 92, 108).

[113] Erik H. Larsen and Stefan Stürup. „Carbon-enhanced inductively coupled plasma mass spectrometric detection of arsenic and selenium and its application to arsenic speciation“. *Journal of Analytical Atomic Spectrometry* 9, October (1994), pp. 1099–1105 (cit. on pp. 92, 104, 108).

[114] S. Liu and D. Beauchemin. „Effect of methanol and sodium dodecylsulfate on radial profiles of ion abundance in inductively coupled plasma mass spectrometry“. *Spectrochimica Acta Part B: Atomic Spectroscopy* 61B (2006), pp. 319–325 (cit. on p. 92).

[115] I. Llorente, M. Gómez, and C. Cámara. „Improvement of selenium determination in water by inductively coupled plasma mass spectrometry through use of organic compounds as matrix modifiers“. *Spectrochimica Acta Part B: Atomic Spectroscopy* 52, 12 (1997), pp. 1825–1838 (cit. on pp. 92, 93, 99, 108).

[116] Jiří Machát, Vítězslav Otruba, and Viktor Kanický. „Spectral and non-spectral interferences in the determination of selenium by inductively coupled plasma atomic emission spectrometry“. *Journal of Analytical Atomic Spectrometry* 17, 9 (Sept. 2002), pp. 1096–1102. DOI: 10.1039/b202167f (cit. on pp. 92, 93, 100, 108).

[117] J. Machát, V. Kanický, and V. Otruba. „Determination of selenium in blood serum by inductively coupled plasma atomic emission spectrometry with pneumatic nebulization“. *Analytical and Bioanalytical Chemistry* 372, 4 (2002), pp. 576–581 (cit. on pp. 92, 108).

[118] Maurizio Pettine et al. „Dissolved inorganic carbon effect in the determination of arsenic and chromium in mineral waters by inductively coupled plasma-mass spectrometry“. *Analytica Chimica Acta* 599, 2 (Sept. 2007), pp. 191–198. DOI: 10.1016/j.aca.2007.08.016 (cit. on p. 92).

[119] I. Rodushkin et al. „Improved multi-elemental analyses by inductively coupled plasma-sector field mass spectrometry through methane addition to the plasma“. *Journal of Analytical Atomic Spectrometry* 20 (2005), pp. 1250–1255 (cit. on pp. 92, 108).

[120] E. Warburton and H. Goenaga-Infante. „Methane mixed plasma—improved sensitivity of inductively coupled plasma mass spectrometry detection for selenium speciation analysis of wheat-based food“. *Journal of Analytical Atomic Spectrometry* 22 (2007), pp. 370–376 (cit. on pp. 92, 108).

[121] P. Kralj and M. Veber. „Investigation into nonspectroscopic effects of organic compounds in ICP-MS“. *Acta Chim. Slovenia* 50 (2003), pp. 633–644 (cit. on pp. 92, 99, 108, 113).

[122] Takashi Nakazawa et al. „Comparison of signal enhancement by co-existing carbon and by co-existing bromine in inductively coupled plasma mass spectrometry“. *Journal of Analytical Atomic Spectrometry* 29, 7 (2014), pp. 1299–1305 (cit. on p. 92).

[123] Assad S. Al-Ammar, Rajesh K. Gupta, and Ramon M. Barnes. „Correction for non-spectroscopic matrix effects in inductively coupled plasma-mass spectrometry by common analyte internal standardization“. *Spectrochimica Acta Part B: Atomic Spectroscopy* 54, 13 (1999), pp. 1849–1860 (cit. on p. 92).

[124] Fadi R. Abou-Shakra et al. „Enzymatic Digestion for the Determination of Trace Elements in Blood Serum by Inductively Coupled Plasma Mass Spectrometry“. *Journal of Analytical Atomic Spectrometry* 12, April (1997), pp. 429–433 (cit. on p. 93).

[125] Hongsen Niu and R.S. Houk. „Fundamental aspects of ion extraction in inductively coupled plasma mass spectrometry“. *Spectrochimica Acta Part B: Atomic Spectroscopy* 51, 8 (July 1996), pp. 779–815. DOI: 10.1016/0584-8547(96)01506-6 (cit. on p. 93).

[126] J. Goossens et al. „Elimination of interferences in the determination of arsenic and selenium in biological samples by inductively coupled plasma mass spectrometry“. *Analytica Chimica Acta* 280, 1 (1993), pp. 137–143 (cit. on p. 93).

[127] E. F. Huth and L. Kühn. *Schaltungsweise zur Schwingungserzeugung mit Vakuumröhren*. Ger. Pat., 310152. 1917 (cit. on p. 95).

[128] P Wetzl and O. Zehnder. *Industrieröhren in Hochfrequenzgeneratoren*. Baden, Switzerland: BBC AG, 1980 (cit. on p. 95).

[129] F. J. Maessen, P. J. H. Seeverens, and G. Kreuning. „Analytical aspects of organic solvent load reduction in normal power ICP by aerosol thermostatting at low temperatures“. *Spectrochimica Acta Part B: Atomic Spectroscopy* 39B, 9-11 (1984), pp. 1171–1180 (cit. on p. 95).

[130] Helmar Wiltsche et al. „Online combustion followed by carbon dioxide removal: evaluation of a new approach for the analysis of volatile organic substances by inductively coupled plasma optical emission spectrometry“. *Journal of Analytical Atomic Spectrometry* 29, 10 (2014), pp. 1767–1777. DOI: 10.1039/c4ja00174e (cit. on p. 95).

[131] M. W. Blades. „Excitation mechanisms and discharge characteristics - Recent developments“. In: *Inductively Coupled Plasma Emission Spectroscopy*. Ed. by P. W. J. M. Boumans. Vol. 90. Chemical Analysis. New York: Wiley Interscience, 1987. Chap. 11, pp. 387–420 (cit. on p. 96).

[132] I. B. Brenner and A. T. Zander. „Axially and radially viewed inductively coupled plasmas - a critical review“. *Spectrochimica Acta Part B: Atomic Spectroscopy* 55B (2000), pp. 1195–1240 (cit. on p. 99).

[133] J. C. Ivaldi and J. F. Tyson. „Performance evaluation of an axially viewed horizontal inductively coupled plasma for optical emission spectrometry“. *Spectrochimica Acta Part B: Atomic Spectroscopy* 50B (1995), pp. 1207–1226 (cit. on p. 99).

[134] D. G. Weir and M. W. Blades. „Characteristics of a ICP operating with organic aerosols - Part 1“. *Journal of Analytical Atomic Spectrometry* 9 (1994), pp. 1311–1322 (cit. on p. 104).

[135] George C-Y Chan and Gary M Hieftje. „Spatial emission profiles for flagging matrix interferences in axial-viewing inductively coupled plasma-atomic emission spectrometry: 2. Statistical protocol.“ *Analytical Chemistry* 85, 1 (Jan. 2013), pp. 58–65. DOI: 10.1021/ac3022345 (cit. on p. 105).

[136] J. Mora, V. Hernandis, and A. Canals. „Influence of solvent physical properties on drop size distribution, transport and sensitivity in flame atomic absorption spectrometry with pneumatic nebulization“. *Journal of Analytical Atomic Spectrometry* 6, 7 (1991), pp. 573–579 (cit. on p. 105).

[137] *Reaxys Database (Beilstein, Gmelin)*. Reed Elsevier Properties SA (cit. on p. 108).

[138] C. S. Enos, A. G. Brenton, and A. R. Lee. „A unified view of the spin conservation rule for disparate collisional processes“. *International Journal of Mass Spectrometry* 122 (1992), pp. 361–376 (cit. on p. 110).

[139] A. E. Kramida et al. *NIST Atomic Spectra Database (ver. 5.2 Online)*. Gaithersburg: National Institute of Standards and Technology, 2014 (cit. on p. 111).

[140] J. L. Todolí et al. „Elemental matrix effects in ICP-AES“. *Journal of Analytical Atomic Spectrometry* 17, 2 (2002), pp. 142–169 (cit. on p. 111).

[141] Jérôme Dennaud et al. „Study of ionic-to-atomic line intensity ratios for two axial viewing-based inductively coupled plasma atomic emission spectrometers“. *Spectrochimica Acta Part B: Atomic Spectroscopy* 56, 1 (2001), pp. 101–112 (cit. on p. 111).

[142] I. B. Brenner et al. „Ca and Na interference effects in an axially viewed ICP using low and high aerosol loadings“. *Journal of Analytical Atomic Spectrometry* 13, 11 (1998), pp. 1257–1264 (cit. on p. 111).

[143] K. Kitagawa and G. Horlick. „Deviation of the Level Populations of Iron Atoms and Ions From the Boltzmann Distribution in an Inductively Coupled Plasma: Part 2. Effect of an Easily Ionizable Element“. *Journal of Analytical Atomic Spectrometry* 7 (1992), pp. 1221–1229 (cit. on p. 112).

[144] S. Greenfield and H. McD McGeachin. „Calorimetric and dimensional studies on inductively coupled plasmas“. *Analytica Chimica Acta* 100, C (1978), pp. 101–119 (cit. on p. 113).

Acronyms

AAS atomic absorption spectrometry. 51
ADC analog-digital converter. 74, 94, 95
ANOVA analysis of variance. 45
ASTM American Society for Testing and Materials. 35, 38, 39, 42, 46

BCR Bureau Communautaire de Référence. 19, 26, 32, 33

CAPES Coordenação de Aperfeiçoamento de Pessoal de Nível Superior. 47
CCD charge-coupled device. 95
CNPq Conselho Nacional de Desenvolvimento Científico e Tecnológico. 47
CNRC Conseil National de Recherches Canada. 26
CRM certified reference material. 5, 19, 25, 26, 30, 32, 33
CTE complete thermodynamic equilibrium. 68–71

EMI electromagnetic interference. 84
EP excitation potential. 93
EPA Environmental Protection Agency. 36

FAPERGS Fundação de Amparo à Pesquisa do Estado do Rio Grande do Sul. 47
FWHA full width at half area. 54, 72
FWHM full width at half maximum. 54, 58, 72

HPLC high pressure/performance liquid chromatography. 15, 22, 32
HV high voltage. 94, 95, 102, 113, 114, 154

IC ion chromatography. 37
ICP inductively-coupled plasma. 11, 13, 25, 51, 61, 63, 71, 72, 76–78, 80, 81, 83, 85–88, 91–98, 100, 104–110, 113–116
ICP-MS inductively-coupled plasma mass spectrometer. 87, 94, 98, 99, 104

ICP-MS inductively-coupled plasma mass spectrometry. 5, 9, 45, 76, 87, 92–94, 99, 108, 115

ICP-OES inductively-coupled plasma optical emission spectrometer. 25, 62, 67, 77, 80–82, 85, 86, 94, 98, 100

ICP-OES inductively-coupled plasma optical emission spectrometry. 1, 9, 19, 25, 37–41, 45–47, 51, 62–65, 67, 72, 75, 76, 87, 91–95, 99, 100, 108, 115, 117, 121, 123

IP ionization potential. 92–94, 108, 111

IR infrared. 12

LOD limit of detection. 5, 16, 37, 46, 47, 75, 76, 81, 85, 88

LOQ limit of quantification. 5, 25, 32, 46, 75, 81, 85

LTE local thermodynamic equilibrium. 70, 71, 111, 112

MIC microwave-induced combustion. 1, 9, 12, 16, 17, 35, 37–47

NIST National Institute of Standards and Technology. 19, 26, 30–33, 38, 40, 42, 46

PC polycarbonate. 17, 95

PE polyethylene. 17, 42, 43

PEEK polyether ether ketone. 22–24

PFA perfluoroalkoxy alkane. 13–15, 19, 22–25, 29, 33

PSU power supply unit. 94, 95, 154

PTFE polytetrafluorethylene. 13–15, 21, 23, 29, 85, 97

PWM pulse width modulation. 23

RCC residual carbon content. 12, 13, 15, 19, 21, 25, 27–30, 32–34, 37, 38, 41, 45, 47

RF radiofrequency. 25, 39, 61, 64, 73–77, 80, 82–85, 87–89, 91, 92, 94, 95, 97, 99, 102–106, 110–116, 121

RMS root mean square. 102

RSD relative standard deviation. 25, 33, 46, 101, 150

SD standard deviation. 102

SRM standard reference material. 19, 26, 30–33, 38, 40, 42, 46

UV ultraviolet. 33

XRF X-ray fluorescence. 36

APPENDIX A

Octave Script for Electron Density

This chapter lists the source code of the Octave scripts which were written to evaluate the width of the H_γ emission line. It was also tried to correct some overlapping peaks by subtracting a fitted VOIGT profile.

A.1. H_gamma.m

```
1  function [FWHA,N_e] = H_gamma(filename,undesired_peaks)
2
3  more off;
4
5  peak_figure = figure;
6
7  % set parameters
8
9  lambda = 434.05; % approximate wavelength of hydrogen_gamma line
10
11 % load data file
12
13 % for *.spc file
14 % M = dlmread(filename,'\t',[19540,0,27830,1]);
15
16 % for detector readout
17 %M = dlmread(filename,'\t',[2,1,2089,2]);
18
19 % with Helmar's data converter
```

```
20 M = dlmread(filename,'\t',[1,0,45958,1]);
21
22 % sort by ascending wavelength
23
24 [n,ix] = sort(M(:,1));
25 N = zeros(size(M));
26 N = M(ix,:);
27
28 L = N(:,1); % wavelength in nm
29 I = N(:,2); % intensity
30
31 % cut interesting wavelength region
32
33 lambda_start = 432.50; % start wavelength in nm
34 lambda_end = 436.00; % end wavelength in nm
35
36 [temp,x1] = min(abs(L-lambda_start));
37 [temp,x2] = min(abs(L-lambda_end));
38 L = L(x1:x2);
39 I = I(x1:x2);
40
41 % (very) basic underground correction
42
43 [temp,x_min] = min(I);
44 I = I.-I(x_min);
45
46 % find peak maximum
47
48 peak_interval = 0.25; % interval where peak maximum is searched (in nm)
49
50 [temp,x1] = min(abs(L-(lambda-peak_interval)));
51 [temp,x2] = min(abs(L-(lambda+peak_interval)));
52 [temp,x_lambda] = max(I(x1:x2));
53 lambda = L(x1+x_lambda); % set new "exact" peak position
54
55 % final cut
56
57 peak_range = 1.00; % total peak width in nm
58
59 [temp,x1] = min(abs(L-(lambda-peak_range)));
60 [temp,x2] = min(abs(L-(lambda+peak_range)));
61 L1 = L(x1:x2);
62 I1 = I(x1:x2);
63
64 fig = figure;
```

```
65  figure(fig);
66  subplot(3,1,1);
67  plot(L1,I1);
68
69  % apply correction for undesired peaks
70
71  % undesired_peaks = [ 433.3706, 433.5486, 434.5298 ];
72
73  I_m = zeros(size(I1));
74
75  for i = 1:columns(undesired_peaks)
76
77    printf("Correcting␣for␣disturbing␣peak␣at␣%f...\n",undesired_peaks(i));
78
79    [temp,x1] = min(abs(L1-(undesired_peaks(i)-0.075)));
80    [temp,x2] = min(abs(L1-(undesired_peaks(i)+0.075)));
81    [temp,x_i] = max(I1(x1:x2));
82
83    x_1 = L1(x1+x_i-1);
84    L_1 = L1;
85    I_1 = I1;
86
87    % only fit to upper part of peak
88
89    [temp,x1_eval] = min(abs(L1-(x_1-0.04)));
90    [temp,x2_eval] = min(abs(L1-(x_1+0.04)));
91    L_1_eval = L1(x1_eval:x2_eval);
92    I_1_eval = I1(x1_eval:x2_eval);
93
94    figure(peak_figure);
95    hold off;
96    plot(L_1_eval,I_1_eval,'+');
97
98    sig = ones(size(L_1))*0.001;
99    sig_eval = ones(size(L_1_eval))*0.001;
100
101   stepsize = [.001 1e5 .001 .001 .001 .001];
102
103   SplitVoigt2 = @ (p,x) SplitVoigt(x,p);
104
105   PlotCmd = @ (f) 0;
106   a_guess = [ x_1 ; max(I_1) ; 0.005 ; 0.005 ; 0.005 ; 0.005 ];
107   [a,y_fit,cvg,outp] = nonlin_curvefit(SplitVoigt2,a_guess,L_1_eval,I_1_eval
        ,
108     struct(
```

```
109         "debug",true,
110         "Display","iter",
111         "plot_cmd",PlotCmd,
112         "lbound",[L_1_eval(1);0.001;0.001;0.001;0.001;0.001],
113         "ubound",[L_1_eval(end);+Inf;1;1;1;1],
114         "TolFun",0.00001,
115         "fract_prec",0.0000001*ones(6,1),
116         "MaxIter",200,
117         "fixed",[true;false;false;false;false;false]
118       )
119     )
120
121     fit_parameters(i,:) = a;
122     y_fit = feval('SplitVoigt',L_1,a);
123
124     figure(peak_figure);
125     hold on;
126     plot(L_1_eval,y_fit(x1_eval:x2_eval),'r');
127
128     I_m += y_fit;
129
130   endfor
131
132   fit_parameters
133
134   figure(fig);
135   subplot(3,1,1);
136   hold on;
137   plot(L1,I_m,'r');
138
139   % subtract peak model from data
140
141   I1 = I1.-I_m;
142
143   % integrate peak
144
145   I1_Int = cumtrapz(L1,I1);
146   I1_IntSum = trapz(L1,I1);
147
148   [temp,x_quartArea] = min(abs(I1_Int-I1_IntSum*0.25));
149   [temp,x_threeQuartArea] = min(abs(I1_Int-I1_IntSum*0.75));
150
151   figure(fig);
152   subplot(3,1,2);
153   plot(L1,I1);
```

```
154 hold on;
155 plot([L1(x_quartArea),L1(x_quartArea)],[min(I1),max(I1)]);
156 hold on;
157 plot([L1(x_threeQuartArea),L1(x_threeQuartArea)],[min(I1),max(I1)]);
158 subplot(3,1,3);
159 plot(L1,I1_Int);
160 hold on;
161 plot([L1(x_quartArea),L1(x_quartArea)],[min(I1_Int),max(I1_Int)]);
162 hold on;
163 plot([L1(x_threeQuartArea),L1(x_threeQuartArea)],[min(I1_Int),max(I1_Int)]);
164
165 % calculate FWHA
166
167 FWHA = L1(x_threeQuartArea)-L1(x_quartArea)
168
169 % calculate N_e
170
171 % Gigosos2003
172 N_e = nthroot(FWHA/2.433,0.68575)*10^23
173
174 more on;
```

A.2. SplitVoigt.m

```
1 function f = SplitVoigt(x,a)
2 for n = 1:rows(x)
3   if(x(n)<a(1))
4     f(n,1) = a(2)*real(Faddeeva((x(n)-a(1)+i*a(4))/(a(3)*sqrt(2))))/real(
    Faddeeva(i*a(4)/(a(3)*sqrt(2))));
5   else
6     f(n,1) = a(2)*real(Faddeeva((x(n)-a(1)+i*a(6))/(a(5)*sqrt(2))))/real(
    Faddeeva(i*a(6)/(a(5)*sqrt(2))));
7   endif
8 endfor
```

A.3. Faddeeva.m

```
1 function f = Faddeeva(zmat)
2
3 # function f = Faddeeva(z)
```

```
4  # Calculates Faddeeva function.
5  # Copyright (C) 2004 Victor Munoz
6  #
7  # Based on code in Matpack (version 1.7.3).
8  # Copyright (C) 1991-2002 by Berndt M. Gammel
9
10 # Version 1.0
11
12 DBL_MAX = 1.797693134862316e+308;
13 DBL_EPSILON= 2.220446049250313e-16;
14 M_2_SQRTPI= 2/sqrt(pi);
15
16 # The maximum value of rmaxreal equals the root of the largest number
17 # rmax which can still be implemented on the computer in double precision
18 # floating-point arithmetic
19 rmaxreal = sqrt(DBL_MAX);
20
21 # rmaxexp  = ln(rmax) - ln(2)
22 rmaxexp  = log(DBL_MAX) - log(2.0);
23
24 # the largest possible argument of a double precision goniometric function
25 rmaxgoni = 1.0 / DBL_EPSILON;
26 h2 = 0;
27 u2 = 0;
28 v2 = 0;
29 qlambda = 0;
30
31 f=zeros(size(zmat));
32
33 for fila=1:rows(zmat),
34  for columna=1:columns(zmat),
35
36    z=zmat(fila,columna);
37
38    xi = real(z);
39    yi = imag(z);
40    xabs = abs(xi);
41    yabs = abs(yi);
42    x = xabs / 6.3;
43    y = yabs / 4.4;
44
45    # the following statement protects qrho = (x^2 + y^2) against overflow
46    if ((xabs > rmaxreal) | (yabs > rmaxreal)),
47      f(fila,columna)=NaN;
48      message("Faddeeva, absolute value of argument so large w(z) overflows")
```

```
49      end
50
51
52      qrho = x .* x + y .* y;
53      xabsq = xabs .* xabs;
54      xquad = xabsq - yabs .* yabs;
55      yquad = xabs .* 2 .* yabs;
56
57      a = qrho < 0.085264;
58
59      if (a),
60
61        # If (qrho < 0.085264) then the Faddeeva-function is evaluated
62        # using a power-series (Abramowitz/Stegun, equation (7.1.5), p.297).
63        # n is the minimum number of terms needed to obtain the required
64        # accuracy.
65
66        qrho = (1 - y * 0.85) * sqrt(qrho);
67        n = round(qrho * 72 + 6);
68  # C++       j = (n << 1) + 1;
69  # e1 << e2 = e1*2^(e2);
70        j = n * 2 + 1;
71        xsum = 1.0 / j;
72        ysum = 0.0;
73        for i=n:-1:1,
74          j = j-2;
75          xaux = (xsum * xquad - ysum * yquad) / i;
76          ysum = (xsum * yquad + ysum * xquad) / i;
77          xsum = xaux + 1.0 / j;
78        end
79        u1 = (xsum * yabs + ysum * xabs) * -M_2_SQRTPI + 1.0;
80        v1 = (xsum * xabs - ysum * yabs) * M_2_SQRTPI;
81        daux = exp(-xquad);
82        u2 = daux * cos(yquad);
83        v2 = -daux * sin(yquad);
84
85        u = u1 * u2 - v1 * v2;
86        v = u1 * v2 + v1 * u2;
87      else
88
89        #  If (qrho > 1.0) then w(z) is evaluated using the Laplace continued
90        #  fraction.  nu is the minimum number of terms needed to obtain the
91        #  required accuracy.
92        #  if ((qrho > 0.085264) && (qrho < 1.0)) then w(z) is evaluated
93        #  by a truncated Taylor expansion, where the Laplace continued
```

```
94        #  fraction is used to calculate the derivatives of w(z).
95        #  kapn is the minimum number of terms in the Taylor expansion needed
96        #  to obtain the required accuracy.
97        #  nu is the minimum number of terms of the continued fraction needed
98        #  to calculate the derivatives with the required accuracy.
99
100       if (qrho > 1.0),
101         h = 0.0;
102         kapn = 0;
103         qrho = sqrt(qrho);
104 # C++: (int)
105         nu = fix(1442 / (qrho * 26 + 77) + 3);
106       else
107         qrho = (1 - y) * sqrt(1 - qrho);
108         h = qrho * 1.88;
109         h2 = h * 2;
110         kapn = round(qrho * 34 + 7);
111         nu   = round(qrho * 26 + 16);
112       end
113
114       b = h > 0.0;
115
116       if (b),
117         qlambda = h2.^kapn;
118       end
119
120       rx = ry = sx = sy = 0.0;
121       for n=nu:-1:0,
122         np1 = n + 1;
123         tx = yabs + h + np1 * rx;
124         ty = xabs - np1 * ry;
125         c = 0.5 / (tx * tx + ty * ty);
126         rx = c * tx;
127         ry = c * ty;
128         if (b & (n <= kapn)),
129           tx = qlambda + sx;
130           sx = rx * tx - ry * sy;
131           sy = ry * tx + rx * sy;
132           qlambda = qlambda/h2;
133         end
134       end
135
136       if (h == 0.0),
137         u = rx * M_2_SQRTPI;
138         v = ry * M_2_SQRTPI;
```

```
139       else
140         u = sx * M_2_SQRTPI;
141         v = sy * M_2_SQRTPI;
142       end
143
144       if (yabs == 0.0),
145         u = exp(-(xabs * xabs));
146       end
147     end
148
149     #  evaluation of w(z) in the other quadrants
150
151     if (yi < 0.0),
152
153       if (a),
154         u2 = u2*2;
155         v2 = v2*2;
156       else
157         xquad = -xquad;
158
159
160         # the following statement protects 2*exp(-z**2) against overflow
161         if ((yquad > rmaxgoni) | (xquad > rmaxexp)),
162           message("Faddeeva, absolute value of argument so large w(z)
    overflows");
163           f(fila,columna)=NaN;
164         end
165
166         w1 = exp(xquad) * 2;
167         u2 =  w1 * cos(yquad);
168         v2 = -w1 * sin(yquad);
169       end
170
171       u = u2 - u;
172       v = v2 - v;
173       if (xi > 0.0),
174         v = -v;
175       end
176     elseif (xi < 0.0),
177       v = -v;
178     end
179     f(fila,columna)=u+I*v;
180  end
181 end
```

APPENDIX B

"Carbon Enhancement Effect" – Supplementary Material

The contents of the electronic supplementary material of the "Carbon Enhancement Effect" article (chapter 9) is appended here. It can also be found under DOI:10.1039/c5ja00237k.

B.1. Enhancement factors

Table B.1.: Signal enhancement/suppression factors (emission line signal obtained in the given reagent divided by the signal obtained in 3 % HNO_3 v/v) of selected emission lines by various reagents. ND: not determined; LR: line rejected, spectral interference defined as blank signal > 10 % of the signal in the analyte containing solution before blank subtraction; RSD < 3 % for all emission lines

Emission line, nm	Total line energy, eV	Methanol 10 %	Phenylalanine 8 g L^{-1} C	15 sccm CO_2 added to the aerosol gas stream	15 sccm CO_2 added to the intermediate gas flow	Br_2 34 g L^{-1}	NaCl 30 g L^{-1}
Ag (II) 224.641	17.95	1.68	1.01	ND	ND	ND	ND
Ag (I) 328.068	3.78	1.03	0.99	ND	ND	ND	ND
Ag (I) 338.289	3.66	1.02	0.99	ND	ND	ND	ND
Al (II) 167.078	13.41	1.50	1.02	1.04	1.83	0.95	0.69
Al (I) 308.215	4.02	1.09	0.98	LR	LR	LR	LR
Al (I) 394.401	3.14	1.01	0.98	0.76	1.28	1.07	0.79
Al (I) 396.152	3.14	1.00	0.98	0.76	1.27	1.06	0.79
Ar (I) 404.442	14.69	1.97	0.98	1.36	2.49	0.88	0.90
Ar (I) 430.010	14.51	1.94	0.98	1.34	2.40	0.88	0.91
As (I) 189.042	6.56	1.97	1.08	1.52	2.08	1.04	0.83
As (I) 193.759	6.40	1.90	1.07	1.48	2.01	1.04	0.84
As (I) 197.262	6.29	1.92	1.08	1.47	1.98	1.03	0.84
Au (II) 174.050	18.22	LR	0.99	LR	LR	LR	LR
Au (I) 201.200	7.30	1.35	1.00	LR	1.47	1.06	0.80
Au (I) 242.795	5.11	1.18	1.00	0.92	1.25	1.03	0.81
Au (I) 267.595	4.63	1.09	1.00	0.89	1.17	1.02	0.82
B (II) 136.246	17.40	LR	1.05	ND	ND	ND	ND
B (I) 182.641	6.79	LR	1.01	ND	ND	ND	ND
B (I) 208.959	5.93	LR	1.00	ND	ND	ND	ND
B (I) 249.677	4.96	1.16	0.98	0.95	1.25	1.01	0.76
B (I) 249.773	4.96	1.16	0.97	0.94	1.26	1.01	0.76
Ba (II) 230.424	11.19	1.10	1.01	ND	ND	ND	ND
Ba (II) 233.527	11.22	1.08	1.02	ND	ND	ND	ND
Ba (II) 455.404	7.93	0.84	1.02	ND	ND	ND	ND
Be (I) 234.861	5.28	1.18	0.99	0.93	1.28	0.96	0.75
Be (II) 313.042	13.28	1.42	1.08	1.07	1.40	1.05	0.66
Be (II) 313.107	13.28	1.42	1.08	1.07	1.41	1.05	0.66
Bi (II) 190.241	15.91	LR	0.99	LR	1.43	0.87	0.68
Bi (I) 222.825	5.56	1.09	0.98	0.80	1.20	0.92	0.74
Bi (I) 223.061	5.56	1.03	0.97	0.78	1.18	0.94	0.74
Br (I) 144.990	8.55	LR	0.98	LR	1.73	ND	ND
Br (I) 148.845	8.33	1.57	0.98	LR	1.59	ND	ND
Br (I) 154.065	8.05	1.58	0.98	LR	LR	ND	ND
Ca (II) 183.801	14.55	LR	1.04	LR	LR	LR	LR
Ca (II) 315.887	13.16	1.24	1.03	0.86	1.44	1.00	0.66
Ca (II) 317.933	13.16	1.22	1.03	0.87	1.44	0.99	0.66
Ca (II) 393.366	9.26	0.90	1.04	0.69	0.99	0.97	0.65
Ca (II) 396.847	9.24	0.90	1.03	0.67	0.95	0.95	0.65
Ca (I) 422.673	2.93	0.99	0.96	0.70	1.26	1.29	LR
Cd (II) 214.438	14.77	1.57	1.04	1.07	1.85	0.91	0.67
Cd (II) 226.502	14.46	1.40	1.03	0.98	1.65	0.90	0.68
Cd (I) 228.802	5.42	1.31	1.02	0.98	1.44	0.97	0.79

Table B.1.: (continued)

Emission line, nm	Total line energy, eV	Methanol 10 %	Phenylalanine 8 g L^{-1} C	15 sccm CO_2 added to the aerosol gas stream	15 sccm CO_2 added to the intermediate gas flow	Br_2 34 g L^{-1}	NaCl 30 g L^{-1}
Cd (I) 361.051	7.38	1.08	1.04	0.81	1.15	0.96	0.74
Cl (I) 134.724	9.20	1.77	0.99	1.20	2.03	0.83	ND
Cl (I) 135.165	9.28	2.59	1.04	2.16	3.21	0.88	ND
Cl (I) 136.345	9.20	1.75	1.00	1.12	1.92	0.89	ND
Co (II) 228.616	13.72	1.21	1.02	0.85	1.40	0.89	0.65
Co (II) 230.786	13.75	1.19	1.02	0.85	1.40	0.90	0.65
Co (II) 238.892	13.48	1.15	1.01	0.82	1.34	0.89	0.63
Cr (II) 205.552	12.80	1.20	1.03	0.86	1.36	0.95	0.67
Cr (II) 283.563	12.69	1.14	1.03	0.83	1.32	0.94	0.67
Cr (II) 284.325	12.65	1.13	1.02	0.83	1.31	0.93	0.66
Cr (II) 284.984	12.62	1.15	1.04	0.81	1.27	0.94	0.66
Cu (II) 219.226	16.22	1.49	1.03	1.01	1.84	0.89	0.63
Cu (I) 219.958	7.02	1.24	1.00	0.90	1.40	0.94	0.72
Cu (II) 224.700	15.96	1.24	1.01	0.83	1.48	0.88	0.64
Cu (I) 324.754	3.82	0.93	1.02	0.74	1.02	1.01	0.75
Cu (I) 327.396	3.79	0.92	1.01	0.75	1.04	1.02	0.77
Fe (II) 238.204	13.11	1.20	1.01	0.86	1.39	0.85	0.65
Fe (II) 239.562	13.12	1.20	1.01	0.86	1.39	0.85	0.65
Fe (II) 241.331	13.16	1.18	1.01	0.85	1.38	0.85	0.65
Fe (II) 244.451	15.56	1.34	1.00	0.92	1.69	0.84	0.63
Fe (II) 259.941	12.67	1.11	1.00	0.81	1.27	0.83	0.64
Fe (II) 261.187	12.70	1.11	1.01	0.81	1.28	0.83	0.64
Fe (II) 262.567	12.67	1.19	1.01	0.84	1.39	0.85	0.64
Fe (II) 262.829	12.74	1.12	1.00	0.82	1.29	0.83	0.64
Fe (I) 373.486	4.18	0.96	1.04	0.76	1.13	0.96	0.83
Hg (I) 184.950	6.70	1.45	1.00	1.16	1.79	0.98	0.85
Hg (II) 194.227	16.82	1.41	1.01	1.05	1.77	0.91	0.77
Hg (I) 253.652	4.89	0.97	0.99	0.84	1.12	0.99	0.83
Hg (I) 435.835	7.73	1.20	0.99	LR	1.43	0.89	0.75
I (I) 142.549	8.70	1.70	1.06	LR	LR	ND	0.87
I (I) 161.760	7.66	LR	1.04	LR	LR	ND	LR
I (I) 178.276	6.95	1.69	1.05	LR	2.07	ND	0.83
I (I) 179.909	7.83	LR	1.06	LR	LR	ND	LR
I (I) 183.038	6.77	1.52	1.04	1.20	1.86	ND	0.76
K (I) 766.491	1.62	1.08	0.95	ND	ND	ND	ND
Mg (II) 279.079	16.51	1.38	0.97	0.87	1.79	0.85	0.59
Mg (II) 279.553	12.08	1.16	1.03	0.84	1.35	0.95	0.62
Mg (II) 280.270	12.07	1.14	1.00	0.84	1.35	0.95	0.61
Mg (I) 285.213	4.35	1.00	0.96	0.73	1.28	0.95	0.79
Mn (II) 257.611	12.25	1.07	0.99	0.80	1.28	0.92	0.64
Mn (II) 259.373	12.21	1.07	0.99	0.80	1.28	0.91	0.64
Mn (II) 260.569	12.19	1.08	1.00	0.79	1.26	0.92	0.64
Mn (II) 294.921	12.81	1.15	1.02	0.86	1.36	0.92	0.64
Mn (I) 403.076	3.08	0.75	0.98	0.58	0.95	1.06	0.78
Mo (II) 202.030	13.22	1.21	1.05	0.87	1.30	0.94	0.71
Mo (II) 203.844	13.17	1.21	1.04	LR	1.33	0.94	0.71
Mo (II) 204.598	13.15	1.19	1.05	0.86	1.30	0.94	0.71
Mo (II) 281.615	13.16	1.15	1.04	0.83	1.27	0.93	0.70
Na (I) 330.237	3.75	1.17	0.92	ND	ND	ND	ND
Na (I) 330.298	3.75	1.09	0.88	ND	ND	ND	ND

Table B.1.: (continued)

Emission line, nm	Total line energy, eV	Methanol 10 %	Phenylalanine 8 g L^{-1} C	15 sccm CO_2 added to the aerosol gas stream	15 sccm CO_2 added to the intermediate gas flow	Br_2 34 g L^{-1}	NaCl 30 g L^{-1}
Na (I) 588.995	2.10	0.86	0.93	ND	ND	ND	ND
Na (I) 589.592	2.10	0.86	0.92	ND	ND	ND	ND
Ni (II) 221.648	14.27	1.31	1.03	0.91	1.55	0.89	0.65
Ni (II) 227.021	14.26	1.29	1.02	0.90	1.52	0.88	0.64
Ni (II) 231.604	14.03	1.25	1.02	0.88	1.47	0.89	0.64
Ni (I) 232.003	5.34	1.11	0.99	0.83	1.27	0.96	0.75
Ni (I) 300.249	4.15	0.96	1.01	0.76	1.10	0.98	0.77
Ni (I) 341.476	3.66	0.88	1.02	0.71	1.00	1.02	0.82
P (I) 138.147	8.97	2.00	1.03	1.65	2.16	1.13	0.88
P (I) 168.599	8.76	2.14	1.05	LR	LR	LR	LR
P (I) 169.403	8.73	2.08	1.05	1.71	2.21	1.13	0.81
P (I) 177.495	6.99	1.89	1.04	1.56	2.00	1.13	0.86
P (I) 178.287	6.95	1.87	1.03	LR	2.01	1.13	0.86
P (I) 213.618	7.21	2.09	1.03	1.63	2.20	1.14	0.86
P (I) 214.914	7.18	2.11	1.03	1.65	2.20	1.14	0.86
Pb (II) 220.353	14.79	1.29	0.99	0.88	1.63	0.91	0.65
Pb (I) 283.305	4.38	0.97	0.97	0.77	1.16	1.02	0.76
Pb (I) 405.778	4.38	0.99	0.99	0.81	1.18	1.07	0.81
S (I) 142.503	8.70	1.44	0.97	LR	LR	1.17	0.93
S (I) 180.731	6.86	1.59	0.97	1.18	LR	1.18	0.94
S (I) 182.034	6.86	1.64	0.98	1.17	1.67	1.19	0.91
Sb (I) 187.115	6.63	LR	1.00	LR	LR	0.98	0.77
Sb (I) 206.833	5.99	1.24	1.00	LR	LR	LR	LR
Sb (I) 217.581	5.70	1.18	1.00	0.92	1.32	0.98	0.78
Sc (II) 256.023	11.41	ND	ND	1.09	1.07	ND	ND
Sc (I and II) 335.373	—	ND	ND	1.04	1.02	ND	ND
Sc (II) 355.855	10.05	ND	ND	1.05	1.02	ND	ND
Sc (II) 361.384	10.01	ND	ND	1.06	1.03	ND	ND
Sc (II) 364.279	9.96	ND	ND	1.07	1.05	ND	ND
Sc (I) 390.749	3.17	ND	ND	0.88	0.86	ND	ND
Sc (II) 424.683	9.80	ND	ND	1.03	0.99	ND	ND
Sc (II) 429.477	10.05	ND	ND	1.04	1.01	ND	ND
Sc (II) 432.501	10.02	ND	ND	1.06	1.03	ND	ND
Sc (II) 437.446	10.01	ND	ND	1.07	1.05	ND	ND
Se (I) 196.090	6.32	2.51	1.20	1.98	2.89	1.86	0.78
Se (I) 203.985	6.32	2.64	1.22	2.02	2.97	1.83	0.78
Se (I) 207.479	5.97	2.24	1.22	LR	2.37	1.85	0.71
Sr (II) 407.771	10.38	0.89	1.02	0.69	0.96	0.97	0.66
Sr (II) 421.552	10.28	0.84	1.02	0.66	0.93	0.98	0.65
Sr (I) 460.733	2.69	0.96	0.96	0.68	1.19	1.26	LR
Ti (II) 307.864	10.88	1.09	1.04	0.80	1.14	0.94	0.70
Ti (II) 323.452	10.71	1.05	1.05	0.77	1.10	0.93	0.70
Ti (II) 334.941	10.58	1.03	1.04	0.78	1.13	0.95	0.70
Ti (II) 336.121	10.54	1.03	1.04	0.78	1.13	0.94	0.70
Tl (II) 132.171	15.49	2.13	1.03	1.36	2.68	0.00	0.72
Tl (II) 190.864	12.60	LR	1.02	LR	LR	LR	LR
Tl (I) 276.787	4.48	1.06	0.95	0.79	1.27	1.04	0.81
V (II) 292.402	11.38	1.14	1.04	0.85	1.26	0.94	0.71
V (II) 292.464	11.35	1.13	1.03	0.84	1.25	0.95	0.71
V (II) 309.311	11.15	1.13	1.05	0.84	1.23	0.95	0.70

Table B.1.: (continued)

Emission line, nm	Total line energy, eV	Methanol 10 %	Phenylalanine 8 g L^{-1} C	15 sccm CO_2 added to the aerosol gas stream	15 sccm CO_2 added to the intermediate gas flow	Br_2 34 g L^{-1}	NaCl 30 g L^{-1}
V (II) 311.071	11.08	1.10	1.05	0.82	1.20	0.93	0.70
Zn (II) 202.548	15.51	1.81	1.05	1.23	2.10	0.91	0.69
Zn (II) 206.191	15.40	1.78	1.05	1.21	2.04	0.91	0.69
Zn (I) 213.856	5.80	1.28	1.01	0.94	1.41	0.93	0.77
Zn (I) 334.502	7.78	1.25	1.00	0.97	1.40	0.91	0.72

B.2. HV PSU Data Logger Schematics

The following pages include the schematics of the HV-PSU data logger which was used in the investigations of the “carbon enhancement effect” (refer to chapter 9).

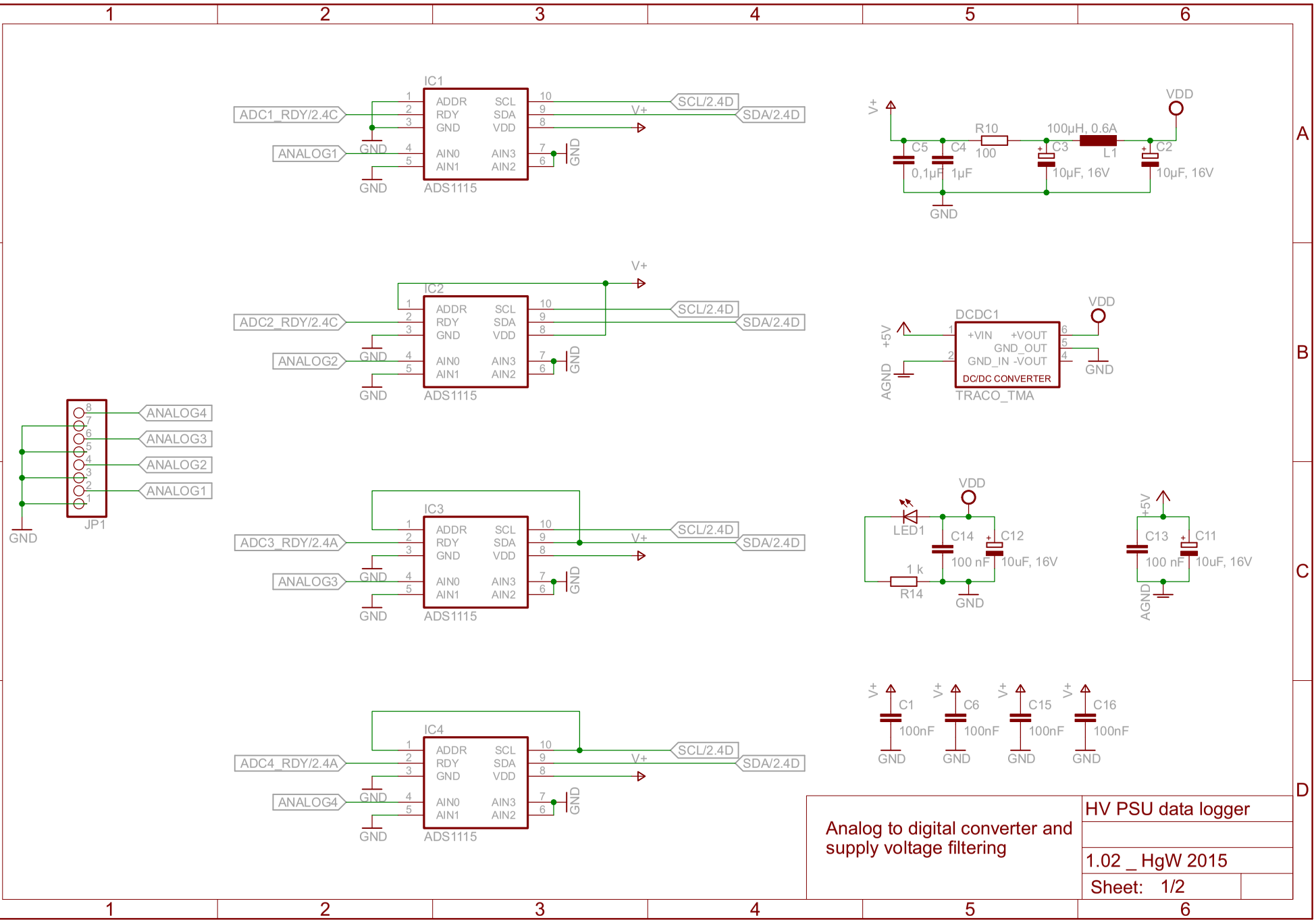
IC1
ADDR
RDY
GND
AIN0
AIN1
SCL
SDA
VDD
AIN3
AIN2
ADS1115
ADC1_RDY/2.4C
ANALOG1
SCL/2.4D
SDA/2.4D
V+
GND
IC2
ADC2_RDY/2.4C
ANALOG2
IC3
ADC3_RDY/2.4A
ANALOG3
IC4
ADC4_RDY/2.4A
ANALOG4
JP1
R10
100
100µH, 0.6A
L1
C5
0,1µF
C4
1µF
C3
10µF, 16V
C2
10µF, 16V
VDD
DCDC1
+VIN
+VOUT
GND_OUT
GND_IN -VOUT
DC/DC CONVERTER
TRACO_TMA
+5V
AGND
LED1
C14
100 nF
C12
10uF, 16V
1 k
R14
C13
C11
C1
C6
C15
C16
100nF
Analog to digital converter and supply voltage filtering
HV PSU data logger
1.02 _ HgW 2015
Sheet: 1/2

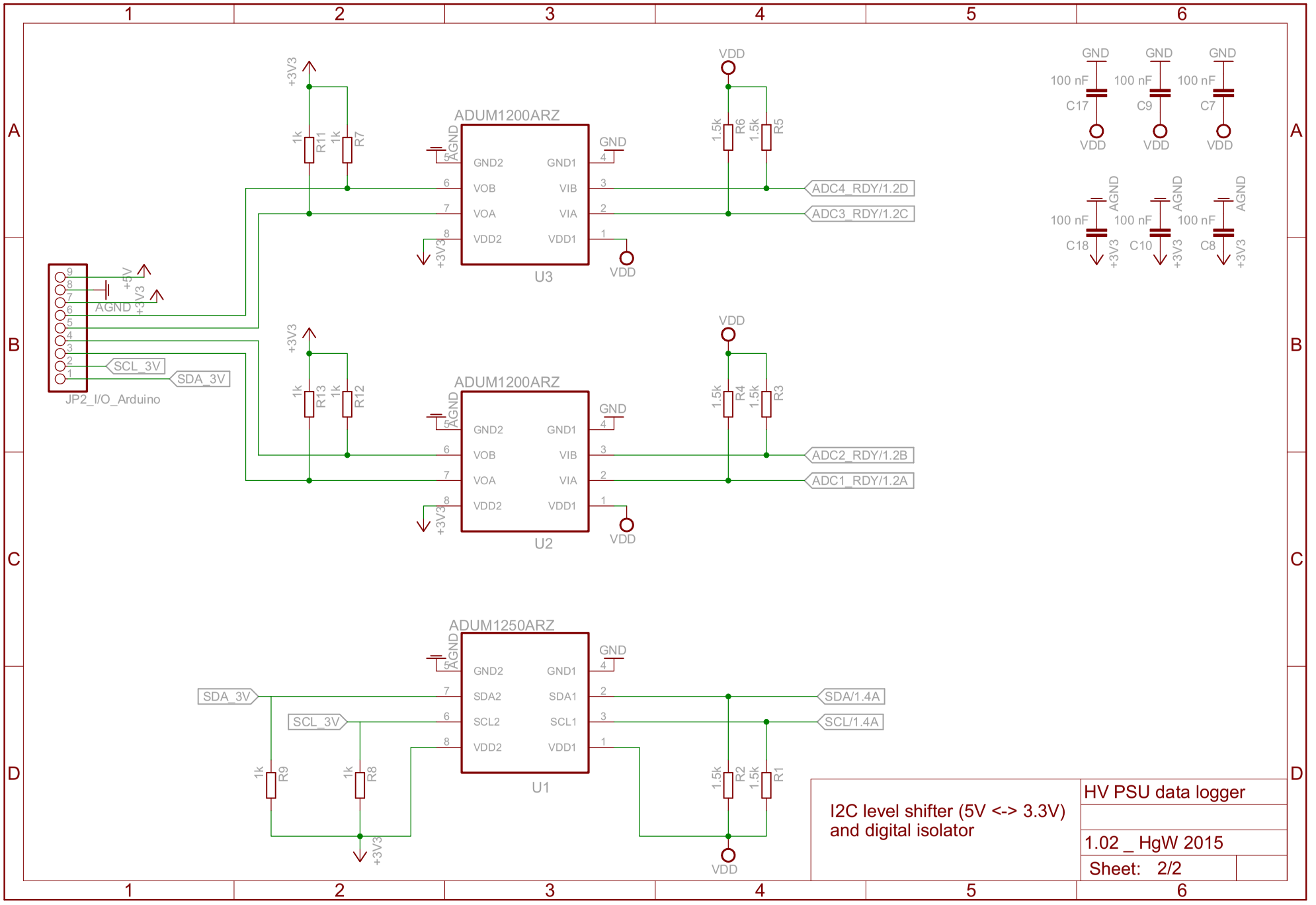
ADUM1200ARZ
U3
ADUM1200ARZ
U2
ADUM1250ARZ
U1
JP2_I/O_Arduino
SCL_3V
SDA_3V
AGND
+5V
+3V3
VDD
GND
ADC4_RDY/1.2D
ADC3_RDY/1.2C
ADC2_RDY/1.2B
ADC1_RDY/1.2A
SDA/1.4A
SCL/1.4A
R11
R7
R6
R5
R13
R12
R4
R3
R9
R8
R2
R1
C17
C9
C7
C18
C10
C8
100 nF
1k
1.5k
I2C level shifter (5V <-> 3.3V)
and digital isolator
HV PSU data logger
1.02 _ HgW 2015
Sheet: 2/2